


Doctoral Dissertation
Doctoral Program in Electrical, Electronics and Communication Engineering
(33.rd cycle)

Analysis and Detection of Outliers in GNSS Measurements by Means of Machine Learning Algorithms

Caner Savas

* * * * *

Supervisor
Prof. Fabio Dovis

Doctoral Examination Committee:
Prof. Elena Simona Lohan, Referee, Tampere University
Prof. Steffen Schön, Referee, Leibniz Universität Hannover
Prof. Enrico Magli, Politecnico di Torino
Dr. Lucilla Alfonsi, Istituto Nazionale di Geofisica e Vulcanologia
Dr. Melania Susi, Joint Research Center of the European Commission

Politecnico di Torino
May 7, 2021

I hereby declare that, the contents and organisation of this dissertation constitute my own original work and does not compromise in any way the rights of third parties, including those relating to the security of personal data.

. . . . . .

Caner Savas

Turin, May 7, 2021

Summary

Global Navigation Satellite Systems (GNSS) have a central role in many applications that require high accuracy and precision such as in air/marine transport, robotics, military operations, and precision agriculture applications. However, GNSS signals suffer from many error sources, such as interference/jamming, ionospheric/atmospheric anomalies, and multipath that affect the quality of the estimated position. To reach a high level of accuracy in the navigation, the GNSS errors must be corrected. GNSS modernization with the availability of multi-frequency signals and multi-constellations has been providing an improvement against the degradation effects of many error sources, leaving the scintillation effect that has a quasi-random nature and the multipath as the most significant and dominant error contributions in positioning. In parallel, the advancement of the technology for processors is boosting the fully software implementations of GNSS receivers running on a General-Purpose Processor (GPP), also for multi-band and multi-constellation architectures. Among the well-known advantages of such flexible implementations, the software approach opens the door to new paradigms for the implementation of the receiver functions needed for signal processing and position estimation, and receiver implementations have been constantly evolving to alleviate the performance degradation effects of error sources such as scintillation and multipath.

In this context, this thesis aims at analyzing the effects of scintillation and multipath through GNSS observables and measurements utilizing the implemented post-processing GNSS receiver and investigating and designing the scintillation and multipath detection methods based on Artificial Intelligence (AI) solutions. Assessing the performance analysis of GNSS receiver acquisition and tracking stages allows to choose the best setting of the acquisition and tracking parameters to provide the receiver operation at a comparable performance level by testing the robustness of the implemented algorithms under harsh amplitude and phase scintillation conditions. Detecting and monitoring the scintillation effects to estimate the ionospheric scintillation in its early stages and measure the scintillation parameters are important as well. With the evolving AI world, Machine Learning (ML) algorithms have gained importance to be applied for the detection of similarities and outliers among the observables and measurements. In this thesis, one of the

proposed methods based on supervised machine learning algorithms, namely, Support Vector Machines (SVM) is implemented and analyzed through different kernel functions such as linear, Gaussian Radial Basis Function (RBF), and polynomial for scintillation detection. The work addressed the investigation of an optimal kernel function and parameter settings for this specific task, trading-off performance, space and time complexity of the method. It is also known that the presence of multipath errors falsely inflates the measurements of the ionospheric scintillation activity. It is then of paramount importance to detect the satellite signals that suffer from the multipath effect to reach an acceptable positioning accuracy and to increase the scintillation detection performance. The developed and implemented multipath detection algorithms work at the measurement level and are based on unsupervised ML algorithms, namely, K-means and Self-Organizing Map (SOM). It is demonstrated in the thesis that this ML approach overcomes the limitation of the availability of training data sets a-priori obtained as representative of multipath and no-multipath conditions. The measurement sets computed for each tracked satellite signal, namely, carrier phase, pseudorange, and carrier-to-noise ratio are in fact used to create clusters of consistent measurements. The performance of the detection algorithms is assessed under different conditions with collected different datasets.

To sum up, within the framework of this thesis study, starting from the design and implementation of multi-frequency multi-constellation software GNSS receiver, a detailed analysis of different signal acquisition and tracking methods in order to test their robustness to the presence of scintillation and to select optimal setting parameters has been realized. Having analyzed the effects of multipath and scintillation on the receiver observables and measurements, investigation and use of AI solutions through different ML algorithms to develop new countermeasures have been studied.

Acknowledgements

First of all, I would like to express my sincere gratitude to my supervisor Professor Fabio Dovis for his complete guidance, continuous support, advice, criticism, and encouragement throughout my doctoral studies.

I would like to acknowledge TREASURE project, funded by European Union's Horizon 2020 Research and Innovation Programme within Marie Skłodowska Curie Actions (MSCA) Innovative Training Network (ITN), for funding my studies and providing invaluable training opportunities. I would like to thank the Space Geodetic Research Group led by Prof. João Francisco Galera Monico at UNESP and the Space and Navigation Research Division of LINKS foundation headed by Dr. Marco Pini for their support during my secondments within the TREASURE project.

I appreciate the support from the members of the Navigation Signal Analysis and Simulation (NavSAS) group who contributed to the research activities in various ways. I would like to mention Dr. Gianluca Falco and former NavSAS member Dr. Nicola Linty, whose contributions since the beginning of my research are very important. Also, I would like to thank my colleagues Neil, Calogero, Alex, Wenjian, Rayan, and Andrea for the good times spent together.

For the ionospheric scintillation datasets used in this study, I would like to thank the Italian National Research Programme for Antarctica (Programma Nazionale di Ricerche in Antartide, PNRA), for the data collected in the framework of the DemoGRAPE project, under contract 2013/C3.01. Moreover, I also thank Hans Visser from Fugro Innovation and Technology B.V., The Netherlands for the data collected during road tests conducted in The Hague, The Netherlands.

As for my personal life, I would like to extend my special appreciation to my Selcen for her love and support throughout this study. Last but not the least; I would like to express my deepest gratitude to my parents and my sister for their love, trust, understanding, and permanent support throughout my life.

Contents

List of Tables

List of Figures

List of Acronyms

ADC	Analog-to-Digital Converter
ADR	Accumulated Delta Range
AGC	Automatic Gain Control
AI	Artificial Intelligence
AIWB	Axial Integrated Wigner Bispectrum
AltBOC	Alternative Binary Offset Carrier
ANN	Articial Neural Network
AUC	Area Under Curve
AWGN	Additive White Gaussian Noise
BMU	Best-Matching Unit
BOC	Binary Offset Carrier
BPSK	Binary Phase Shift Keying
C/A	Coarse/Acquisition
CAF	Cross Ambiguity Function
CBOC	Composite Binary Offset Carrier
CDMA	Code Division Multiple Access
CNN	Convolutional Neural Network
CSM	Cornell Scintillation Model
C/N_0	Signal Carrier-to-Noise Density Power Ratio
DCM	Direction Cosine Matrix

DL	Deep Learning
DLL	Delay Lock Loop
DNN	Deep Neural Network
DPP	Dot-Product Power
EC	European Commission
ECEF	Earth Centered Earth Fixed
EKF	Extended Kalman Filter
ELE	Early-minus-Late Envelope
ELP	Early-minus-Late Power
ENU	East-North-Up
ESA	European Space Agency
FEC	Forward Error Correction
FDMA	Frequency Division Multiple Access
FLL	Frequency Lock Loop
FN	False Negative
FPGA	Field Programmable Gate Array
FP	False Positive
FPR	False Positive Rate
GEO	Geostationary Earth Orbit
GISM	Global Ionospheric Scintillation Model
GLONASS	GLObal NAvigation Satellite System
GNSS	Global Navigation Satellite System
GPP	General Purpose Processor
GPS	Global Positioning System
HPF	High Pass Filter

ICD	Interface Control Document
IF	Intermediate Frequency
IGSO	Inclined Geo-Synchronous Orbits
IRI	International Reference Ionosphere
ISMR	Ionospheric Scintillation Monitoring Receiver
ISOMAP	ISOmetric MAPping
KF	Kalman Filter
kNN	k-Nearest Neighbors
LE	Laplacian Eigen
LOS	Line-Of-Sight
LNA	Low Noise Amplifier
LO	Local Oscillator
LSSVM	Least Squares Support Vector Machines
MEDLL	Multipath Estimating Delay Lock Loop
MEO	Medium Earth Orbits
ML	Machine Learning
MMT	Multipath Mitigation Technology
NBC	Naïve Bayes Classifier
NBP	Narrow Band Power
MPS	Multiple Phase Screen
NARX	Nonlinear Autoregressive with External Input
NCO	Numerically Controlled Oscillator
NED	North-East-Down
NH	Neuman-Hofman
NLOS	Non-Line-Of-Sight

NN	Neural Network
OS	Open Service
PCA	Principal Component Analysis
PE	Parabolic Equation
PLL	Phase Lock Loop
PPP	Precise Point Positioning
PRN	Pseudo-Random Noise
PSD	Power Spectral Density
PSK	Phase Shift Keying
PVT	Position, Velocity and Time
QMBOC	Quadrature Multiplexed Binary Offset Carrier
QPSK	Quadrature Phase Shift Keying
RAIM	Receiver Autonomous Integrity Monitoring
RHCP	Right-Hand Circularly Polarized
RBF	Radial Basis Function
RF	Radio Frequency
RFE	Radio Front-End
RFF	RF Fingerprinting
RFI	Radio-Frequency Interference
RKHS	Reproducing Kernel Hilbert Space
RNN	Recurrent Neural Network
ROC	Receiver Operating Characteristics
ROT	Rate of TEC
RPA	Retarding Potential Analyzer
RSS	Root Sum Squared

RTK	Real Time Kinematic
SBAS	Space Based Augmentation System
SDR	Software Defined Radio
SNN	Spiking Neural Network
SNR	Signal-to-Noise Ratio
SOM	Self-Organizing Map
SV	Satellite Vehicle
SVM	Support Vector Machines
TEC	Total Electron Content
ToA	Time of Arrival
TOW	Time of Week
TN	True Negative
TNR	True Negative Rate
TP	True Positive
TPR	True Positive Rate
TWSVM	Twin Support Vector Machine
UERE	User Equivalent Range Error
USRP	Universal Software Radio Peripheral
UHF	Ultra High Frequency
UTC	Universal Time Coordinated
UTM	Universal Transverse Mercator
VC	Vision Correlator
VHF	Very High Frequency
WAM	Wernik-Alfonsi-Materassi
WBMOD	WideBand MODel

WBP Wide Band Power

WT-SVD Wavelet Transform - Singular Value Decomposition

Chapter 1

Introduction

This Chapter provides a general background of Global Navigation Satellite System (GNSS) receivers, phenomena of multipath propagation and scintillation, Software Defined Radio (SDR) approach in GNSS receivers. It continues with the objectives and contributions of this research and at the end, an outline of the thesis is presented.

1.1 Background

GNSS receivers have a central role in many applications necessitating high accuracy and precision such as in air/marine transport, robotics, autonomous vehicles, military operations, and precision agriculture. However, GNSS signals are prone to suffer from numerous error sources (e.g. interference/jamming, ionospheric/atmospheric anomalies, multipath, etc.) that must be detected and corrected at the receiver level in order to reach a good level of accuracy in the navigation. GNSS modernization with the availability of multi-frequency signals and multi-constellations, the capabilities of new civil signals, and the upsurge in research and development of GNSS receiver algorithms have been providing an improvement against the degradation effects of many error sources for positioning [1, 2]. However, the reception of the reflected or diffracted replicas of the desired signals due to propagation through the ionospheric layer and the physical surrounding environment is leaving the multipath and scintillation effects as significant and sometimes dominant error contributions in the positioning [3].

As it is observed in the trans-ionospheric communication of the radio waves while traveling from transmitter to user, the GNSS signals are affected by the ionosphere that is highly variable and dynamic in both time and space [4] and it is a fact of life for a number of communication and radar systems that have to operate through the auroral or equatorial ionosphere [5]. In the same way, scintillation caused by the electron density irregularities in the ionospheric plasma leads to

rapid fluctuations in the amplitude and phase of the GNSS signals, as pictorial representation depicted in Figure 1.1 (a). Under multipath conditions, the received signal by the GNSS antenna consists of the direct Line-Of-Sight (LOS) and the multipath signals whereas the Non-Line-Of-Sight (NLOS) signals contain only the reflected signals, as demonstrated in Figure 1.1 (b). The presence of scintillation and multipath conditions cause large degradation in the navigation performance and it is of paramount importance to detect the satellite signals suffering from the multipath and scintillation effects.

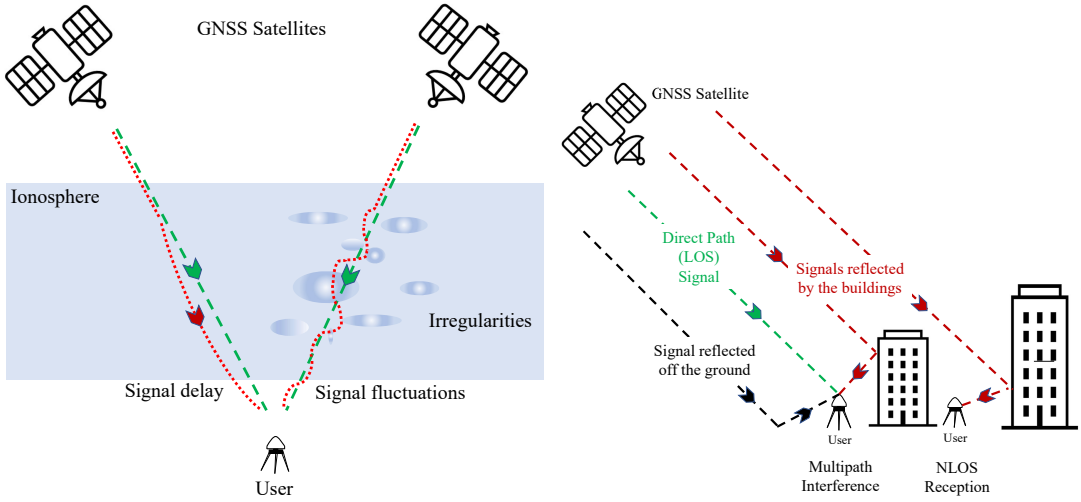

(a) Ionospheric delay and scintillation - Adapted from [6].

(b) Multipath and NLOS reception - Adapted from [7].

Figure 1.1: Pictorial representations of ionospheric delay, scintillation effect, multipath, and NLOS reception. The green dashed lines are the LOS paths from GNSS satellites to the receiver on earth; the red dashed lines account for propagation distortion due to the ionosphere and surrounding environment of the receiver.

Proper countermeasures must be undertaken at receiver level in order to correct and minimize the effects of such threats, and the countermeasures are specific for each source. Various methods have been employed in a GNSS receiver either at the signal processing and measurement level in order to cope with these effects. Given this picture, the software radio implementation that is applicable to any Radio Frequency (RF) transmission provides a tremendous level of flexibility and establishes a framework for the implementation and test of advanced algorithms [8]. It is a promising way to implement new algorithms and processing strategies.

Software GNSS receivers are being used since many years, mainly as research tools or as tools at the early stage of the design process. They can be implemented as software defined, or fully software receivers, depending on the computational burden of the processing and on the real-time/non real-time requirements. Having access

to the internal stages and related observables and measurements allows easiness and flexibility in both design and analysis of the implemented algorithms.

Moreover, with the flourishing Artificial Intelligence (AI) world, Machine Learning (ML) algorithms enable us to interpret the data correctly, to integrate the information better, to draw wider data insights, and to improve the decisions on the results. Therewithal, with the innovative trend of SDR receivers and ML algorithms, receiver implementations have been constantly evolving to alleviate the performance degradation effects of error sources such as scintillation and multipath.

1.2 Objectives and contributions of the thesis

Given the fundamental role of the software GNSS receiver and aspects of the ML algorithms, the objective of this thesis is the investigation of new approaches to the receiver design focusing on the signal processing stages. In particular, this means to address new techniques for scintillation and multipath identification and rejection, as well as the exploitation of new methods based on AI in this field.

Although scintillation phenomena are well known and characterized, it is difficult to find a definitive treatment of the theory of scintillation [9]. Moreover, the observation of scintillation has been used in many research fields such as astronomy, geophysics, atmospheric physics, telecommunications, etc. to identify the irregular structure of the propagation medium [4]. Even if the GNSS signals are themselves affected by scintillation too, ionospheric scintillation through some measurement indices can be estimated by means of received GNSS signals as it is discussed in Section 3.1.1. Specialized Ionospheric Scintillation Monitoring Receivers (ISMRs) and software receivers have started to be used for ionospheric scintillation monitoring purposes. A scintillation monitoring and data collection setup at which the data sets used throughout this thesis were collected is defined in Section 3.1.2.

Moreover, thanks to a tremendous number of observations, studies on the atmospheric structure, modeling the wave propagation through ionospheric irregularities, and scattering theories have led to the development of different ionospheric scintillation models. It is quite important to understand the global morphology of ionospheric scintillation and to be able to model it. Because it helps users to differentiate between the fluctuations that are caused by ionospheric irregularities and the ones that are originated from equipments or other error sources [4]. The countermeasures are specific for each error source. However, when the ionospheric scintillation models where are discussed in Section 3.2.1 are considered, it has been observed that there are limitations and simplicities in case of creating the characteristics of actual scintillation effects in GNSS applications. Hence, this points out the significance of collecting real GNSS data under scintillation events.

Under a scintillation event, proper countermeasures could be undertaken at signal processing level, enabling either more robust signal acquisition and tracking

or alternate resources to decrease the effect of disturbed signal propagations. The work started from a comparative study of different acquisition and tracking methods for GPS L5 and L1 C/A signals in order to test their robustness to the presence of observed real phase and amplitude scintillations in the propagation environment. Compared to observing the scintillation effects only in the positioning performance of the GNSS receiver, implemented software GNSS receiver provides advantages in both design and performance analysis of the implemented algorithms thanks to having access to the internal stages and observables.

Besides the scintillation effect, the multipath effect is another significant and dominant error contribution in the positioning as exemplified through the analysis of simulated and real data sets in Section 3.3. Moreover, the presence of multipath errors falsely indicates the existence of ionospheric scintillation by inflating the scintillation measurements of the receiver. In the literature, for detection of scintillation and multipath effects, numerous algorithms, where a general overview discussion is provided in Section 3.2.3 and Section 3.3.3, have been proposed either at signal processing or measurement processing stages of the receiver.

In the framework of this thesis, new approaches utilizing AI solutions have been investigated. Although there is an increasing interest in the application of ML-based approaches in different fields, it has to be noted that ML algorithms are not simply plug-and-play tools. The selection of the method with the design and implementation of data preparation procedure and tuning of the setting parameters have significant roles in the performance of the implemented algorithm for the solution of the problem. With this perspective in mind, detection of scintillation and multipath effects have been investigated and applied by means of implemented ML-based methods.

Main contributions of the thesis are summarized as follows:

- A detailed comparative study of the different acquisition and tracking methods for GPS L5 and L1 C/A signals in order to test their robustness to the presence of real phase and amplitude scintillations in the propagation environment and to select the optimal acquisition and tracking parameters.

- With the analysis of the effects of scintillation and multipath on receiver observables and measurements, the investigation and use of AI solutions through ML methods to develop new countermeasures.

- Development, analysis, and performance assessment of multipath detection algorithm through simulated, real static and kinematic data.

Some of the works presented in the thesis were published in the peer-reviewed journal papers [10, 11] and in different international conferences [12, 13, 14, 15]. Furthermore, side works related to the estimation of scintillation indices and application of multipath detection algorithm led to other publications [16, 17].

1.3 Outline of the thesis

Chapter 2 provides an overview of GNSS, principles of satellite navigation, signal structures, and main GNSS error sources. It continues with GNSS receiver architecture and the basics of the different stages in a receiver. Eventually, with the concept of SDR-based GNSS receiver, the challenges in the implementations are discussed.

Chapter 3 starts with a description of the scintillation effect including the estimation of the phase and amplitude scintillation indices that quantify and characterize the scintillation events. As an introduction to the experimental part of thesis work, the data collection setup utilizing the SDR receiver approach and analysis of real scintillation data are provided. Having discussed the simulation models in the literature, an overview of the effects of scintillation at the signal processing stages of a GNSS receiver and classical scintillation detection strategies are given. Likewise, in the last part of the chapter, the multipath effect on the GNSS measurements and observables is investigated through the analysis of simulated and real GNSS data. Moreover, classical multipath detection strategies and especially, the potential of the Receiver Autonomous Integrity Monitoring (RAIM) algorithm for multipath detection is examined.

Chapter 4 presents a detailed comparative study of the different acquisition and tracking methods for GPS L5 and L1 C/A signals in order to test their robustness to the presence of phase and amplitude scintillations in the propagation environment. Implementation of four L5 and three L1 C/A acquisition methods and performance comparison in terms of probabilities of detection/false alarm, peak-to-noise floor ratios and acquisition time duration are given. By employing Phase Lock Loop (PLL) and Kalman Filter (KF)-based carrier-tracking algorithms for GPS L1 C/A and L5 signals, the performances of different architectures are evaluated and compared in terms of the residual effects on the receiver observables and internal parameters.

Chapter 5 first describes the ML-based methods and discusses the role of ML in a GNSS receiver. Afterward, with an overview of the Support Vector Machines (SVM) algorithm and kernel function, implementation of the scintillation detection algorithm is detailed. The impact of the kernel function on the scintillation detection performance is evaluated by exploiting Receiver Operating Characteristics (ROC) curves, confusion matrix results, and the related performance metrics. Then, implementation details of the proposed multipath detection approach based on K-means and Self-Organizing Map (SOM) algorithms and a comprehensive performance analysis with different real static and kinematic data are provided.

Chapter 6 finally provides a summary of the researches presented within this thesis and discusses some future works.

Chapter 2

Global Navigation Satellite Systems

In this chapter, an overview of GNSS and fundamentals of satellite navigation are presented. With the signal structures, a GNSS receiver architecture and the basics of the different stages in a receiver are explained considering the concept of SDR-based GNSS receiver and the challenges in the implementations. Eventually, the main GNSS error sources are pointed out.

GNSS is a generic term for a space-based navigation system that provides users an ability to determine their Position, Velocity, and Time (PVT) in a common reference system on a continuous basis. There are four operational GNSSs, namely, the U.S. Global Positioning System (GPS), the Russian Federation's GLObal NAvigation Satellite System (GLONASS), the European Galileo system, and the Chinese BeiDou Navigation Satellite Demonstration System (BDS). The first operational prototype satellite of the GPS was launched in 1978 and the initial operational capability of the full system with 24 satellites was realized in 1993 [18]. Although GLONASS is the second fully operational system deployed in 1995, the number of satellites gradually decreased down to 7 in 2001 due to limited operational lifetime of the first satellites and fully global service was re-establised in 2011 [19]. Galileo development was initiated in late 2013 and carried out by a joint initiative of the European Commission (EC), the European Space Agency (ESA), and the European GNSS Agency (GSA). Initial operational phase was declared in December 2016, and by end of 2020, there are 24 usable, 1 unavailable and 1 not-usable satellites in the orbit [20]. The BDS-3 is the global service developed as extension of the the Regional Orbit Determination Satellite Service (RDSS) implementations established in the frame of BDS-1 and BDS-2 initiated in 2000 and 2012, respectively [21]. Since July 2020, BDS-3 has 24 active satellites in the orbit. Furthermore, the modernization programs including such as the changes in the signal structures and upgrades of the satellites have been ongoing for all the aforementioned systems.

A GNSS system consists of three components: the space segment, the control

or ground segment, and the user segment, as depicted in Figure 2.1. The space segment comprises the satellites (i.e. space vehicles (SVs)) that broadcast signals to both the users and the control segment and collectively known as a constellation. The current constellation arrangements of the systems are summarized in Table 2.1. GPS, GLONASS, and Galileo satellites are distributed among a number of Medium Earth Orbits (MEOs) [18]. However, BDS-3 consists of 3 Geostationary Earth Orbit (GEO) and 3 Inclined Geo-Synchronous Orbits (IGSO) satellites besides 24 MEO satellites.

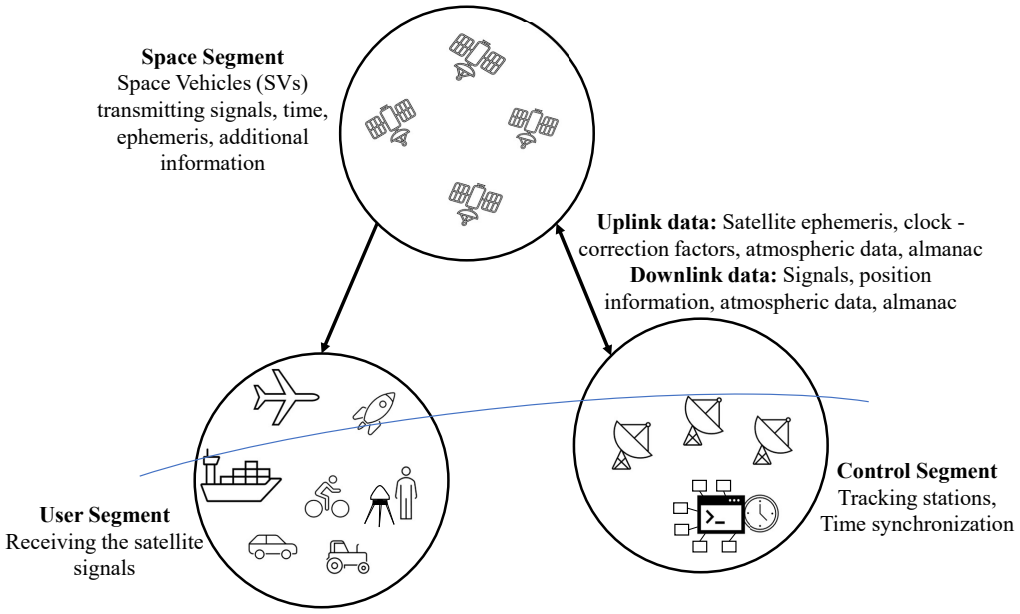

Figure 2.1: GNSS segments.

Table 2.1: GNSS Constellation Parameters [22, 23, 24, 19, 25, 21]

Parameters	GPS	GLONASS	GALILEO	BEIDOU (BDS-3)		
				GEO	MEO	IGSO
Number of operational satellites	24	24	24	3	24	3
Number of orbital planes	6	3	3	1	3	3
Number of satellites in a plane	4	8	8	3	8	1
Eccentricity	$e < 0.02$	$e < 0.001$	$e = 0.0$	$e = 0.0$	$e = 0.0$	$e = 0.0$
Inclination	55°	64.8° ± 0.3°	56°	80°E, 110.5°E, 140°E	55°	55°
Nominal orbital altitude [km]	20180	19100	29600.318	35786	21528	35786
Period of revolution	11 h 58 m	11 h 15 m 44 s ± 5 s	14 h 4 m 42 s	–	12 h 53 m	–

The control segment consists of a network of monitoring stations, control stations, and uplink statitions as depicted in Figure 2.1. In order to determine the satellite orbits and calibrate the satellite clocks, the ranging measurements are used

by the monitoring stations of which locations are precisely defined, the navigation data message for each satellite are computed and are transmitted to the space segment by the uplink stations [18]. The user segment comprises GNSS antennas and receivers that receive and process GNSS signals to determine user coordinates needed in different applications. In the following with the principle of navigation, the signal structure and the receiver architecture are introduced by recalling the main aspects. There are many books where a detailed explanation of the fundamentals of satellite navigation, signal structures, and receiver architectures are covered such as [18, 26, 27, 28, 29].

2.1 Satellite navigation principles

GNSS signals that are detailed in the next section consist of a modulation of the *carrier* on different frequencies with a unique *Pseudo-Random Noise (PRN) ranging code* continuously repeating at intervals of a few milliseconds to seconds for each satellite. On top of the ranging code, the signal may also be modulated by low rate *navigation data* that contains information about the orbits and clock offsets [30].

GNSS exploits the Time of Arrival (ToA) ranging concept in principle to determine user position [26] by measuring the propagation time of the signal from the satellite as depicted in Figure 2.2.

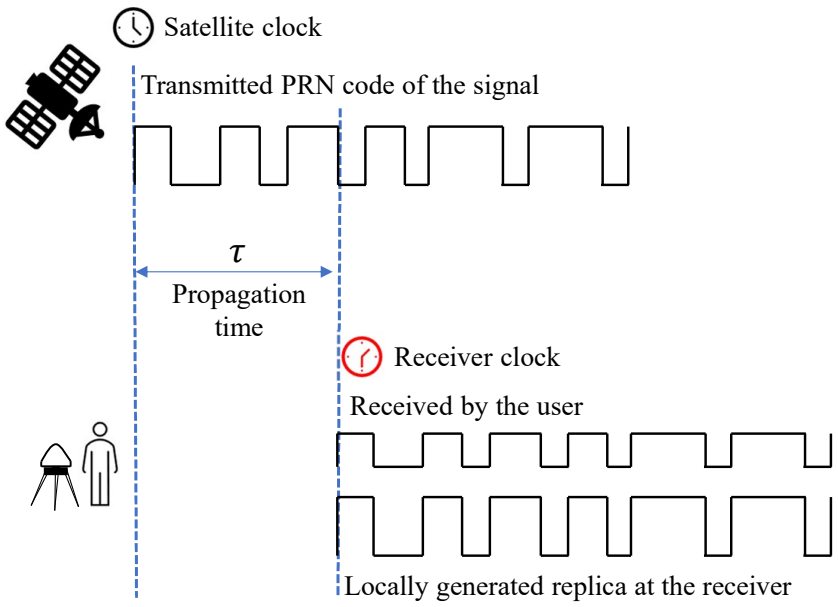

Figure 2.2: Clocks on range measurement and principle of pseudorange measurement.

If a satellite (i) transmits a ranging signal traveling at the speed of light (c) at t_0, it is received by the receiver at time $t_0 + \tau$, this time interval can be converted to a range (R_i):

$$R_i = c\,\tau \tag{2.1}$$

Although the clocks of the satellites within a constellation are synchronized to an internal scale that is known as system time (e.g. GPS time), the user's clock as picturized in Figure 2.2 has a clock offset (δt_u) from the base time. If the receiver clock is ahead, the range measurement is written as

$$\rho^i = c\,(\tau + \delta t_u) = R_i + \varepsilon \tag{2.2}$$

where ρ^i is the pseudorange measurement. With only one measurement, the user knows located on a spherical circle with radius $R_i + \varepsilon$ centered about the satellite that broadcast signals. Therefore, the intersection of three spherical circles allows computing the user position in three-dimensional space as shown in Figure 2.3. However, other intersections separated from the true user position (A) in Figure 2.3 are a function of the receiver clock offset that should be removed.

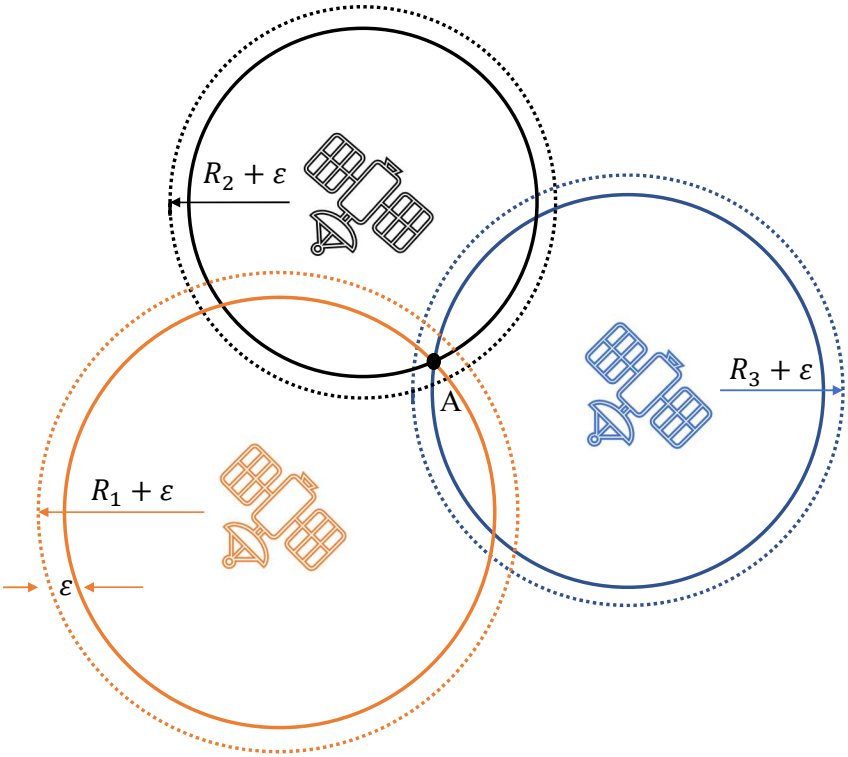

Figure 2.3: Effect of receiver clock offset on Time of Arrival (ToA) measurements (adapted from [3]).

The pseudorange measurement for the i^{th} satellite can be written as

$$\rho^i = \sqrt{(x^i - x_u)^2 + (y^i - y_u)^2 + (z^i - z_u)^2} + c\,\delta t_u \tag{2.3}$$

where x^i, y^i, z^i are the coordinates of the satellite and x_u, y_u, z_u are the user coordinates. Therefore, considering the additional unknown clock offset, at least four measurements (i.e. four satellites) are required to obtain a 3-D position solution. It has to be noted that only the receiver clock offset with synchronized satellite clocks are considered in this position solution. Furthermore, in the books [3, 18, 31], the concept of ranging using ToA measurements can be found in detail.

2.2 Signal structure

In this section, an overview of GNSS signal components is provided. Figure 2.4 shows a general block diagram of GNSS signal generation. The atomic clocks (e.g. Cs, Rb, H maser, etc.) onboard satellites sustain a consistent time reference and every GNSS signal is generated by RF carrier of which the frequency is $f_0 = 1/T_0$ Hz where T_0 is the time interval between peak-to-peak.

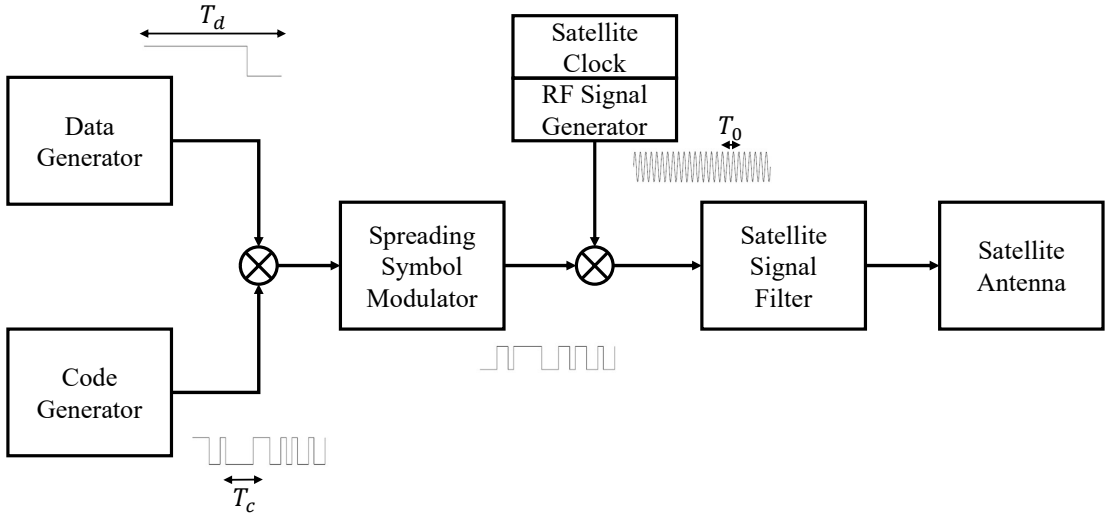

Figure 2.4: GNSS signal generation (adapted from [32]).

The navigation data containing information about the orbits and clock corrections is binary-coded (0 and 1) having a successive interval of $T_d = 1/R_d$ seconds, where R_d is the data rate in bits per second (bps).

The code generator generates the PRN ranging code sequence (i.e. spreading code) that is unique for each satellite. $f_c = 1/T_c$ is the chipping rate of the sequence of which the chip interval is T_c. Although a chip corresponds to a bit, it is called a chip since it does not hold any information [33] and the spreading code is known to the receiver.

In majority of the GNSS signals, the combination of code and navigation data are applied to the carrier by using Binary Phase Shift Keying (BPSK) modulation [18]. A BPSK modulated signal can be written as:

$$s_{\text{BPSK}}(t) \;=\; \sqrt{2P}\, s(t)\, \cos\left(2\pi f_0 t + \phi\right) \tag{2.4}$$

where P is the transmitted signal power, f_0 is the carrier frequency, ϕ is the carrier phase, and $s(t)$ is the bipolar (i.e. $+1$, -1) representation of modulo-2 addition of the spreading code and navigation data [34]. The carrier phase (ϕ) is either 0° or 180° depending on transmitted digital 0 and 1 over successive intervals of T_d seconds in time. However, in modern GNSS signals, Forward Error Correction (FEC) is applied to the navigation data to be able detect and correct error bits that may be introduced due to noise, interference and fading. Therefore, considering the redundant bits that are transmitted through the defined FEC method, common convention is to replace bit rate (R_b) with symbol rate (R_s) to distinguish data symbols from data bits [26].

In principle, the GNSS signals employ Direct Sequence Spread Spectrum (DSSS) modulation technique that involves the modulation of RF carrier with a spreading code and often with the navigation data [26]. In DSSS waveforms, having frequent phase changes created by the spreading sequence allows the receiver to reach precise distance measurement. Moreover, the spreading symbol does not have to have a constant amplitude over the chip period in a DSSS signal, as applied with rectangular chips in BPSK. For example, in Binary Offset Carrier (BOC) signals, modulation of the spreading code sequence onto the square-wave subcarrier is applied [34]:

$$\begin{aligned} s_{\text{BOC}_S}(t) \;&= s_{\text{PRN}}(t)\, \text{sign}\left[\sin\left(2\pi f_{sc} t\right)\right] \\ s_{\text{BOC}_C}(t) \;&= s_{\text{PRN}}(t)\, \text{sign}\left[\cos\left(2\pi f_{sc} t\right)\right] \end{aligned} \tag{2.5}$$

where the subscripts s and c denote the sine and cosine phasing of the BOC subcarrier, respectively. $s_{\text{PRN}}(t)$ is the bipolar representation of the spreading code sequence, f_{sc} is the subcarrier frequency, and sign is the signum function:

$$\text{sign}(x) \triangleq \begin{cases} 1, & x \geq 0 \\ -1, & x < 0 \end{cases} \tag{2.6}$$

As it is observed, BOC modulations provide additional signal design parameters compared to BPSK modulations and reaching enhanced performance is aimed considering the constraints at both transmitter and receiver sides.

Furthermore, many modern signals split the total power of one signal between two components, namely, data and pilot (i.e. dataless) that utilize different ranging codes. The motivation behind is to enable receiver to be able track GNSS signals through pilot components in more challenging environments. In order to have

robust data bit synchronization, secondary (i.e. synchronization) codes are also generated besides primary ranging codes in new generation GNSS signals.

To sum up, after the generated code and navigation data are applied to the carrier by utilizing the defined modulation, RF up-conversion is applied; then, the transmission bandwidth is restricted by the satellite filter before the signal is being transmitted by the satellite antenna. The main differences between the GNSS signals available in space are summarized in terms of DSSS modulation, code length, navigation data, and the transmitted signal power level in Table 2.2.

Table 2.2: GNSS Signals Overview [22, 23, 26, 35, 36]

Signal	Center Frequency (MHz)	Modulation Type	Component	Primary Code Length (chips)	Secondary Code Length (chips)	Tiered Code Length (ms)	Data Rate (sps)	Min. Received Signal Power (dBW)
GPS L1	1575.42	BPSK(1)	L1 C/A	1023	-	1	50	-158.5
GPS L1C	1575.42	BOC(1,1)	L1C-data	10230	-	10	100	-163.0
		TMBOC [comb. of BOC(1,1) and BOC(6,1)]	L1C-pilot	10230	1800	18000	-	-158.3
GPS L2	1227.60	BPSK(1)	L2-CM	10230	-	20	50	-161.5
		BPSK(1)	L2-CL	767250	-	1500	-	-161.5
GPS L5	1176.45	BPSK(10)	L5-I	10230	10	10	100	-157.9
		BPSK(10)	L5-Q	10230	20	20	-	-157.9
GAL E1	1575.42	CBOC(6,1,1/11)	E1-B	4092	-	4	250	-160
		CBOC(6,1,1/11)	E1-C	4092	25	100	-	-160
GAL E5a	1176.45	BPSK(10)	E5a-I	10230	20	20	50	-158
		BPSK(10)	E5a-Q	10230	100	100	-	-158
GAL E5b	1207.14	BPSK(10)	E5b-I	10230	4	4	250	-158
		BPSK(10)	E5b-Q	10230	100	100	-	-158
GAL E6	1278.75	BPSK(5)	E6-B	5115	-	1	1000	-158
		BPSK(5)	E6-C	5115	100	100	-	-158
BDS B1	1561.098	BPSK(2)	B1I	2046	-	1	50 or 500	-163
BDS B2	1207.14	BPSK(2)	B2I	2046	-	1	50 or 500	-163
BDS B3	1268.520	BPSK(10)	B3I	10230	-	10	50 or 500	-163
BDS B1C	1575.42	BOC(1,1)	B1C_data	10230	-	10	100	-159/-161*
		QMBOC(6,1,4/33)	B1C_pilot	10230	1800	18000	-	
BDS B2a	1176.45	BPSK(10)	B2a_data	10230	5	5	200	-156/-158*
		BPSK(10)	B2a_pilot	10230	100	100	-	
BDS B2b	1207.14	BPSK(10)	B2b_data	10230	-	10	100	-160/-162*
GLO L1OF	from 1598.0625 to 1605.375	FDMA - BPSK(0.511)	C/A	511	-	1	50	-161
GLO L2OF	from 1242.9375 to 1248.635	FDMA - BPSK(0.511)	C/A	511	-	1	50	-167
GLO L1OC	1600.995	BOC(5,2.5)	L1SC	?	?	?	-	-155
		BPSK(1) mux.	L1OCd	1023	2	2	250	-155
		BOC(1,1) mux.	L1OCp	4092	-	8	-	
GLO L2OC	1248.06	BOC(5,2.5)	L2SC	?	?	?	-	?
		BPSK(1) mux.	L2 CSI	?	?	?	?	?
		BOC(1,1) mux.	L2OCp	10230	50	1000	?	?
GLO L3OC	1202.025	BPSK(10)	L3OCd	10230	50	50	200	?
		BPSK(10)	L3OCp	10230	50	1000	-	?

*The received signal power levels differ depending on the broadcasting satellite type (i.e. MEO or IGSO).

In Table 2.2, BPSK(b) is the shorthand notation of BPSK modulation having a spreading code at the rate of ($b \cdot 1.023$) Mega chips per second (Mcps). BOC(a, b) modulation is created by a sine wave carrier with the modulation of a square-wave subcarrier of which the frequency is ($a \cdot 1.023$) MHz and a spreading code having ($b \cdot 1.023$) Mcps chipping rate. It has also to be noted that the transmission of DSSS signals having the same carrier frequency with different spreading sequences are referred to as Code Division Multiple Access (CDMA) while the use of different carrier frequencies to transmit multiple signals having the same spreading code sequence is known as Frequency Division Multiple Access (FDMA). As it can be seen in Table 2.2, although FDMA is only used by GLONASS, the new generation GLONASS satellites have started broadcasting CDMA signals as well to improve interoperability with other GNSSs [19].

2.2.1 GNSS frequency plan

Most GNSS signals are transmitted in $1-2$ GHz L-band of the electromagnetic spectrum. A summary of the different GNSS signals of which the signal components are provided in Table 2.2 and of which the carriers are centered at 1575.42 MHz (L1), 1227.60 MHz (L2), and 1176.45 MHz (L5) frequencies are shown in Figure 2.5.

L-band offers advantages for GNSS signals to penetrate through rain, clouds, storms, and vegetation. While in lower frequencies atmosphere causes severe fading in the received signal, at greater frequencies to diminish rain attenuation additional signal power is required [26].

2.2.2 GPS L1 C/A and L5 signals

Third civilian GPS signal L5 is being broadcast by 15 Block IIF GPS satellites as of December 2020 [35]. The L5 signal, as being a new signal with advanced features, represents an opportunity of enhanced performance for GNSS receivers.

GPS L1 Coarse/Acquisition (C/A) signal is BPSK modulated with the carrier frequency of $f_{L1} = 1575.42$ MHz, while GPS L5 signal is Quadrature Phase Shift Keying (QPSK) modulated and its carrier frequency is $f_{L5} = 1176.45$ MHz. L1 C/A and L5 transmitted signals by a satellite are modelled as:

$$s_{L1}(t) = \sqrt{2C_{L1}}c_{L1}(t)d_{L1}(t)\cos(2\pi f_{L1}t) \tag{2.7}$$

$$\begin{aligned} s_{L5}(t) =& \sqrt{C_{L5}}c_{L5_I}(t)d_{L5}(t)s_{NH_{10}}(t)\cos(2\pi f_{L5}t) \\ &+\sqrt{C_{L5}}c_{L5_Q}(t)s_{NH_{20}}(t)\sin(2\pi f_{L5}t) \end{aligned} \tag{2.8}$$

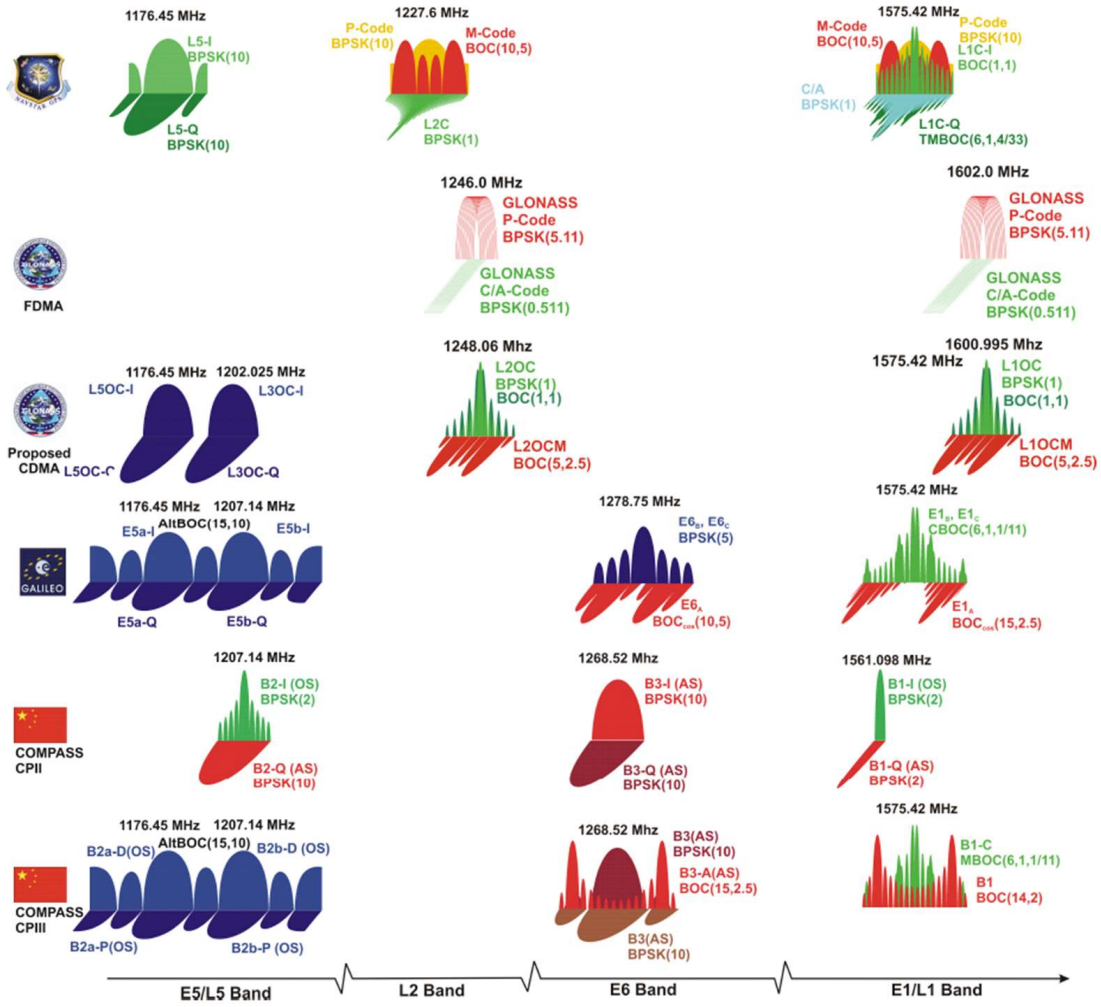

Figure 2.5: GNSS spectrum (retrieved from [32]).

where c_{L1} is the C/A code of 1 millisecond in length at the chipping rate of 1.023 Mchip/s, d_{L1} is GPS L1 C/A navigation data message at 50 bit/s, and d_{L5} is GPS L5 navigation data encoded with FEC codes at 100 sample/s. Neuman-Hofman (NH) codes ($s_{NH_{10}}$ and $s_{NH_{20}}$) are secondary codes of GPS L5 signal and are 10-bits and 20-bits long, respectively, with the code rate of 1 kHz. c_{L5_I} and c_{L5_Q} are PRN codes of in-phase and quadrature channels which are 1 millisecond in length with a chipping rate of 10.23 Mchip/s. C_{L1} and C_{L5} correspond to the RF powers of L1 C/A and L5 signals, respectively.

L5 signal includes a navigation data at only in-phase component (i.e. data channel), while quadrature component, namely the pilot channel, carries no message. Furthermore, L5 signal has longer spreading codes for both in-phase and quadrature

channels, and higher transmitting power compared to the L1 C/A signal. According to the interface specification document for the block IIF satellites, while the received minimum RF signal strength is −158.5 dBW for the GPS L1 C/A signal, the L5 signal strength is −154.9 dBW (i.e. −157.9 dBW on each channel, namely, in phase and quadrature) [37]. The results in [38] show that experimentally receiving a mean of 3.5 dB higher power for GPS L5 compared to GPS L1 C/A could be measured. Having a data-free pilot channel, which uses longer codes at higher chipping rates with NH secondary codes, and higher transmitted power than L1 C/A signal, it could have better performance in GNSS receiver. Since the code on L5 is ten times faster than the C/A code, the main peak in the auto-correlation function is sharper by a factor of ten and cross-correlation side lobes are lower than that for the C/A code. Hence it provides an improvement in the signal tracking capability [1]. Moreover, data-free signal components are useful in low signal-to-noise ratio environments due to the fact that squaring loss caused by the squaring operation, that is used to remove the data modulation, is reduced with the increasing integration time.

2.2.3 Galileo E1 and E5 signals

In Galileo signals, as being different from GPS signals, BOC modulated signals that are characterized by rectangular sub-carrier to shape the signal spectrum, increase frequency separation, and improve tracking performance were developed [39].

Galileo E1 Open Service (OS) signal is Composite Binary Offset Carrier (CBOC) modulated with the carrier frequency of 1575.42 MHz. It comprises of two signal components, namely E1-B (data-component) and E1-C (pilot-component) [23]:

$$\begin{aligned} s_{E1}(t) = 1/\sqrt{2}\,(e_{E1-B}(t)\,(\alpha\, sc_{E1-B,a}(t) + \beta\, sc_{E1-B,b}(t))) \\ - 1/\sqrt{2}\,(e_{E1-C}(t)\,(\alpha\, sc_{E1-C,a}(t) - \beta\, sc_{E1-C,b}(t))) \end{aligned} \tag{2.9}$$

where $sc_X(t) = \text{sign}\,(\sin\,(2\pi R_{s,X} t))$ is the sub-carrier component with rates $R_{s,X,a}$ and $R_{s,X,b}$ that are equal to 1.023 MHz and 6.138 MHz, respectively. The parameters $\alpha = \sqrt{10/11}$ and $\beta = \sqrt{1/11}$ are chosen so that the combined power of the sub-carrier components equals 1/11 of the total power [23]. Galileo E1 signal has increased transmitted power (−157.0 dBW) compared to GPS L1 C/A signal (−158.5 dBW), which means improved robustness against signal impairments [40].

The wide-band Galileo E5 signal is centered at 1191.75 MHz and consists of two individual signals, namely, Galileo E5a of which carrier frequency is 1176.45 MHz and E5b that is centered at 15.345 MHz above the E5 carrier. E5 combined signal is generated coherently using the Alternative Binary Offset Carrier (AltBOC) modulation scheme. E5 signal occupies a total bandwidth of 51.15 MHz with two

main lobes of the AltBOC signal comprising of E5a and E5b. The specified minimum received power by using an ideally matched Right-Hand Circularly Polarized (RHCP) 0 dBi antenna is −155 dBW for both E5a and E5b signals [23]. Moreover, the E5 signal can also be described as 8-Phase Shift Keying (PSK) signal, comprised of two QPSK E5a and E5b signals. The analytical baseband complex envelope representation of the E5 signal is given in [23]:

$$\begin{aligned} s_{E5}(t) =& 1/2\sqrt{2}\,(e_{E5a-I}(t) + j\,e_{E5a-Q}(t))\,[sc_{E5-S}(t) - j\,sc_{E5-S}\,(t - T_{s,E5}/4)] + \\ & 1/2\sqrt{2}\,(e_{E5b-I}(t) + j\,e_{E5b-Q}(t))\,[sc_{E5-S}(t) + j\,sc_{E5-S}\,(t - T_{s,E5}/4)] + \\ & 1/2\sqrt{2}\,(\bar{e}_{E5a-I}(t) + j\,\bar{e}_{E5a-Q}(t))\,[sc_{E5-P}(t) - j\,sc_{E5-P}\,(t - T_{s,E5}/4)] + \\ & 1/2\sqrt{2}\,(\bar{e}_{E5b-I}(t) + j\,\bar{e}_{E5b-Q}(t))\,[sc_{E5-P}(t) + j\,sc_{E5-P}\,(t - T_{s,E5}/4)] \end{aligned} \tag{2.10}$$

where the dashed signal components $\bar{e}_{E5a-I}$, $\bar{e}_{E5a-Q}$, $\bar{e}_{E5b-I}$, and $\bar{e}_{E5b-Q}$ represent the defined product signals of the binary components e_{E5a-I}, e_{E5a-Q}, e_{E5b-I}, and e_{E5b-Q} that are the signal components containing the navigation data stream and ranging codes. sc_{E5-S} and sc_{E5-P} are the four-valued sub-carrier functions for the single and product signals, and the coefficients and functions are defined in Galileo Interface Control Document (ICD) [23].

2.3 GNSS receiver architecture

A functional block diagram of GNSS user equipment, in other words, GNSS receiver is shown in Figure 2.6.

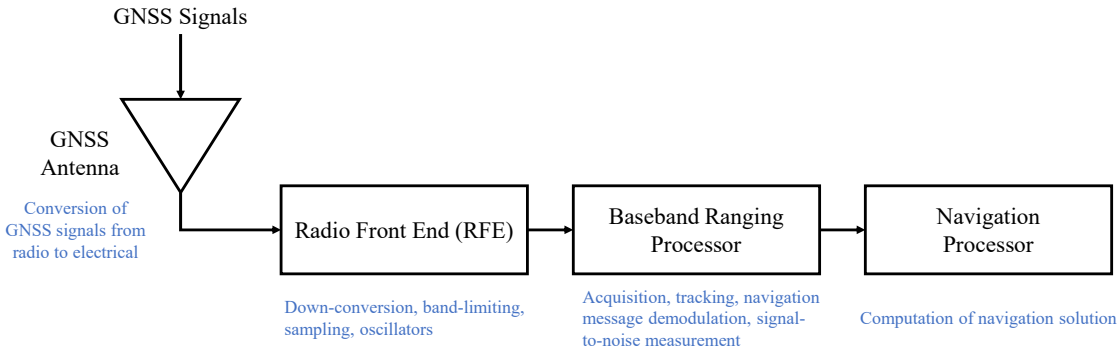

Figure 2.6: GNSS receiver functional block diagram (adapted from [18]).

As it is presented in Figure 2.6, GNSS receiver can be split into four main parts: GNSS antenna, RFE, baseband processor that performs signal acquisition and tracking, and navigation processor computing user PVT. GNSS antenna is the first element in the signal path and it receives the electromagnetic waves transmitted

from the satellites. In the following subsections, the aforementioned stages are detailed.

2.3.1 Radio front end

After the GNSS signals are received by the antenna, the signals are amplified, filtered, down-converted to Intermediate Frequency (IF) and sampled. This process performed at the front-end stage is depicted in Figure 2.7.

In a GNSS receiver, RFE stage determines the cost, size and power consumption of the receiver and its design has the primary importance [41]. The key components are the Low Noise Amplifier (LNA), the RF filter used for image rejection, the IF filter eliminating unwanted spectral parts, and the Local Oscillator (LO) used for down-conversion. The design and the selection of the components that satisfy the requirements such as phase noise, stability, and noise figure through the front-end chain gain importance.

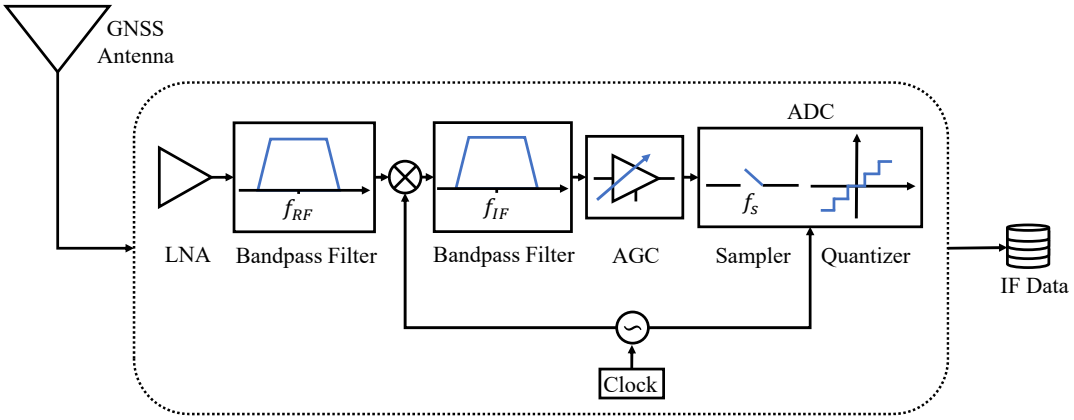

Figure 2.7: Radio front end (RFE) architecture.

Each transmitted satellite signal is separately delayed, attenuated and affected by Doppler and the sampled signal in the front-end is the combination of the signals from different visible satellites. Then, the received signal from one satellite in different frequencies (e.g. L1 and L5) can be modeled as:

$$\begin{aligned} r_{L1}[n] =& r_{L1}(nT_s) \\ =& \sqrt{2A_{L1}} c_{L1}(nT_s - \tau_{L1,0}) d_{L1}(nT_s - \tau_{L1,0}) \\ & \cos(2\pi(f_{IF,L1} + f_{L1,0})nT_s - \varphi_{L1,0}) \\ & + \eta_{L1,IF}(nT_s). \end{aligned} \tag{2.11}$$

$$
\begin{aligned}
r_{L5}(nT_s) = &\sqrt{A_{L5}} c_{L5_I}(nT_s - \tau_{L5,0}) d_{L5}(nT_s - \tau_{L5,0}) \\
&s_{NH_{10}}(nT_s - \tau_{L5,0}) \\
&\cos(2\pi(f_{IF,L5} + f_{L5,0})nT_s - \varphi_{L5,0}) \\
&+\sqrt{A_{L5}} c_{L5_Q}(nT_s - \tau_{L5,0}) s_{NH_{20}}(nT_s - \tau_{L5,0}) \\
&\sin(2\pi(f_{IF,L5} + f_{L5,0})nT_s - \varphi_{L5,0}) \\
&+\eta_{L5,IF}(nT_s).
\end{aligned}
\tag{2.12}
$$

where τ_0, f_0, φ_0 are the code delay, Doppler frequency offset, and carrier phase respectively. T_s is the sampling period which is equal to $1/f_s$ where f_s is the sampling frequency. $f_{IF,L1}$ and $f_{IF,L5}$ are the IF values of the RFE for GPS L1 C/A and L5 signals, respectively. A_{L1} and A_{L5} are the signal powers of received GPS L1 C/A and L5 signals, respectively. $\eta_{L1,IF}(nT_s)$ and $\eta_{L5,IF}(nT_s)$ are the down-converted and filtered noise components that are assumed to be Additive White Gaussian Noise (AWGN).

GNSS receiver algorithms are responsible for the synchronization of the received signal and the locally generated signal to demodulate the navigation data (d_{L1} and d_{L5}) according to a two-stage architecture made of acquisition and tracking.

Depending on the sample rate and quantization type applied in the Analog-to-Digital Converter (ADC), a data link providing a continuous stream of IF data to the baseband processor has to be designed and implemented for real-time processing in commercial receivers. However, mostly for software GNSS receiver implementations, IF data storage is realized so as to be able post-process the IF data.

2.3.2 Signal acquisition

At the acquisition stage, the objective is to process the incoming digitized signals to find out all the visible satellites. Rough synchronization of the locally generated signal with the incoming one is performed and the estimated Doppler frequency (f_D) and code phase (τ) values of all the acquired satellites are fed to the tracking stage.

Figure 2.8 shows the general structure of a coherent acquisition using a coherent integration time equal to one primary code period and K non-coherent accumulations. While acquiring a modern GNSS signal (e.g. GPS L5) having both data and pilot signal components, the input signal can be correlated with the pilot or the data channel. In case of data-pilot acquisition, the number of correlators in Figure 2.8 must be doubled in number in order to include the processing of both the data and pilot channels in two separate channels. Although it will cause an increase in the computational burden, it will increase as well the available signal power. In the case of processing only the pilot signal, the advantage of the absence of the navigation data is exploited.

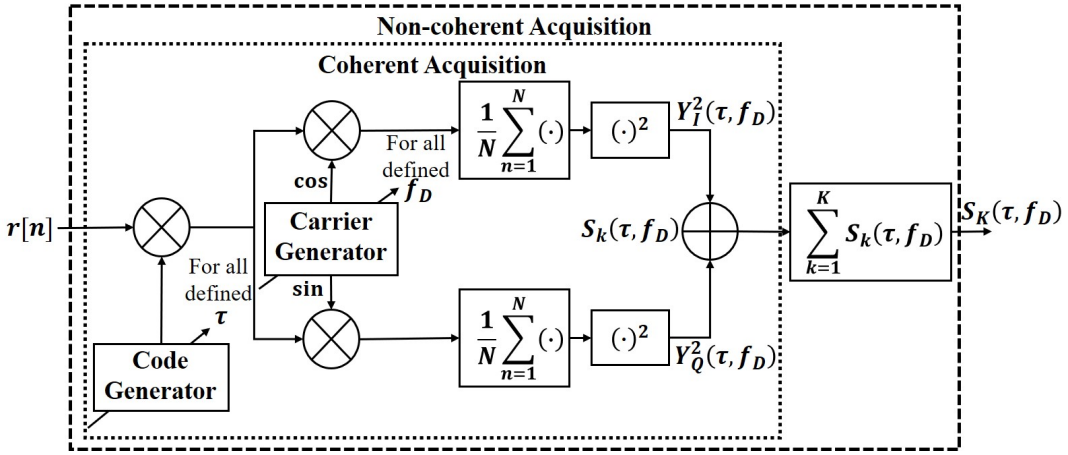

Figure 2.8: GPS signal acquisition block for coherent and non-coherent cases.

At the acquisition stage, different locally generated Doppler frequency (f_D) and code delay (τ) values are tested to estimate the delay and Doppler shift of the incoming signal. For all possible combinations (τ, f_D), the correlator outputs in Figure 2.8 for the pilot and the data channel acquisitions during the coherent integration in the case of no sign transition are expressed as [42]:

$$Y_{I,p_k}(\tau, f_D) \approx \sqrt{\frac{C}{4}} R(\Delta T_k) \frac{\sin(\pi \Delta F_k T_c)}{\pi \Delta F_k T_c} \cos(\Delta\theta_k) + \eta_{I,p_k} \tag{2.13}$$

$$Y_{Q,p_k}(\tau, f_D) \approx \sqrt{\frac{C}{4}} R(\Delta T_k) \frac{\sin(\pi \Delta F_k T_c)}{\pi \Delta F_k T_c} \sin(\Delta\theta_k) + \eta_{Q,p_k} \tag{2.14}$$

$$Y_{I,d_k}(\tau, f_D) \approx \sqrt{\frac{C}{4}} d_k R(\Delta T_k) \frac{\sin(\pi \Delta F_k T_c)}{\pi \Delta F_k T_c} \cos(\Delta\theta_k) + \eta_{I,d_k} \tag{2.15}$$

$$Y_{Q,d_k}(\tau, f_D) \approx \sqrt{\frac{C}{4}} d_k R(\Delta T_k) \frac{\sin(\pi \Delta F_k T_c)}{\pi \Delta F_k T_c} \sin(\Delta\theta_k) + \eta_{Q,d_k} \tag{2.16}$$

where subscripts d and p correspond to the data and the pilot channels, respectively. Subscript k is the accumulation number which corresponds to the duration between kT_c and $(k+1)T_c$ where T_c corresponds to the coherent integration time interval. $R(\Delta T_k)$ is the normalized k-th cross-correlation between the incoming and the generated codes, ΔT_k is the k-th sampled code delay difference between the generated local one (τ) and the incoming one (τ_0). ΔF_k is the k-th frequency difference between the locally generated carrier and the incoming one: $\Delta F_k = f_0 - f_D$. $\Delta\theta_k$ is unknown residual phase value. η_{I,p_k}, η_{Q,p_k}, η_{I,d_k} and η_{Q,d_k} are k-th Gaussian noise terms. d_k is the sign of the k-th navigation data bit which are only included in the data channels.

Having obtained the correlations in each branch, the test statistics, namely, the Cross Ambiguity Function (CAF), is computed by squaring and summing each result so as to remove the dependence on the unknown phase residual ($\Delta\theta_k$):

$$\begin{aligned} S_k(\tau, f_D) &= Y^2_{I,p/d_k}(\tau, f_D) + Y^2_{Q,p/d_k}(\tau, f_D) \\ &\approx \left| \sqrt{C/4}\, R(\Delta T_k)\, \mathrm{sinc}(\pi \Delta F_k T_c) + \eta_{IQ_k} \right|^2 \end{aligned} \tag{2.17}$$

where η_{IQ_k} is the resulting noise contribution. By employing K independent correlations, non-coherent acquisition method can be implemented and the test statistics is changed to $S_K(\tau, f_D)$:

$$S_K(\tau, f_D) = \sum_{k=1}^{K} S_k(\tau, f_D) \tag{2.18}$$

The presence of a satellite signal is determined through a decision process considering a preset decision threshold (T_h):

$$\max_{\tau, f_D} |S_K(\tau, f_D)|^2 > T_h \tag{2.19}$$

where the decision threshold (T_h) is determined considering the noise floor and controlling the false alarm probability. One of the performance comparison parameters in the acquisition stage is the peak-to-floor ratio. It is computed as by considering the test statistics parameters in (2.17) or (2.18):

$$\alpha_{max} = 20 \log_{10} \left(\frac{\max(S_K)}{\max(S_{floor})} \right) \tag{2.20}$$

where S_{floor} is the set of CAF values outside of the main peak. Since the detection process deals with distinguishing the presence of the satellite signal from the noisy data, ROC curve that is a plot of the detection probability versus false alarm probability and ROC analysis are also used for performance assessment and threshold setting.

2.3.3 Signal tracking

In a GNSS receiver, after having obtained the rough synchronization of code phase ($\hat{\tau}^{(A)}$) and Doppler frequency ($\hat{f}_D^{(A)}$) of the acquired satellite signals, the values are fed to the tracking stage for code and frequency estimates refinement.

The motivation of the signal tracking stage is to strip off the carrier and the spreading code by tracking the signal to obtain whole navigation data. While in the code tracking loop aligned carriers are utilized, aligned spreading codes are used to remove the carrier synchronously in the carrier tracking loop. In order to estimate

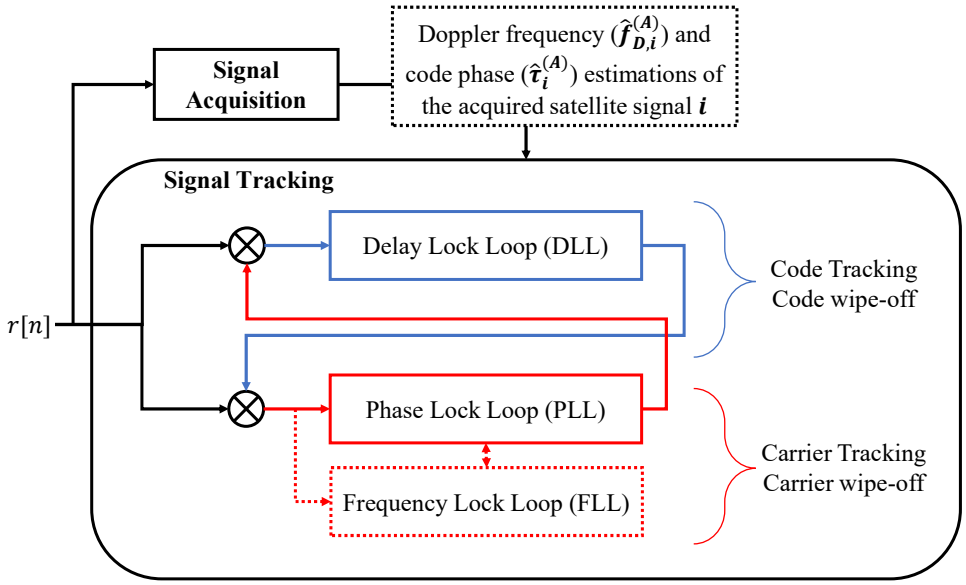

Figure 2.9: Signal tracking stage architecture.

the signal parameters (e.g. code delay, Doppler frequency, carrier phase, etc.) and track their variations over time, Delay Lock Loop (DLL) and PLL are used in a coupled way as depicted in Figure 2.9.

Code tracking

A general code tracking structure is given in Figure 2.10. In code tracking, after carrier is removed using the local replica coming from the PLL, three local spreading codes (i.e. replicas), namely, early ($c_E[n]$), prompt ($c_P[n]$), and late ($c_L[n]$), are generated and correlated with the incoming signal.

The local replica codes are generated having a pre-defined Δ-chip spacing between early and late replicas:

$$\begin{aligned} c_E[n] &= c\left(nT_s - (\hat{\tau}^A + \bar{\tau} + \Delta/2)\right) \\ c_P[n] &= c\left(nT_s - (\hat{\tau}^A + \bar{\tau})\right) \\ c_L[n] &= c\left(nT_s - (\hat{\tau}^A + \bar{\tau} - \Delta/2)\right) \end{aligned} \tag{2.21}$$

where $\bar{\tau}$ is the residual delay estimated by the DLL while $\hat{\tau}^{(A)}$ is obtained from acquisition stage. Δ is less than or equal to chip duration T_c and the case of having $\Delta = 0.5T_c$ spacing is picturized in Figure 2.11.

As it can be seen in Figure 2.11, when the prompt replica code is aligned with the incoming code, the highest peak of the correlation is located at the prompt

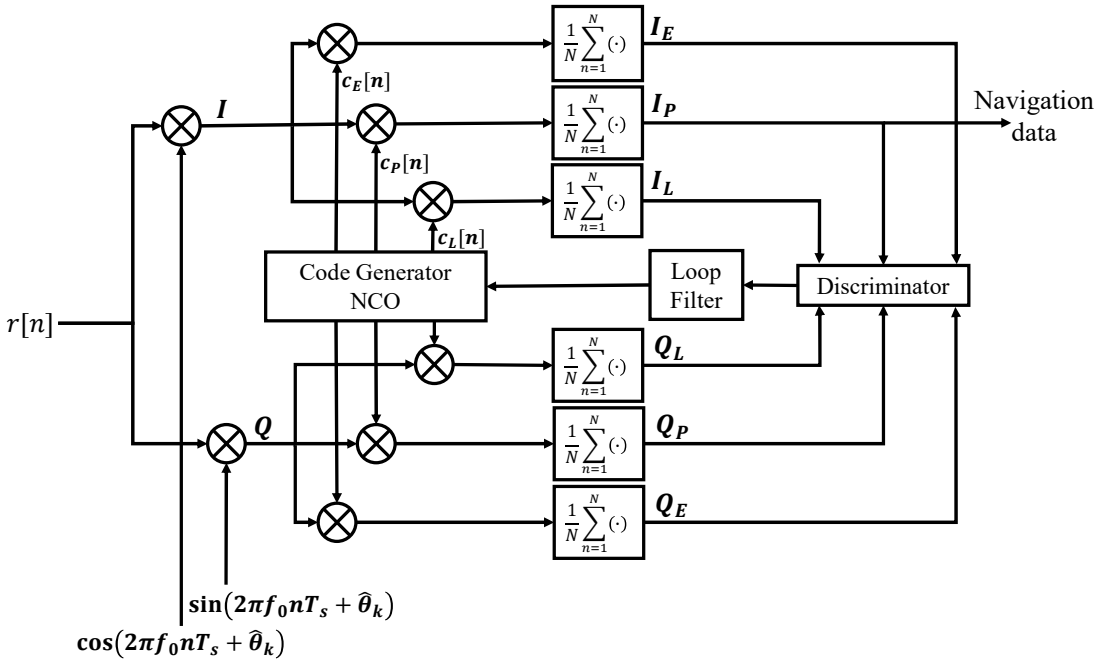

Figure 2.10: Signal code tracking block diagram.

replica and no error is generated by the discriminator. In other cases, the DLL discriminator outputs the relevant error [43]. After in-phase (I) and quadraphase (Q) accumulated correlator outputs are obtained, they feed to a discriminator function to calculate a measurement of the code tracking error (i.e. residual delay error) $\delta\tau_k$. The most commonly used discriminators are the Dot-Product Power (DPP), Early-minus-Late Power (ELP), and Early-minus-Late Envelope (ELE) noncoherent discriminator [18]:

$$\begin{aligned}
\delta\tau_{DPP,k} &= (I_E - I_L)\, I_P + (Q_E - Q_L)\, Q_P \\
\delta\tau_{ELP,k} &= \left(I_E^2 + Q_E^2\right) - \left(I_L^2 + Q_L^2\right) \\
\delta\tau_{ELE,k} &= \sqrt{I_E^2 + Q_E^2} - \sqrt{I_L^2 + Q_L^2}
\end{aligned} \tag{2.22}$$

where k is used to index the steps of the DLL operation. I_E, Q_E, I_L, and Q_L are outputs of the correlators shown in Figure 2.10. The output error of the normalized ELP discriminator is linear over 1-chip range as it is seen in Figure 2.11 and normalization removes the amplitude sensitivity so that improves the performance under rapidly changing Signal-to-Noise Ratio (SNR) conditions [26]. Chip-spacing is a key design parameter that should be carefully set considering the presence of both noise and multipath. Moreover, the loop filter that reduces the noise and is designed with selection of the parameters (e.g. filter order and bandwidth) also plays an important role in the code tracking performance.

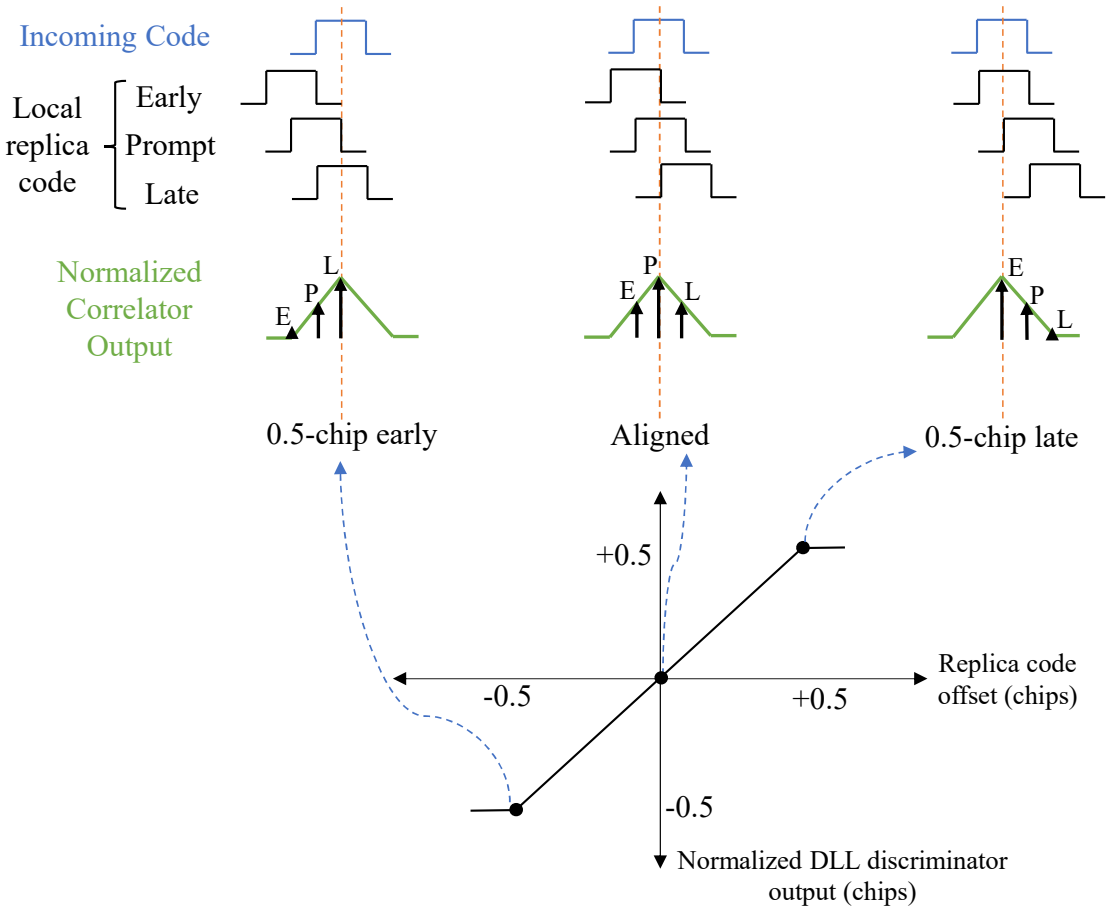

Figure 2.11: Early-prompt-late replicas, correlator outputs, and early-minus-late DLL discriminator (adapted from [43]).

Carrier tracking

The general structure of the carrier tracking loop is given in Figure 2.12. While tracking the carrier signal, the spreading code of the incoming signal is tried to be aligned with the locally generated code at the same time. The aim is to have all the power in the in-phase (I) branch. In principle, the operation and correlator outputs are the same as in the architecture of Figure 2.8. In this case, the carrier phase error is minimized. This is possible when the correlation value in the in-phase branch (I_k) is maximum and in the quadrature-phase branch (Q_k) is zero.

In Figure 2.12, the $c_p[n]$ is the prompt spreading code generated at the code tracking loop and the alignment includes a code delay estimation error ($\delta\tau$) which is also included in the tracking correlator output equations:

$$I_{k,p} = A_k R_k(\delta\tau)\frac{\sin(\pi T\delta f_k)}{\pi T\delta f_k}\cos(\delta\varphi_k) + \eta_{I,p_k} \tag{2.23}$$

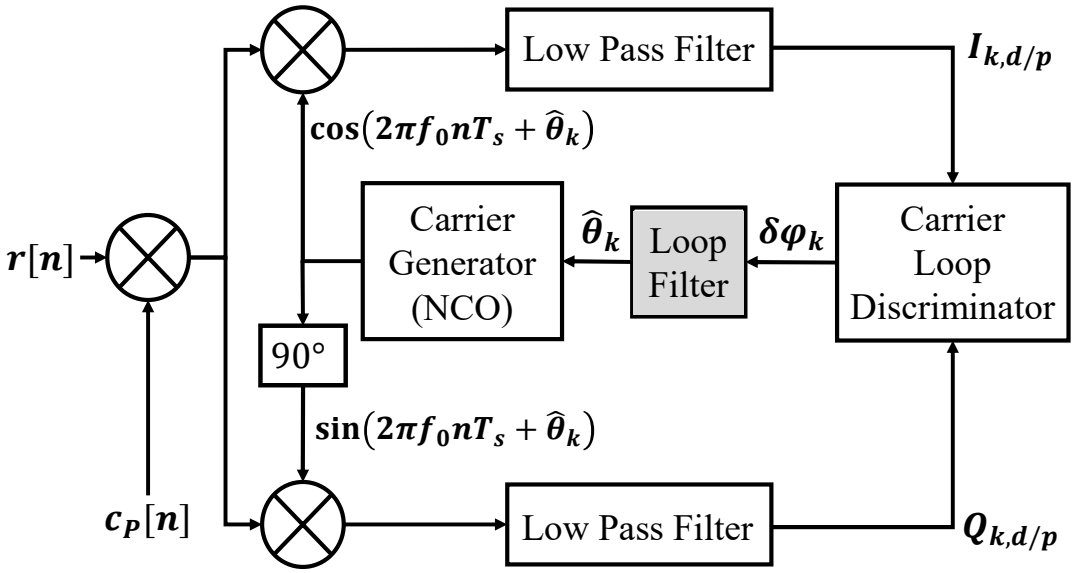

Figure 2.12: Signal carrier tracking block diagram.

$$Q_{k,p} = A_k R_k(\delta\tau)\frac{\sin(\pi T\delta f_k)}{\pi T\delta f_k}\sin(\delta\varphi_k) + \eta_{Q,p_k} \tag{2.24}$$

$$I_{k,d} = A_k R_k(\delta\tau) d_k \frac{\sin(\pi T\delta f_k)}{\pi T\delta f_k}\cos(\delta\varphi_k) + \eta_{I,d_k} \tag{2.25}$$

$$Q_{k,d} = A_k R_k(\delta\tau) d_k \frac{\sin(\pi T\delta f_k)}{\pi T\delta f_k}\sin(\delta\varphi_k) + \eta_{Q,d_k} \tag{2.26}$$

where subscripts d and p correspond to the data and the pilot channels (e.g. GPS L5 signal), respectively. $I_{k,d/p}$ and $Q_{k,d/p}$ are in-phase and quadrature correlator outputs. R is the correlation of the locally generated prompt replica code with the incoming code, d_k is the polarity of the k-th navigation data-bit when data channel is considered, δf is the frequency estimation error. A PLL discriminator computes the difference between the phase of incoming signal and locally generated signal. A commonly used two-quadrant Costas PLL discriminator outputs the phase error as:

$$\delta\varphi_k = \tan^{-1}\left(\frac{Q_{k,d/p}}{I_{k,d/p}}\right) \tag{2.27}$$

where $\delta\varphi_k$ is the average carrier phase estimation error over the coherent integration time (T). After the loop filter, which reduces the noise, A is the carrier amplitude in one branch and η_{I,p_k}, η_{Q,p_k}, η_{I,d_k}, and η_{Q,d_k} are independent Gaussian noise terms. As shown in Figure 2.12, a Numerically Controlled Oscillator (NCO) generates a sinusoid of which phase $\widehat{\theta}_k$ is related to filtered discriminator output ($\delta\widehat{\varphi}_k$). $\delta\varphi_k$,

the average carrier phase error, is the difference between the one estimated by NCO ($\widehat{\theta}_k$) and the phase of the incoming signal (θ_k).

In PLL loop filter design, there is a trade-off in the decision of the integration time (T) and loop bandwidth (B_n) besides the choice of the filter order. The selection of the parameters is discussed in Appendix A.2.1.

2.3.4 Computation of user position

After the signal tracking is successfully achieved by synchronizing the local code and carrier with the incoming signal, the navigation data samples are extracted by wiping off the carrier and code from the incoming signal. Thus, as it is shown in Figure 2.10, the in-phase prompt correlator output (I_P) contains the navigation data sequence to be used for position computation. Figure 2.13 shows the block diagram of the computation of user position.

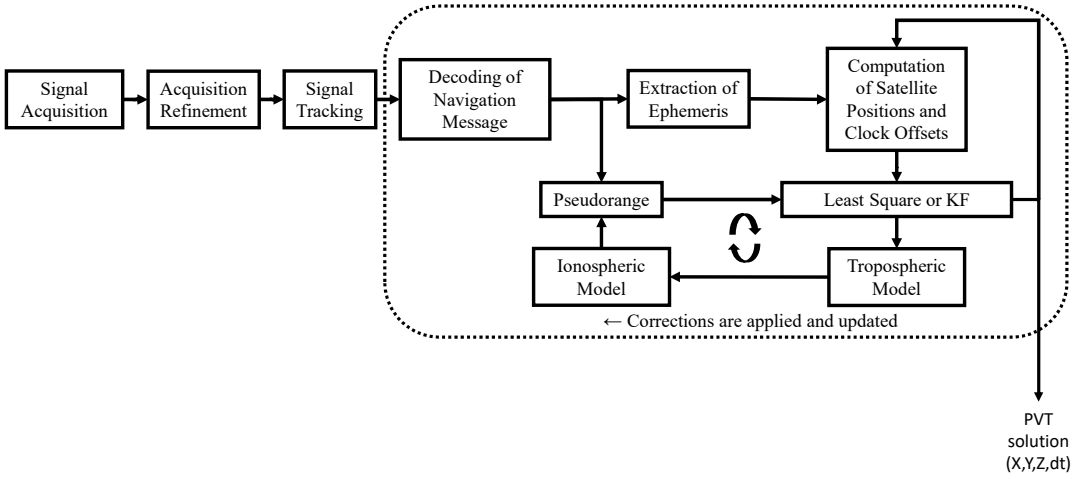

Figure 2.13: Block diagram of the computation of user position.

In decoding the navigation message, firstly the bit synchronization is realized by considering the secondary code (e.g. NH) phase, the navigation data rate (e.g. 50 bps, 100 bps), and error correction technique (e.g. FEC) of the processed signal with the employed tracking integration time (e.g. 1 ms, 10 ms, etc.) in the receiver. After the navigation bits are obtained through some bit synchronization techniques (e.g. Histogram method, K-P method, Viterbi algorithm, etc.) of which a summary can be found in [44], they are decoded by following the scheme defined in the related ICD of the GNSS system. Different GNSS systems have different structured navigation messages defined in the ICDs. However, mostly the beginning of a message block (e.g. frame, sub-frame, page, etc.) starts with a synchronization word (SW) or in other words a preamble. Identifying the preamble is called frame synchronization.

In the receiver implementation, tracking each satellite signal is realized through

an assigned channel individually. After choosing a reference channel, the preamble locations in the processed samples of the remaining channels are compared to each other to set initial pseudorange measurements. The signal travel time from the satellites to the Earth is around $65 - 83$ ms [33] and the earliest detected SW belongs to the closest satellite. However, the relative pseudorange does not contain any receiver clock error, and timing information cannot be extracted [43]. After decoding the navigation data, by computing the time-count parameters in the navigation data, accounting for clock biases, and utilizing the obtained code-delay measurements from the DLL, a better pseudorange is approximated [27]. The basic observation equation for the pseudorange (ρ_u^k) between the satellite (k) and the receiver (u) is [33]

$$\rho_u^k = d_u^k + c\left[\delta t_u - \delta t^k\right] + I_u^k + T_u^k + e_u^k \tag{2.28}$$

where δt_u and δt^k are the receiver and the satellite clock offsets, respectively. I_u^k and T_u^k are ionospheric and tropospheric propagation delays. e_u^k is the observational error. d_u^k is the geometrical range that is computed as

$$d_u^k = \sqrt{(x^k - x_u)^2 + (y^k - y_u)^2 + (z^k - z_u)^2} \tag{2.29}$$

where x_u, y_u, z_u are the user coordinates to be found. The position of the satellite (x^k, y^k, z^k) are computed from the ephemeris.

Each satellite transmits its unique ephemeris parameters that consist of the orbital elements (i.e. Keplerian parameters) and clock offset for a specific epoch. It allows computing the Earth Centered Earth Fixed (ECEF) coordinates of the satellite's antenna phase center position. The broadcast data is updated every specific duration (e.g. 30 minutes, $2 - 3$ hours). As being different from other GNSS systems, in GLONASS ephemeris, the state vector (position and velocity) of the satellite along with corrections in the Earth-fixed PZ90 coordinate system is provided [19]. In any case, the positions of the satellites (x^k, y^k, z^k) are computed by using the ephemeris data and the future satellite positions can be predicted until recent ephemeris data are downloaded. Satellite clock offset (δt^k) are also computed from the ephemeris that includes the clock information as coefficients (e.g. the satellite clock offset, clock drift and clock drift rate) of a polynomial.

When the satellite signals travel through the atmosphere, due to especially ionospheric and tropospheric effects a propagation delay is observed. The ionospheric (I_u^k) and tropospheric (T_u^k) propagation delays can be approximated by utilizing several empirical models whose coefficients are part of the broadcast ephemeris. Thus, the atmospheric effects are tried to be mitigated in the range measurements.

In Equations 2.28 and 2.29, there are four unknowns: $x_u, y_u, z_u, \delta t_u$ and the error term e_u^k that has to minimized. Therefore, at least four pseudorange measurements are needed. The most commonly used algorithm for position computation is based on the least-squares method since there are generally more observations than

unknowns [33]. By performing iterative techniques, the pseudorange measurement equations are solved based on linearization.

2.4 Implementation of a multi-frequency multi-constellation SDR GNSS receiver

A general SDR based GNSS receiver high-level block diagram is shown in Figure 2.14. All the signal and measurement processing techniques (e.g. signal acquisition, tracking, scintillation analysis, navigation data processing, etc.) can be implemented in software. IF data, depicted in Figure 2.14, is the most basic type of GNSS data obtained after the RFE stage [45]. IF samples can be processed in real-time or stored for post-processing.

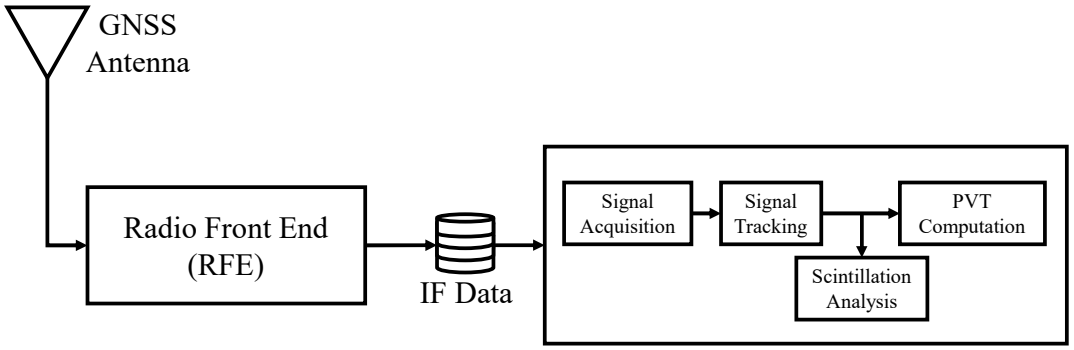

Figure 2.14: GNSS receiver architecture.

In the framework of this thesis study, a non-real-time fully software GNSS receiver has been implemented. The details of the implemented software GNSS receiver in MATLAB [46] and the designed Graphical User Interface (GUI) are shared in Appendix A. The receiver has been developed with a modular architecture and is capable to process GPS L1 C/A, GPS L2-CM, GPS L5 I-Q, Galileo E1b, and Galileo E5a-I signals.

The receiver also includes an analysis tool for scintillation phenomena to output the amplitude and phase scintillation indices, the spectral index of phase scintillation, and the spectral strength of the phase, which are discussed in Section 3.1. The performance analysis of the implemented different acquisition algorithms for GPS L1 C/A and L5 signals is examined in Section 4.1. Nonetheless, when the tracking stage is considered, the design of the signal carrier tracking filter and selection of parameters are detailed in Appendix A.2.1. Moreover, the implementation of KF-based PLL in which the output of the discriminator is used to map the correlator outputs for the estimation of state errors is shared in Appendix A.2.2.

In the SDR approach, processing of the stored IF data allows the possibility to replay the original scenario. For example, the availability of the collected IF data

related to rare scintillation events makes the analysis of data with having a possibility to replay the original event possible, and hence it enables the development of advanced and innovative signal processing techniques to detect and mitigate the effects [47]. It also has provided a flexibility to consider the recent developments in the AI world for signal processing and outlier detections. Furthermore, besides the benefits of the SDR operation such as interoperability, multi-functionality, compactness, and modular architecture design with ease of upgrades, there are also challenges in the implementations [48].

The challenge of SDR implementations in GNSS

SDR concept and the first reconfigurable architectures are defined in Joe Mitola's pioneering works [49, 50] in 1993 and 1995. The ideal software radio interoperates with any communication service in its RF band and the software radio reconfigures itself to the appropriate signal format by running a different algorithm [49]. It has been accomplished through a combination of techniques that are applied in the RF front-end stage and the employed bit-stream processing functions in the general-purpose programmable processors [50]. The resultant software-defined radio extends the evolution of programmable hardware with increasing flexibility via increased programmability [50]. As Mitola had foreseen that this kind of flexibility has opened opportunities for reduced costs and improved services for civilian and military applications as well.

The first complete GPS receiver implementation is described by Dennis Akos in 1997 [33]. Software radio GNSS receivers are being used since many years, mainly as research tools or as tools at the early stage of the design process. They can be implemented as software defined, or fully software receivers, depending on the computational burden of the processing and on the real-time/non real-time requirements. In [51], three categories of the architectures, namely, the classic architecture, hybrid architecture, and fully software architecture, are identified among the variety of solutions.

In the *classic architecture*, whereas a Field Programmable Gate Array (FPGA) is used to perform high-rate massive operations (e.g. correlations), the acquisition/tracking stages and positioning software are implemented in the Digital Signal Processor (DSP). A PC can also be used for the user interface and configuration functions. In the *hybrid architecture*, the receiver is implemented partially in the FPGA and partially through the software running on a General Purpose Processor (GPP). Positioning, user interface and receiver management functions are realized in the PC thanks to the high-speed data connection provided by the FPGA. *Fully software architecture* implementation is based on the software running on a GPP (e.g. PC). The connection between the RF front-end the PC is generally realized through a USB port. In the case of near real-time implementations, FPGA might be used for high speed sample transfer. In [51], a comparative list of available

solutions in the literature can be found.

As it is discussed in Section 2.3.1, the RFE stage determines the cost, size, and power consumption of the receiver. One of the challenges is related to the sampling rates. Timing and synchronization should be required to be maintained within the radio [48]. The capacity requirements associated with the IF data and high data rates are other main challenges [45]. By considering the sample rate and quantization type applied in the ADC, a data link (e.g. PCI, USB, Ethernet, etc.) providing a continuous stream of IF data for real-time processing or an IF data storage system for post-mission processing has to be designed. In these cases, although a higher sample rate that basically provides more measurements is tended to be preferred, it can pose a challenge in size, weight, power, and budget requirements. Furthermore, sustaining required data-rate rate across inter-processor interfaces is difficult [50]. In the software implementation side, the possibilities of the alteration or the destruction of the configuration data and the overuse of processing and memory resources should be taken into account carefully [48].

2.5 Overview of GNSS error sources

A variety of GNSS error sources are picturized in Figure 2.15. These errors corrupt the range measurements and hence degrade overall position accuracy.

As it is mentioned in Section 2.2, the atomic clocks onboard GNSS satellites provide a consistent time reference. Although these clocks are highly stable, they do drift a small amount and they are not perfectly synchronized with the related GNSS system time. With the clock corrections provided by the control segment, the satellite provides the users an estimate of its clock offset. Furthermore, while the satellite transmits its Keplerian elements, they are almost exactly but with a small error broadcasted and this error grows from the time of upload by a control station until the next upload [52]. The geographical extent of the control-segment monitoring networks gains importance in ephemeris determination and hence these errors change with the user location [26].

In signal generation, as it is discussed in Section 2.2 and shown in Figure 2.4, it is expected that each ranging code generated onboard the satellite experiences a different delay from signal generation to output from the antenna because of the different analog and digital signal paths. Therefore, all satellite signals have a unique offset from the GNSS system time, this is also defined as the equipment group delay [26].

Table 2.3 shows the estimates of the pseudorange error sources and the accuracy of the pseudorange value is termed the User Equivalent Range Error (UERE). The aforementioned errors are listed under space/control segment with 1σ error values in meters. The error components are considered independent and identically distributed from satellite to satellite. Moreover, the Root Sum Squared (RSS)

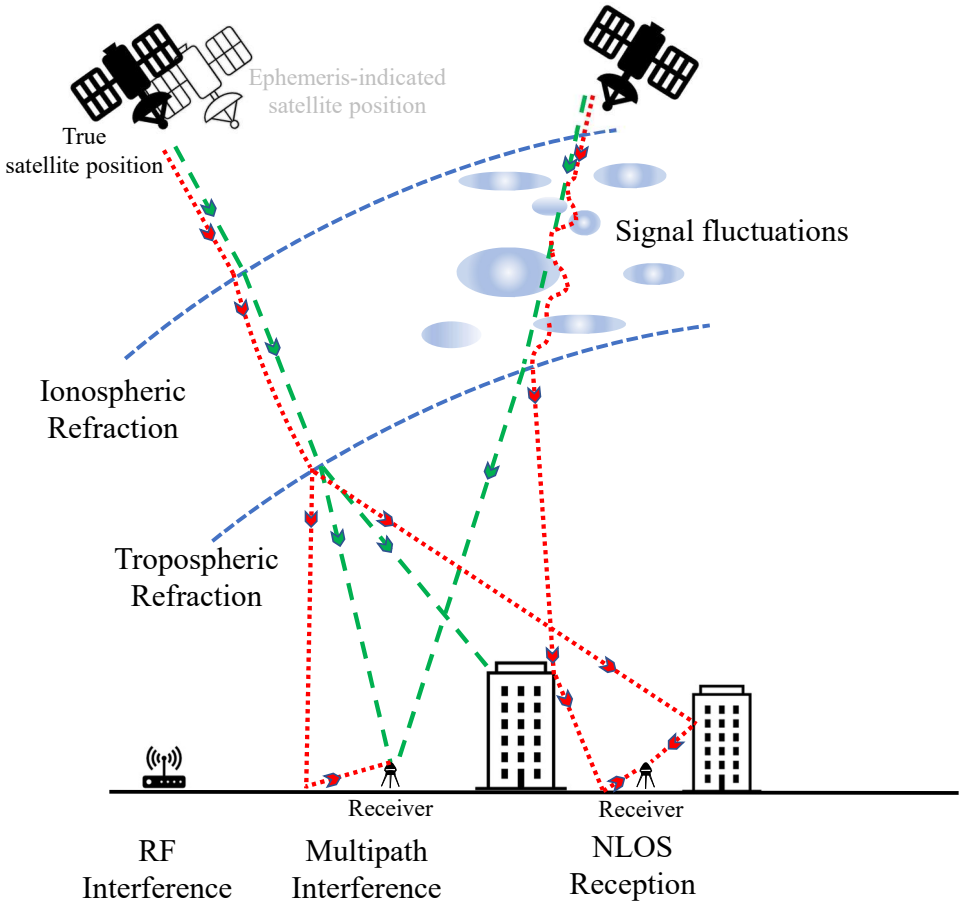

Figure 2.15: Principal GNSS error sources.

addition of UERE components forms the total system UERE that is assumed to be Gaussian distributed [3].

When the GNSS signals travel through the atmosphere, the signals suffer from delays and atmospheric anomalies caused by different layers of the atmosphere. While the ionosphere is a dispersive medium located in the atmosphere between 70 km and 1000 km above the Earth, the troposphere is the lowest layer closest to the Earth surface and it is a non-dispersive medium for radio waves below 15 GHz [3].

The ionospheric delay is proportional to the electron density along the path length [52]. It is referred to as Total Electron Content (TEC) and it is a function of the day, user location, satellite elevation angle, weather season, magnetic activity, ionizing flux, solar activity, and scintillation [26]. Scintillation is caused by the electron density irregularities in the ionospheric plasma as drawn in Figure 2.15. Hence, this varying nature of the atmosphere makes the prediction of the ionospheric delay very difficult. For a user having a single-frequency receiver, the dominant pseudorange error is the ionospheric delay as it is seen in Table 2.3. Since

Table 2.3: Typical GNSS User Equivalent Range Error (UERE) Budget for Single-Frequency Receiver [18]

Segment Source	**Error Source**	$1\,\sigma$ **Error (m)**
Space/Control	Broadcast clock	0.4
	Differential group delay	0.15
	Broadcast ephemeris	0.3
User	Residual ionospheric delay	7.0
	Tropospheric delay	0.2
	Receiver noise and resolution	0.1
	Multipath	0.2
System UERE	Total (RSS)	7.03

the effect is dispersive, it also depends on the frequency of the signal that travels through the ionosphere. Therefore, having a dual-frequency receiver (e.g. GPS L1 and L2) enables the estimation of the delay on both frequencies by differencing the pseudorange measurements made on two frequencies [26]. In this approach, multipath error and receiver noise errors are neglected.

The speed of the signals also alters within the troposphere and the delay is a function of the local temperature, pressure, and relative humidity. Although its effect is nearly independent of the signal frequency, it depends on the time of passage [52]. Therefore, a mapping function model is also needed to determine the path length considering satellite location (i.e. elevation angle) and the user height.

Measurement errors in the receiver are induced by the signal tracking loops and the dominant error sources are thermal noise jitter and interference effects [26]. Multipath effect is basically the self-interference of the replicas of the signals that are reflected or refracted from the physical surrounding environment and it varies significantly depending on the surrounding environment of the receiver and satellite elevation angle. Both multipath and receiver noise errors are uncorrelated between receivers and they can change very rapidly [26].

Furthermore, it has to be mentioned that there are some ways for compensating and mitigating the errors up to a point. For example, in order to compensate for satellite clock and satellite orbit errors, it is possible to download precise satellite clock and ephemeris information from a Space Based Augmentation System (SBAS) or a Precise Point Positioning (PPP) service provider [53]. Due to the fact that the ionospheric and tropospheric conditions are very similar within a local area, besides the models that are used to estimate the amount of error caused by the delays, Differential GNSS or Real-Time Kinematic (RTK) receiver configurations are exploited. Moreover, high-end GNSS receivers and antennas today tend to have less receiver noise and be better at rejecting multipath than lower cost GNSS

receivers [53]. Nevertheless, the modernization of the GNSS systems, availability of multi-frequency signals with augmentation systems, and the developments in GNSS receiver and antenna technologies leave the multipath and scintillation effects as the dominant error contributions in the positioning.

A more detailed description of each source can be found in [18, 26, 28, 54].

Chapter 3

Ionospheric scintillation and multipath

This chapter starts with the description of the ionospheric scintillation, estimation of the scintillation indices that quantify and characterize the scintillation events, and analysis of real scintillation events. With the literature research on scintillation modeling and classical scintillation detection methods, an overview of scintillation effects on the signal processing stages of a receiver are provided. Then, the multipath effect on GNSS measurements and observables is investigated through the analysis of real and simulated GNSS data. Moreover, classical multipath detection techniques in the literature are examined.

3.1 Ionospheric scintillation

Trans-ionospheric communication of the radio waves while traveling from transmitter to user is affected by the ionosphere that is highly variable and dynamic in both time and space [4]. The ionosphere, highly varied propagation medium, has an irregular structure due to plasma instabilities and scintillation is basically random fluctuations of the parameters of trans-ionospheric waves. Observation of the scintillation has been used in many research fields such as astronomy, geophysics, atmospheric physics, ocean acoustics, telecommunications, etc. so as to identify the irregular structure of the propagation medium [4].

GNSS signals undergo severe propagation effects such as phase shifts, group delays, and amplitude variations while propagating through the ionosphere [47]. Ionospheric irregularities affect the GNSS signals in two ways, namely, refraction and diffraction, and both of them are caused by the group delay and phase advance of GNSS signals [55]. Both the aforementioned effects that are usually denoted as *scintillation* as the event causing fluctuations in the signal amplitude and phase of the received signals. Large-scale variations in both signal power and phase with the

increased measurement noise level severely degrade the GNSS receiver performance by preventing the receiver from correctly acquiring the GNSS signals or causing loss-of-lock when the signals are tracked.

Under a scintillation event, proper countermeasures could be undertaken at signal processing level, enabling either more robust signal acquisition and tracking or alternate resources to decrease the effect of disturbed signal propagations. Therefore, detecting and monitoring the scintillation effects in order to estimate the ionospheric scintillation in its early stages and measure the scintillation parameters gains importance. In this sense, GNSS signals provide an excellent means for measuring scintillation effects due to the fact that they are available all the time and can be acquired through many points of the ionosphere simultaneously [56]. With the coming new GNSS systems, a greater number of signals are available for monitoring signals and the advantages of new modernized signals and constellations for scintillation monitoring can be found in [40]. Although GNSS signals are themselves affected by the ionospheric scintillation too, observation of the received GNSS signals can be a possible option to estimate the ionospheric scintillation [56].

The received signal $r(t)$, where detailed in Section 2.3.1 and that is a linear combination of signals $s(t)$ broadcast by N visible satellites, can be expressed under scintillation as:

$$r(t) = \sum_{i=1}^{N} \xi_{s,i}(t)\, s_i(t) + \omega(t) \tag{3.1}$$

where $\omega(t)$ is zero-mean noise that is usually modeled as white Gaussian and $\xi_s(t)$ is the ionospheric scintillation disturbance effect [57]:

$$\xi_s(t) = \rho_s(t)\, \exp(j\theta_s(t)) \tag{3.2}$$

where $\rho_s(t)$ and $\theta_s(t)$ are envelope and phase components, respectively. However, this kind of model could mimic the variations of other effects besides scintillation, and it must also be specific among the scintillation events. Thus, modeling and characterizing the ionospheric scintillation are not easy and straightforward as discussed in Section 3.2.1, and for example, as it is observed in the Cornell model, $\xi_s(t)$ aims to represent the perturbations of specifically equatorial scintillation activity on the signal amplitude and phase. Correspondingly, there are two parameters (i.e. scintillation indices) that are typically used to indicate the amount of scintillation effect in a satellite signal and that are computed by employing the tracking outputs [56]: *amplitude scintillation index* S_4 and *phase scintillation index* σ_ϕ.

While S_4 is unitless, σ_ϕ is measured in radians. Even if they have different dimensions, both S_4 and σ_ϕ indices typically fall within the range of 1 and 0. Throughout the analyses and implementations in this thesis, different levels of scintillations are evaluated, and the values proposed for classifications are in line with the ones in other papers [58, 59] that base the choice of the thresholds on statistical observations. When there is no scintillation, the indices are below 0.2.

For weak scintillation, the indices are normally between 0.2 and 0.5. It is often considered as moderate scintillation when the indices are between 0.5 and 0.7. If the indices are higher than 0.7, they are evaluated as strong scintillation events.

In the following, estimation of the scintillation indices by employing different techniques that consist of detrending operations and the analysis and statistics of the scintillation events through the collected data are provided. The necessity of detrending the phase and/or amplitude measurements arises from the need to consider the related-frequency portion of the fluctuations due to diffraction. Indeed, the signals scattered from the surrounding environment could mimic the disturbance effect of ionospheric scintillation [60], which points out the significance of post-correlation data processing in the tracking stage to quantify, detect and monitor a scintillation event.

3.1.1 Estimation of scintillation indices

Phase detrending

Phase scintillation monitoring is achieved by computing the σ_ϕ index that corresponds to the standard deviation of the detrended phase measurements [61]:

$$\sigma_\phi = \sqrt{\langle \varphi^2 \rangle_T - \langle \varphi \rangle_T^2} \tag{3.3}$$

where φ is the detrended phase measurement that can be obtained by processing the carrier phase measurements through the filters. Accumulated Delta Range (ADR) that corresponds to the accumulation of the estimated phase by the corresponding carrier tracking loop is used for the carrier phase observation. $\langle \cdot \rangle_T$ is the average operation over a fixed period T which generally denotes a 1-min average [61].

There are two phase-detrending methods that are mostly used, and they will be described in this Section. Generally speaking, the phase measurements are passed through cascaded high pass filters and all low-frequency effects are removed. Raw data (φ) at 50 Hz rate from tracking outputs are used and the indices are generally computed at an observation interval of $T = 60$ s, as previously remarked.

i) Cascaded High Pass Filters: In this phase detrending algorithm, the phase measurements are passed through three cascaded 2^{nd} order High Pass Filters (HPFs), and all low-frequency effects are removed [56]. The block diagram is as shown in Figure 3.1.

Each stage filter has a transfer function in the s-plane [56]:

$$H_i(s) = \frac{s^2}{s^2 + \alpha_i \omega_N s + \omega_N^2} \tag{3.4}$$

where $f_N = \omega_N/(2\pi)$ is the filter's corner frequency in Hz. α_1, α_2, and α_3 are the coefficients, the product $H_1(s)H_2(s)H_3(s)$ makes up the frequency response of the

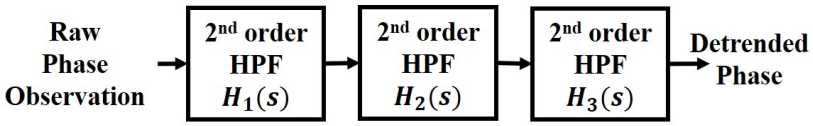

Figure 3.1: Cascaded High Pass Filter (HPF) design for phase detrending.

high-pass filter. Although the characteristics of the ionospheric effect at different regions require different detrending settings, generally $f_N = 0.1$ Hz is selected in the implementations. More information related to the selection of the coefficients and cutoff frequency can be found in [56]. Moreover, in setting the filter cutoff frequency and coefficients, the oscillator (e.g. TCXO, OCXO) phase noise, thermal noise, and the multipath effects on lower frequency components should be considered to monitor scintillation events better; hence, as it is expected, empirically derived values are reported in the literature.

ii) Butterworth Filters: Another popular detrending method is described in [62]. It is based on the use of a Butterworth filter that can be implemented by cascading six 1^{st} order high-pass Butterworth filters, each with a cutoff frequency $f_c^{'}$ as depicted in Figure 3.2.

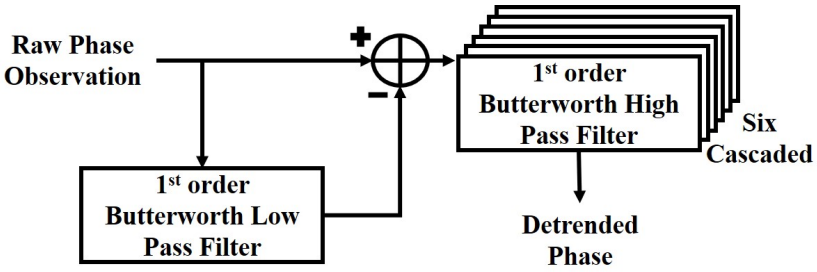

Figure 3.2: Block diagram of Butterworth filtering for carrier phase data.

The equivalent cutoff frequency of each filter is computed by [63]:

$$f_c = \frac{f_c^{'}}{\sqrt{2^{1/N} - 1}} \tag{3.5}$$

where N is set to 6 in our case and by setting $f_c = 0.1$ Hz, it is obtained that $f_c^{'} = 0.035$ Hz.

The selection of 0.1 Hz is proposed in [56] and the motivation behind cascading a number of lower-order high-pass Butterworth filters instead of employing one higher-order filter is to overcome the problem of phase shift between input and output [62, 63].

Amplitude detrending

S_4 index that is used to quantify the amplitude scintillation is derived from the detrended intensity of the signals. S_4 values are also computed over $T = 60$ s intervals by processing the prompt in-phase (I_i) and quadraphase (Q_i) correlator outputs at 50 Hz rate. For example, in the case of employing 1 ms integration time in the tracking of GPS L1 C/A signal, in other words, having I_i and Q_i samples with 1 kHz rate, the Narrow Band Power (NBP) and Wide Band Power (WBP) are computed as [56]:

$$\begin{aligned} \text{WBP} &= \sum_{i=1}^{20} I_i^2 + Q_i^2 \\ \text{NBP} &= \left(\sum_{i=1}^{20} I_i \right)^2 + \left(\sum_{i=1}^{20} Q_i \right)^2 \end{aligned} \tag{3.6}$$

where the raw signal intensity is equal to (NBP − WBP) and it is measured every 20 milliseconds. In the case of measurements performed over data channels, a summation over a bit transition has to be avoided. The value of 20 ms is a heritage of GPS signals processing wherein the L1 C/A code data rate is 50 Hz.

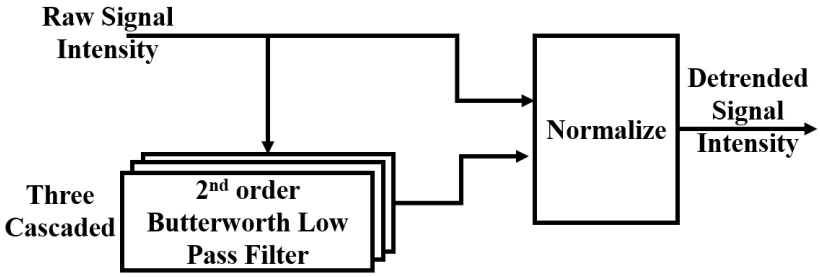

Figure 3.3: Block diagram of Butterworth low pass filtering for intensity measurements.

The transfer function of each filter depicted in Figure 3.3 has the form in the s-plane [56]

$$H_i(s) = \frac{\omega_N^2}{s^2 + \alpha_i \omega_N s + \omega_N^2} \tag{3.7}$$

where $f_N = \omega_N/(2\pi)$ is the filter's corner frequency in Hz and it is not necessarily the same as for phase detrending. The detrending signal intensity SI is computed by diving the raw signal intensity by the output of the low-pass filter stage [56]:

$$SI_k = \frac{(\text{NBP} - \text{WBP})_k}{(\text{NBP} - \text{WBP})_{LPF,k}} \tag{3.8}$$

where k is the measurement index that corresponds to a 20 ms processing interval. Then, the S_4 metric is calculated as [64]

$$S_4 = \sqrt{\frac{\langle SI^2 \rangle_T - \langle SI \rangle_T^2}{\langle SI \rangle_T^2}} \tag{3.9}$$

where SI is the detrended signal intensity, $\langle \cdot \rangle_T$ is the average operation over a fixed period T. So as to compute the scintillation effect on the signal amplitude and to remove the variations due to other effects (e.g. thermal noise, tropospheric delay, multipath, receiver clock, etc.), detrending operations that commonly correspond to processing the signal intensity through cascaded low-pass filters are employed. However, in some cases where the fluctuations and noise that mixed into the signal are not at the level to contaminate the actual scintillation data, the S_4 can be approximated without detrending the signal intensity.

3.1.2 Data collection and sites

The amount of amplitude and phase scintillation that affect the GNSS signal can be monitored and measured by exploiting the signal tracking stage correlator outputs in the GNSS receiver. Specialized ISMRs or SDR based receivers can be used for monitoring purposes [47, 64, 65, 66, 67, 68].

Figure 3.4 shows an example of scintillation monitoring and data collection setup. A part of the data that are used throughout this thesis study were collected in an Antarctic station and in an Equatorial site by means of data grabbers of this kind. Data collection stations and coordinates are given in Table 3.1.

Table 3.1: Data Collection Sites

Station	**Coordinates**
South African Antarctic Research Base (SANAE-IV), Antarctic	Lat.: 71.67°S Long.: 2.84°W
Hanoi, Vietnam	Lat.: 21.00°N Long.:105.84°E
Centro de Radioastronomia e Astrofisica Mackenzie (CRAAM), Brazil	Lat.: 23.55°S Long.: 46.65°E

The data collecting setup is a custom-designed solution based on a multi-constellation and multi-frequency GNSS data grabber and a SDR receiver [65, 69]. The data collection process in Antarctica started in 2015 in the framework of the DemoGRAPE project and it is still on-going [69].

In such an installation, the data grabber used is Fourtune, which is a multi-band multi-frequency data collection unit and it is able to perform medium-complexity

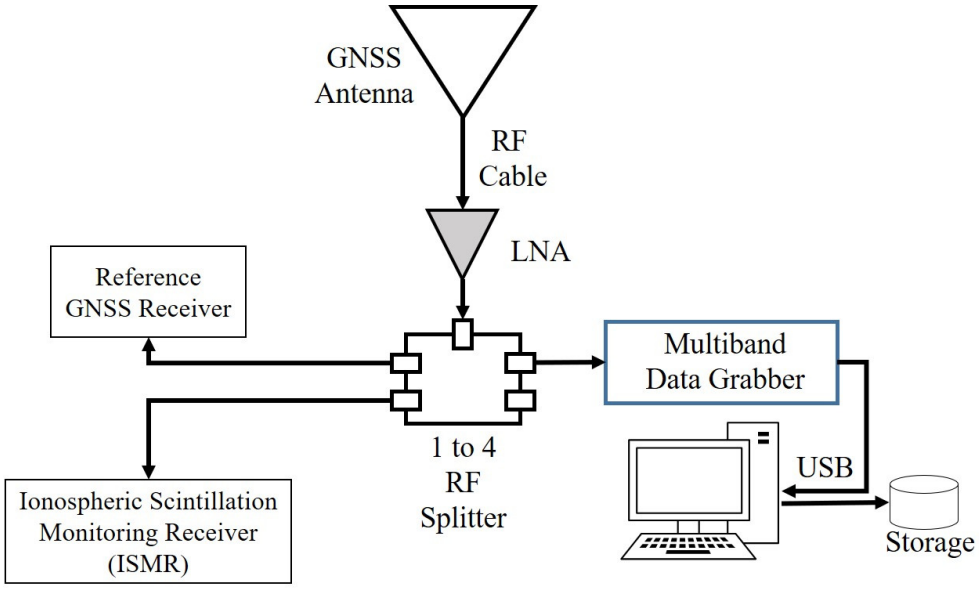

Figure 3.4: GNSS experimental scintillation data collection configuration.

signal processing (e.g. decimation, digital filtering, quantization, etc.). It has been developed by the researchers at Joint Research Center (JRC) of the European Commission in Italy and an interested user can find more information about its architecture in [64].

GNSS signals have been captured by an active antenna embedding a built-in amplifier with 39 ± 2 dB gain and maximum 2.8 dB noise figure. The LNA of the front-end has 30 dB gain and 3 dB noise figure. However, depending on the test setup, due to the antenna cable, coaxial connectors and one-to-four splitter, additional losses are experienced. An interested reader can find useful material about the design of monitoring stations of this kind in [47]. The data grabber operates by means of monitoring of regular intervals of S_4 and σ_ϕ, and in case their level passes a threshold, it triggers the data storage.

The collected IF data through the data grabber are post-processed in the proprietary non-real-time fully software GNSS receiver that has been developed within the thesis work and of which the implementation details are shared in Appendix A. All the signal and data processing techniques (e.g. signal acquisition, tracking, scintillation analysis, navigation data processing, etc.) have been implemented in MATLAB with a modular architecture.

3.1.3 Analysis of real scintillation data

In order to provide a computation example and discuss also the benefits and limitations of scintillation detection based on S_4 and σ_ϕ, in this Section some examples of real data processing are provided. The ionospheric scintillation indices

are computed by the software receiver through post-processing of the collected IF data.

Figure 3.5 (a) and (b) show an example of the computed amplitude and phase scintillation indices of GPS L1 signal that belongs to the data collected at SANAE IV on January 21, 2016. In Figure 3.5 (b), a sharp increase starting around 12:50 a.m. can be noticed which indicates that the GPS signal broadcast from PRN-14 satellite experiences strong phase scintillation. On the other hand, in Figure 3.5 (a), there is no increase observed in the computed S_4 indices which could be an indicator for amplitude scintillation.

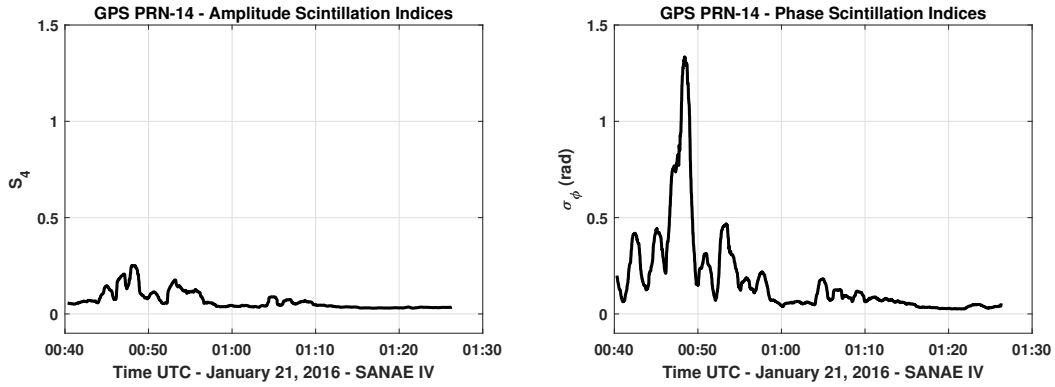

(a) Amplitude Scintillation. (b) Phase Scintillation.

Figure 3.5: Scintillation index values of GPS L1 C/A PRN-14 signal - January 21, 2016 (SANAE IV).

Figure 3.6 (a) and (b) show an example of the computed amplitude and phase scintillation indices of GPS L1 signal that is broadcast from PRN-20 satellite. It is seen that both amplitude and phase scintillations occur at the same time in these data that were collected in Hanoi on April 16, 2013.

Owing to the fact that the occurrence of the ionospheric scintillation depends on the several factors such as solar and geomagnetic activity, geographic location, the season of the year, and local time [65], it is not straightforward to model the occurrence of the event, and statistical analyses have been exploited in order to characterize the intensity, duration and occurrence frequency of the scintillation events observed in different locations [70, 71]. Due to polar location of SANAE IV, phase scintillation statistically occurs more often than amplitude scintillation [70]. In the scintillation events observed at the equatorial region, typically both phase and amplitude scintillations occur with faster and deeper signal power fadings that take longer durations [71]. Furthermore, in [71], the authors provided a statistical analysis of intensity, duration and occurrence frequency of amplitude and phase scintillation by analyzing the collected data-sets in both high latitude and equatorial regions. The analysis shows also that while the mean duration of amplitude

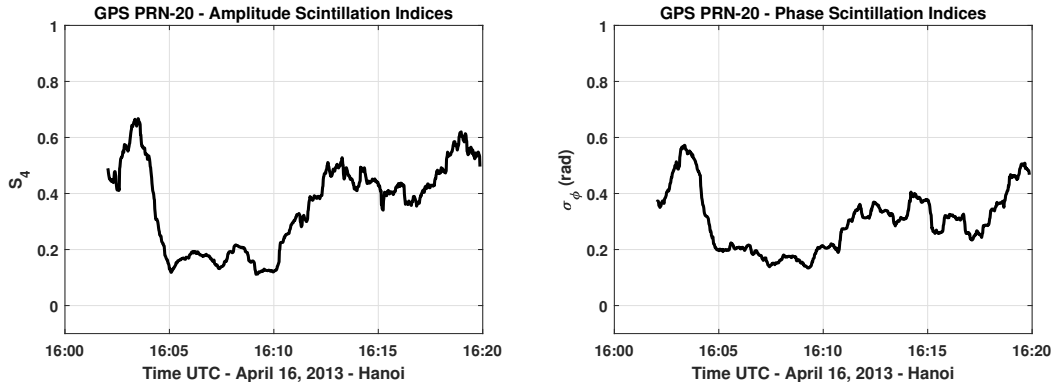

(a) Amplitude Scintillation. (b) Phase Scintillation.

Figure 3.6: Scintillation index values of GPS L1 C/A PRN-20 signal - April 16, 2013 (Hanoi).

scintillation events observed in the equatorial region lasts 12.4 minutes, the mean duration of the phase scintillation events in the polar region is 5.6 minutes. An interested reader can find more statistics related to scintillation events in [71, 70].

3.2 Scintillation effect

Although scintillation phenomena are well known and widely characterized, it is difficult to find a definitive treatment of the theory of scintillation [9], and it is a fact of life for a number of communication and radar systems that have to operate through the auroral or equatorial ionosphere [5]. Moreover, it has been found that the atmospheric structure has the basic characteristics of fluid turbulence in the equilibrium range, which is characterized by the well-known properties of Kolmogorov turbulence [9]. It has led to the development of the theoretical characterization of the scintillation effect [72, 73] besides the observational point of view of the scintillation effect. Moreover with the scintillation observations to identify and diagnose the irregular structure, different scintillation models including the modeling of the wave propagation through the ionospheric irregularities have been developed.

It is quite important to understand the global form of ionospheric scintillation and to be able to model it. Because it helps users to differentiate the observed fluctuations whether are originated from the ionospheric irregularities or from the equipment or human-made so that countermeasures could be developed having identified the effects [4].

3.2.1 Signal characterization and simulation models

Ionospheric scintillation models in the literature can be divided into three groups, namely, analytical models, climatological models based on in situ data, and global climatological models [4, 74].

The most known **analytical models** such as the ones developed by Fremouw and Rino [75] and Aarons [76] are suitable for trans-ionospheric Very High Frequency (VHF) and Ultra High Frequency (UHF) communication links. Although in the model of Franke and Lui [77], multi-frequency scintillations observed in C-band and L-band besides VHF band are used for modeling through analytical and numerical techniques, the study is limited to the amplitude scintillation data observed in the equatorial region [74]. Likewise, the three-dimensional ionospheric plume model developed by Retterer [78], and the empirical model that exploits the cubic spline technique to reproduce the variation of scintillations developed by Iyer et al [79] suffer from being limited to either a geographical sector (e.g. low latitude) or the VHF band frequencies.

The first attempt for a **climatological model based on in situ data** is by Basu et al in 1976 [80]. A developed model of equatorial scintillations with a study of F-region irregularities using the density measurements obtained from the Retarding Potential Analyzer (RPA) data onboard the OGO-6 satellite located at altitude of 400 km is presented in [80]. Moreover, in 1981, by using the Atmospheric Explorer D (AE-D) data, the model of scintillations at high latitudes was developed [4]. Another most-known model based on in situ data is the Wernik-Alfonsi-Materassi (WAM) model [81]. It is a scintillation climatological model for the Northern Hemisphere high-latitude ionosphere and it uses the Dynamics Explorer 2 plasma density data collected between August 1981 and February 1983, the International Reference Ionosphere (IRI) model [82] for estimating the irregularity layer thickness, and the phase screen approach of Rino [83]. However, the aforementioned models based on in situ data are limited in space and time by the data used in their constructions and hence, their outputs cannot be used for real-time GNSS applications [74].

The most known and used **global climatological models** are WideBand MODel (WBMOD) and Global Ionospheric Scintillation Model (GISM) [4, 74]. Moreover, these models have been preferred to be used to estimate the scintillation effects on GNSS receivers.

- *WBMOD* was developed over 40 years ago by NorthWest Research Associates (NWRA) scientists to study ionospheric scintillation. On their webpage, NWRA still provides an access to the solar and geomagnetic activity indices that are frequently used as inputs to space-weather models [84]. The WBMOD is a global model and it includes the variations with solar cycle, season, geomagnetic disturbance levels, and local time [85]. The model is formed by two parts: the modeling of the electron-density irregularities in

the F-region, which is the highest region of the ionosphere and located at altitudes greater than 160 km, and a wave propagation law that is the power-law phase screen model [83] developed by Rino in 1979 [85]. The phase spectrum $P_\phi(f)$ is characterized by the power law with two parameters, namely, the spectral index (p) and the strength of the phase spectrum at a fluctuation frequency of 1 Hz (T) [86]:

$$\begin{aligned} p &\approx q + 1 \\ T &= N(q)\lambda^2(C_s L)\ \sec\theta\, G V_e^q \end{aligned} \tag{3.10}$$

where N is a normalization factor. q is one dimensional spectral index of electron density fluctuations as measured in situ onboard a satellite. λ is the radio wavelength and $C_s L$ is the strength of the irregularities where C_s is the turbulence strength parameter and L is the irregularity layer thickness [83]. θ is the zenith angle. $G(a, b, \delta)$ is a phase enhancement factor due to geometry with three-dimensional anisotropic irregularities with respect to the magnetic field, which a is along the field, b is across the field, and δ is an orientation angle in relation to the local magnetic shell. $V_e(V_s, V_d, a, b, \delta)$ is the effective scan speed across contours of plasma density [86]. V_s is the line-of-sight scan velocity and V_d is the plasma irregularity drift velocity.

Then, by taking the integral of the phase spectrum $P_\phi(f)$ over a processing interval, phase variance is given by [4, 86]

$$\sigma_\phi^2 = \int_{f_c}^{\infty} P_\phi(f) df = 2\int_{f_c}^{\infty} \frac{T df}{(f_0^2/f^2)^{p/2}} \tag{3.11}$$

where f_c is low frequency cut off, $f_0 = V_e/2\pi r_0$ where r_0 is the outer scale of ionospheric structure. For weak intensity scintillation, in the absence of multiple scatter, the corresponding weak-scatter scintillation index $S_{4\mathrm{w}}$ is [86]:

$$\begin{aligned} S_{4\mathrm{w}}^2 &= \frac{M(q)}{N(q)} T \frac{F}{G} \frac{Z^{q/2}}{V_e^q} \\ S_4^2 &\approx 1 - \exp(-S_{4\mathrm{w}}^2) \end{aligned} \tag{3.12}$$

where $F(q, a, b, \delta)$ is the Fresnel filter factor and $Z(\lambda, h)$ is the Fresnel zone size. $M(q)$ is the normalization factor. The varied range of irregularities with respect to the plasma drift velocity impose perturbations on the signals and the threshold separating small and large scale irregularities is given by Fresnel's scale [16]. While the irregularities having scale sizes below Fresnel's scale, both refractive and diffractive effects occur at the same time which results in an interference pattern at a ground receiver [87], the irregularities having scale sizes above Fresnel's scale result in a refractive effect.

- *GISM* was developed by Bèniguel and Buonomo in 1999 [88] with the inclusion of the Multiple Phase Screen (MPS) technique that consists the Parabolic Equation (PE) method for a medium divided into successive layers of which each acts a phase screen. In the extended version of the model provided by Bèniguel in 2002 [89], the inputs of the model are listed as the geophysical parameters (e.g. flux number, drift velocity), the inhomogeneity data, and the operating data (e.g. carrier frequency etc.). In homogeneity characteristics, the spectral density of the electron density fluctuations, correlation distance of the inhomogeneities, height of the irregularities, and drift velocity and direction of the inhomogeneities are to be specified [89]. Besides the MPS technique, the GISM also includes the NeQuick model as an ionospheric electron density model. NeQuick model is particularly for the study of trans-ionospheric propagation applications and was developed by ICTP Trieste and the University of Graz and the model genesis, uses, and evolution can be found in [90]. Furthermore, the details of GISM can be found in the published user manual [91]. It has to be noted that the GISM outputs the intensity and phase scintillation indices and also provides the time series synthesis of transmitted signal phase and intensity [89].

Since both WBMOD and GISM have a climatological nature, they do not properly represent the actual conditions but rather show an average dependence of the propagation characteristics on geophysical conditions [74]. Furthermore, these models are being calibrated with the data sets that do not include the GNSS derived data; hence, it causes a limitation in the case of GNSS applications on which the geometry is always changing and is different from geostationary and polar-orbiting satellite links [92]. A comparison of GISM and WBMOD with experimental data for satellite navigation applications is provided in [92].

Moreover, with a need for a simple scintillation model relevant to GNSS user equipment, scientists at Cornell University developed the Cornell Scintillation Model (CSM) to test and evaluate the performance of GNSS receivers under scintillation [55, 93]. In the model, scintillation amplitude is assumed to follow a Rice distribution:

$$K = \frac{\sqrt{m^2 - m}}{m - \sqrt{m^2 - m}} = \frac{\sqrt{1 - S_4^2}}{1 - \sqrt{1 - S_4^2}}, \quad S_4 \leq 1 \tag{3.13}$$

where $K \leq 0$ is the Rician parameter and Nakagami-m distribution is defined for $m \leq 1/2$. Another important assumption of the model is that the rapidly-varying component of the complex scintillation has a spectrum similar to the white noise passing through a low-pass second-order Butterworth filter. Block diagram of the scintillation model is depicted in Figure 3.7. There are two input parameters to define the severity of the scintillation: S_4 and τ_0.

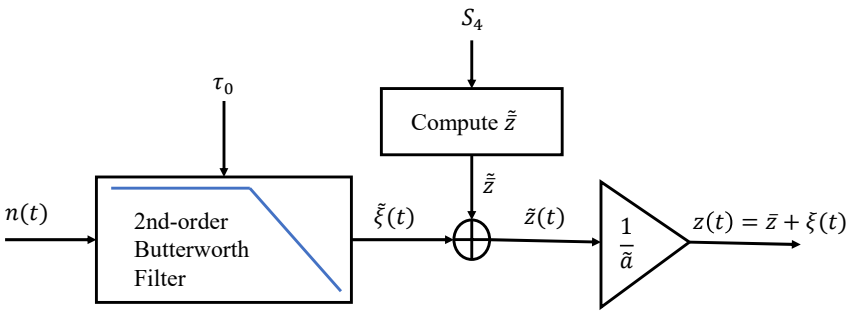

Figure 3.7: Block diagram of the Cornell Scintillation Model (CSM) (adapted from [93].)

In the output of the model $z(t) = \bar{z} + \xi(t)$, $\bar{z}$ is the direct component and $\xi(t)$ is the time-varying multipath component (i.e. refers to the fading process). $\tau_0 > 0$ is the channel decorrelation time at which the autocorrelation of $\xi(t)$ reduces to $1/e^{th}$ of its initial value. Having a narrow autocorrelation function or in other words, having a small τ_0 implies a scintillation that changes rapidly with time [93]. When there is no scintillation $z(t) = 1$. The details of the model can be found in [55, 93, 94].

It has to be noted the CSM is not a global scintillation model and it is based on equatorial scintillation effects. Furthermore, it is a statistical model that generates perturbations on the signal amplitude and phase; hence, the statistics may disagree with the localized irregularity patches that are associated with the ionospheric scintillation [95, 96].

Moreover, a comparative summary of some ionospheric models with a detailed literature review can be found in [4].

3.2.2 Scintillation effect at the signal processing stages

During a scintillation event, the availability, reliability, and accuracy of GNSSs can be affected. In order to mitigate the effect of the rapid fluctuations in the amplitude and phase of the signal, one of the solutions could be to minimize the effects of the scintillation by making the signal acquisition and tracking stages that are two key stages of the receiver more robust. In the literature, the aforementioned simulation models have been practically used in the analysis of the scintillation effects on GNSS receivers and the development of robust architectures.

It can be pointed out that most of the studies in the literature do not consider the effects of scintillation on the acquisition stages. It has been assumed that the rate of phase changes that occurred during the phase scintillation events stays quite constant over the integration time or this effect is minimal in the acquisition process. However, while the phase scintillation might have has less impact on the acquisition stage, strong amplitude scintillation can prevent the acquisition of the

signal. Detailed comparative performance analysis of different acquisition methods and their robustness to the presence of phase and amplitude scintillation in the propagation environment are presented in Section 4.1.

Nonetheless, as far as the tracking stage is concerned, when an amplitude scintillation occurs, the amplitude of the correlator outputs is reduced and it causes a lower signal carrier-to-noise density power ratio (C/N_0) hindering a receiver's ability to track the signal. On the contrary, phase scintillation not only introduces extra noise to the estimation of the carrier phase error but also causes deep fadings because of the destructive interference resulting in the loss of lock of the signal. In order to be able to cope with the fading and abrupt phase changes of the scintillation effects, some additional robust architectures and various tracking schemes (e.g. FLL-assisted-PLL, KF-based carrier tracking, etc.) have been investigated in the literature. In such techniques, additional degrees of freedom are provided by applying different choices for the integration time and loop parameters (orders, bandwidths, etc.) and by employing different state space design models by considering the presence of thermal noise, oscillator effects, receiver dynamics, and challenging environmental conditions. Examples of generalized GNSS signal carrier tracking loop architectures using traditional (FLL/PLL/DLL) and KF-based state space representations can be found in [97, 98, 99, 100].

For example, different methods have been proposed to tune the dynamic models by exploiting the knowledge about the scintillation level as in [101] or by using the C/N_0 levels as a control parameter to improve the tracking of the incoming signals as in [102, 103]. However, these types of adaptive algorithms require parallel computation of the scintillation level and to feed back such information to the tracking stage. Moreover, in [104], different constant-bandwidth PLL structures and KF-based tracking are compared under scintillation; unfortunately, the analysis is limited to an equatorial scintillation event in terms of loss-of-lock duration only.

Moreover, in order to show the performance of the proposed signal tracking techniques, different ionospheric scintillation models have been used. Some of the proposed algorithms are tested by using the CSM as in [93, 105], others the GISM [106, 107] or the WBMOD as in [108, 109]. It can be stressed that most of the aforementioned studies do not consider the effects of scintillation on GNSS signals under real scintillation events, but they limit the analysis to simulations. The performance of the carrier tracking methods, namely, traditional PLL and KF-based PLL, have been compared by using real GNSS signals affected by significant phase and amplitude scintillation effects in Section 4.2. The innovative aspect of the analysis resides in exploiting the real GNSS data instead of oversimplified or limited scintillation models.

3.2.3 Classical scintillation detection strategies

Detecting and monitoring the scintillation effects in order to estimate the ionospheric scintillation in its early stages, measure the scintillation parameters, and warn users about the potential degradation in the navigation gain importance. As classified in the recently published survey paper on scintillation detection, monitoring, and mitigation [57], in the literature, there are mainly four scintillation detection strategies, namely, visual inspection, thresholding, non-scintillation indices-based techniques, and machine learning approaches. Machine learning-based implementations are discussed in Section 5.2.1.

Although the **visual inspection approach** is time-consuming, not being automatic, open to user error, and lacking scientific rigor, it assures the best detection performance [57]. Besides the scintillation indices S_4 and σ_ϕ, other measurements (e.g. C/N_0, TEC, Rate of TEC (ROT), satellite azimuth and elevation, etc.) and other instruments such as solar flare detectors and magnetometers can be exploited to decide scintillation classification. Furthermore, since the multipath effect can inflate the scintillation indices and falsely indicate an ionospheric scintillation activity [110], a comparison with historical data can help to distinguish the unique pattern of scintillations and the similar trends on S_4 fluctuations, which are caused by the multipath effect depending on the daily satellite motion when the receiver position is fixed.

The **thresholding** method is a comparison of the scintillation indices including some additional masks to the predefined thresholds in order to characterize the scintillation phenomenon. In the case of that the scintillation indices (S_4, σ_ϕ) are directly compared to the thresholds $(T_{S_4}, T_{\sigma_\phi})$, it is referred to as hard detection rule [6]:

$$S_n[n] > T_{S_4} \text{ or } \sigma_\phi > T_{\sigma_\phi} \tag{3.14}$$

where the scintillation is claimed to be present if the indices exceed the thresholds. The performance of detection clearly depends on the choice of the threshold. Although this approach has simplicity, relatively low computational burden, and low tuning requirements, it is prone to have a large false alarm or missed detection rates because of other propagation errors (e.g. multipath, etc.) [57].

Furthermore, in the semi-hard detection approach, additional conditions on the satellite elevation angle (θ_{el}) and C/N_0 measurements can be applied to reduce the false alarm rates and better characterize the scintillation [6]:

$$(S_4[n] > T_{S_4}) \wedge (\theta_{el}[n] > T_{\theta_{el}}) \wedge (C/N_0[n] > T_{C/N_0}) \tag{3.15}$$

where $T_{\theta_{el}}$ is the elevation threshold that is to be decided considering the surrounding environment. However, T_{C/N_0} is mainly dependent on the receiver. For example, in [111], an amplitude scintillation event trigger based on S_4 and C/N_0 measurements is proposed:

$$S_4 > 1.075 - C/N_0 \cdot 0.01875 \tag{3.16}$$

where C/N_0 is in dB-Hz. This threshold is based on the collected data in Alaska through a commercial GNSS receiver. However, in [112], elevation angle is considered a better variable for the threshold setting in some cases:

$$\begin{aligned} S_4 &> -9.09 \cdot 10^{-4}\theta_{el} + 0.1373, \\ \sigma_\phi &> -6.36 \cdot 10^{-4}\theta_{el} + 0.1091 \text{ radians}. \end{aligned} \tag{3.17}$$

where θ_{el} is in degrees. The main disadvantage of the thresholding approaches is that they rely on the collected or analyzed data and they are not scaled for different spatial and temporal observations [57].

One of the **non-scintillation indices-based techniques** is based on wavelet-based detrending [113] and proposed alternative scintillation indices [61]. As it is discussed in Section 3.1.1, in the estimation of the scintillation indices, the detrending method and the selected cutoff frequency have an influence on the accuracy and validity of the computed indices. Through the wavelet transforms, preserving the local features of the signal by taking into consideration the non-stationarity of the raw signals unlike time-invariant Butterworth filters has been aimed [61]. Furthermore, in [114], rather than using the calculation of S_4 for the scintillation events that are not lasting $T = 60$ s [see Equation (3.9)] or more, inspecting the scalograms, which are wavelet statistical energy plots, from continuous wavelet analysis has been found useful.

In S_4 estimation, while the prompt correlator samples (3.6) are processed in traditional closed-loop tracking architectures, a statistical metric that is based on the histogram of the processed samples has been proposed in the assisted open-loop architectures that do not include either a PLL or an FLL [115, 116]. Although this approach is specific to the dedicated receiver architecture, it is insensitive to the degradation of the results under strong scintillations [57].

3.3 Multipath effect

Under multipath conditions, the received signal by the GNSS antenna consists of the direct LOS signal and the multipath signals. However NLOS contains only the reflected signals. In Figure 3.8, basic multipath and NLOS scenarios are demonstrated.

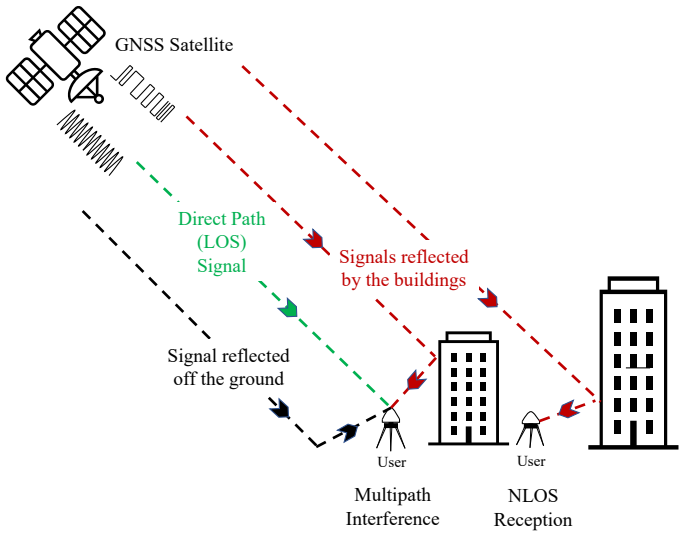

Figure 3.8: Multipath Interference and NLOS Reception.

3.3.1 Multipath effect on GNSS observables and measurements

The received signal by the GNSS receiver under multipath conditions can be modeled as [117]:

$$\begin{aligned} s(t) = & \underbrace{A\ p(t-\tau_0)\cos\left(2\pi f_0 t + \theta_0\right)}_{\text{Direct Signal (LOS)}} \\ & + A\sum_{k=1}^{N} \alpha_k\, p\left(t-\tau_0-\tau_k\right) \\ & \underbrace{\cos\left[\,2\pi f_0 t + \theta_0 + \Delta\phi_{M,k} + 2\pi\left(\Delta f_k - f_D\right) t\,\right]}_{N \text{ Multipath Signals}} \end{aligned} \tag{3.18}$$

where A, τ_0, θ_0, f_0, and f_D are the amplitude, propagation time, carrier phase, frequency, and Doppler shift of the direct signal, respectively. Ranging and data codes are represented by p. The direct LOS signal is superimposed by N multipath signals in which are attenuated by the coefficient α_k in the amplitude depending on the reflection and antenna gain pattern. τ_k is the time shift between the direct signal and the k^{th} multipath signal. $\Delta\phi_{M,k}$ is the multipath relative phase corresponds to the phase shift between the direct signal and the k^{th} multipath component. Multipath phase rate (i.e. fading frequency) is determined by the Doppler difference $(\Delta f_k - f_D)$ between the direct signal and the multipath component [117].

As it can be understood from (3.18), code and phase observations of the LOS signal are influenced by the multipath propagation. Measured code pseudorange

(ρ_j^k) and carrier phase (ϕ_j^k) measurements for the k-th satellite in the j-th band by a GNSS receiver can be written as [118]

$$\begin{aligned} \rho_j^k &= d_u^k + c\left[\delta t_u - \delta t^k\right] + I_j + T + M_j^\rho + \epsilon_j^\rho \\ \phi_j^k \lambda_j &= d_u^k + c\left[\delta t_u - \delta t^k\right] - I_j + T + N\lambda_j + M_j^\phi + \epsilon_j^\phi \end{aligned} \tag{3.19}$$

where d_u^k represents the true range between the satellite k and the user u. λ is the wavelength of the incoming carrier wave (e.g. $\lambda_1 = 0.19$ m for GPS L1 C/A signal). N is the integer ambiguity that refers to number of full carrier cycles between the satellite and receiver. c is the speed of the light. δt_u and δt^k are the receiver clock bias and satellite clock bias, respectively. I, T, M and ϵ denote the ionospheric delay, tropospheric delay, multipath error, and receiver noise. When the signal travels through the dispersive medium (ionosphere), the signal delay terms in code and carrier measurements are equal in magnitude but opposite in sign [27].

As it is denoted in (3.19), both observations can be affected by multipath. Moreover, although it is harder to mitigate the multipath in the carrier phase than in pseudorange, M_1^ρ is larger than M_1^ϕ [119]. For example, the analyses based on weighted multipath error envelopes model show that with some assumptions (e.g. the use of 0.1 chip narrow correlator in DLL, consideration of an urban environment, the use of multipath limiting antennas, etc.) mean multipath errors up to 4.9 m for the GPS L1 C/A signal having 42 dBHz C/N_0 are expected. However, maximum carrier multipath errors are around 21 mm for the aforementioned conditions. An interested reader can find the detailed comparative analysis in [117].

Moreover, the error characteristics of the multipath and NLOS reception is quite different. Whereas multipath affects code- and carrier-based measurements differently by producing different errors on different frequencies, in NLOS reception, the pseudorange measurement errors are dominated by the path delay, which is the difference between the reflected signal and the direct path, and indeed they are same for both code and carrier through different frequencies [7].

Multipath interference also affects C/N_0 measurements due to the fact that the measurements are based on the prompt correlator output of which size increases or decreases depending on the phase difference of the direct and reflected signals [7, 120]. The phenomenon is called constructive multipath interference if the phase of the direct and reflected signals differs less than $\pm 90°$. It results in an increase in the prompt correlator outputs and hence C/N_0 measurements. On the contrary, when the signals are out-of-phase (i.e. phase difference is around 180°), destructive multipath occurs resulting in a decrease in both prompt correlator outputs and C/N_0 measurements.

Furthermore, the strength of NLOS signals can be as nearly strong as the blocked direct signal or can be very weak, and even multipath interference and NLOS reception can occur together [7], which eventually lead to measurement and

position errors caused by the processing of the NLOS and multipath signals.

3.3.2 Analysis of simulated and real multipath data

Both real GNSS data and the simulated data in which the ionospheric, tropospheric, and multipath errors are modeled are analyzed from the point of multipath effect.

Simulated data

Table 3.2 shows the parameters of the simulated data. As a first step, by using the downloaded YUMA Almanac data [121], the orbital parameters of the satellites are obtained. By considering the pre-defined user position, the time and the almanac data, the positions of the visible satellites are computed. For each satellite, tropospheric, ionospheric, and thermal noise errors are added to the actual distance to model the pseudorange value (3.19). The ionospheric/tropospheric errors are modeled as in [28], where detailed information can be found. The error models are summarized in Table 3.2.

Table 3.2: GPS Constellation and Errors - Simulation Parameters

Parameters	**Values**
Signal Frequency	1575.42 MHz
User Position (Lat; Lon; Height)	45.0548° ; 07.6866° ; 250 m
Almanac Data	YUMA (Week 74) [121]
Tropospheric Delay	Modified Hopfield Algorithm [28]
Ionospheric Delay	Klobuchar Model [28]
Pseudorange Noise	Normal dist. with mean 0 and var. 1

Figure 3.9 shows the skyplot of the visible satellites and the positioning error computed in the East-North-Up (ENU) frame.

The multipath effect is generated exploiting an open source GPS multipath simulator developed in MATLAB [122] with the simulation parameters reported in Table 3.3.

Figure 3.10 shows the simulated multipath signatures generated through the multipath simulator [122] with respect to changing elevation angles. It can be noted that code and phase observations are affected in different ways depending on the elevation angles and the values can be used to consider different test scenarios. In the implementation of the proposed multipath detection algorithm that is detailed in Section 5.3, setting parameters have been decided through the simulated data analysis.

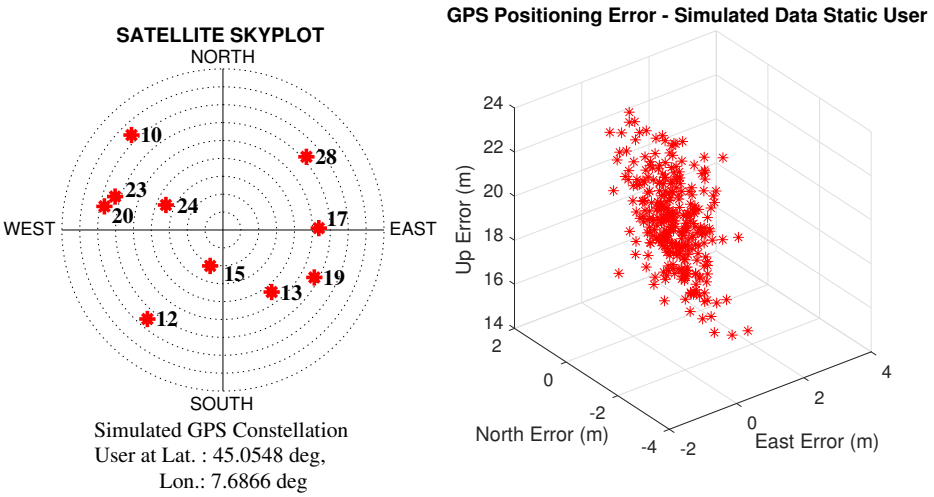

Figure 3.9: Simulated GPS Constellation and GPS Positioning Error.

Table 3.3: Multipath Simulation Parameters

	Parameters	Values
Signal	Type	GPS L1 C/A
	Frequency	1575.42 MHz
Medium Material	Top	Air
	Bottom	Soil (sandy loam with moisture content)
	Reflecting Surface Height Std.	0.1 meters
Antenna	Model	Trimble Choke Ring
	Height	2.0 meters
	Slope	Boresight/zenith are aligned
Receiver	Noise Temperature	290 K
	Noise Bandwidth	1 Hz
	Discriminator Type	Non-coherent early minus late power

Real data

Besides the simulated data, two different data sets that were collected on January 20 and 21, 2016 in the Antarctic station SANAE -IV are analyzed. Figure 3.11 (a) and (b) show the amplitude scintillation index values computed for the duration in which the data is analyzed. It has been observed that the increases or changes in the index values of some satellites repeat and follow almost the same

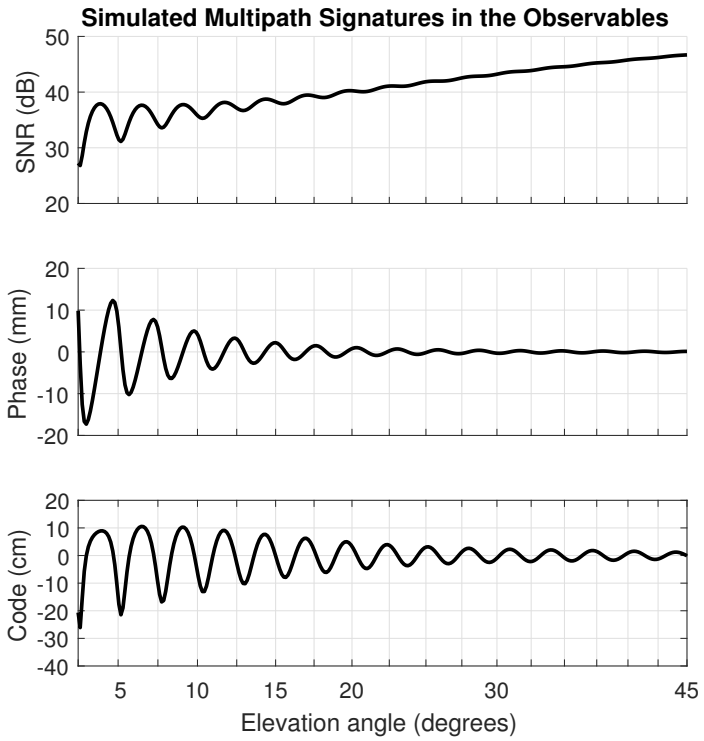

Figure 3.10: Simulated Multipath Effects in the Observables with Changing Elevation Angles.

trend on consecutive days. This is actually an artifact due to the presence of multipath errors that inflate the scintillation values and falsely indicate the ionospheric scintillation activity.

When the satellites that suffer from the multipath effect are included in the position computation, a degradation in the accuracy and the precision of the position solution is experienced. Figure 3.12 shows the computed positions with different satellite sets in Universal Transverse Mercator (UTM) coordinate system by processing the real data set collected on January 20, 2016. The differences between the mean positions of different clouds of points can be noticed.

3.3.3 Classical multipath detection strategies

The countermeasures are specific for each error source and as far as multipath is concerned, various methods have been employed in a GNSS receiver either at the signal processing level or at the measurement level in order to cope with its effect [123].

Among the methods detecting and estimating the multipath features at the signal processing level, it is worth mentioning the Multipath Estimating Delay

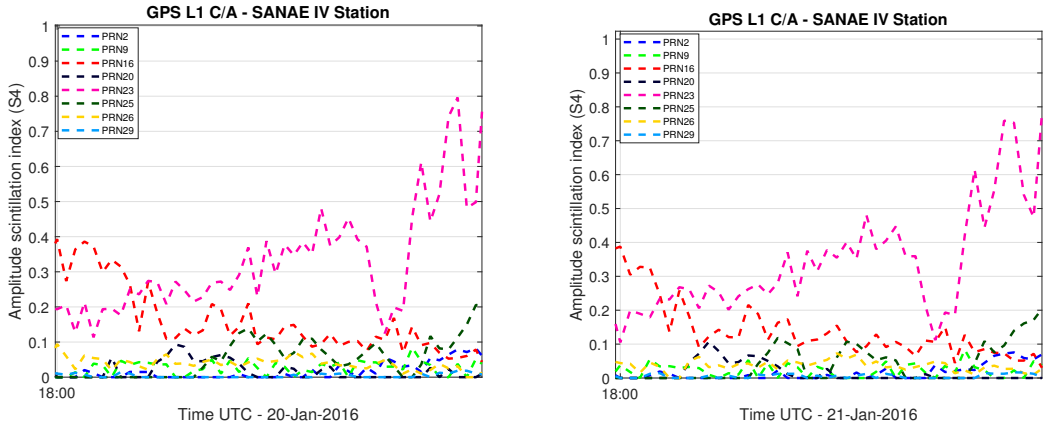

(a) GPS L1 C/A Signals - S4 Index Values - 20 Jan 2016.

(b) GPS L1 C/A Signals - S4 Index Values - 21 Jan 2016.

Figure 3.11: Amplitude scintillation index values at GPS L1 C/A signals - 20-21 Jan 2016 SANAE IV Station.

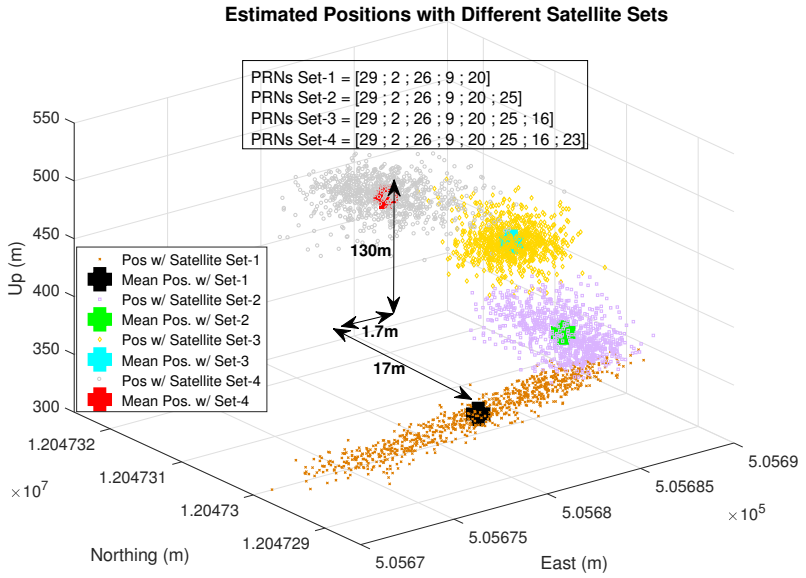

Figure 3.12: Real Multipath Effects in the Estimated Position.

Lock Loop (MEDLL) method [124] and its variants such as Multipath Mitigation Technology (MMT) [125] and Vision Correlator (VC) [126] techniques. Thanks to existing several correlators the signal parameters such as amplitude, delay, and phase of the LOS and multipath signals can be estimated as well as can be applied

for multipath detection purposes. For these methods, although an improvement in detecting and removing multipath signals is provided, a large number of correlators and higher sampling frequency are also needed which leads to a computational burden [127][117]. Moreover, since they are implemented at the signal processing level they are not flexible to modifications that might be required, not as may be able to act only at the measurement level.

There are indeed algorithms working at the measurement level and they are based on the consistency check of the produced measurements. The basic significant approach in the literature is the Receiver Autonomous Integrity Monitoring (RAIM) algorithm [128]. The RAIM methods such as the range comparison method, least-squares residual method, and parity method, are snapshot detection schemes with the assumption that noisy redundant range-type measurements are available at a given time epoch and in all cases, the problem is linearized about some nominal value of the position and clock bias [129]. The RAIM algorithm is mainly based on the calculation of the least square residuals to detect outliers by building a test statistic under the assumption of a Gaussian error [123][130] and it has the potential to detect multipath influences [117].

RAIM algorithm is contained in the receiver and autonomously provides a self-consistency check on the measurements. The RAIM algorithm, namely, the parity method, starts with the basic linearized GNSS measurement relationship that can be written as follows:

$$y = Hx + \epsilon \tag{3.20}$$

where y is $(n \times 1)$ vector of equivalent pseudorange measurements. n is equal to the number of the satellites in view. H is the Direction Cosine Matrix (DCM) between the user positions and the satellite positions in view, x is (4×1) vector of user's position with receiver clock bias and ϵ is $(n \times 1)$ vector of pseudorange measurement error. Least-square estimate of x is denoted as $\hat{x}$ and it is computed as:

$$\begin{bmatrix} \hat{x} \\ \dots \\ p \end{bmatrix} = \begin{bmatrix} \left(H^T H\right)^{-1} H^T \\ \dots \\ P \end{bmatrix} y \tag{3.21}$$

where p is the parity vector and P is defined as the parity transformation matrix of which size is $(n-4) \times n$. P is obtained by QR factorization of the H matrix.

$$H = QR = \begin{bmatrix} Q_1 & \vdots & Q_2 \end{bmatrix} \begin{bmatrix} R_1 \\ \dots \\ 0 \end{bmatrix} = Q_1 R_1 \tag{3.22}$$

where Q is the orthogonal matrix and R is the upper triangular matrix.

$$P = Q_2^T \tag{3.23}$$

The magnitude of the parity vector ($p = Py$) is used as the test statistics. For the real data, parity vectors are computed and Figure 3.13 shows the results of the magnitude change of the parity vector in time for different sets of satellites.

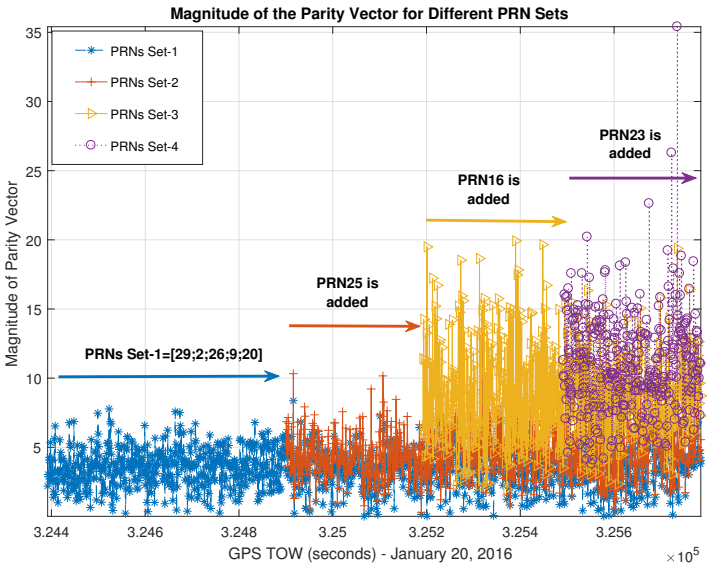

Figure 3.13: Magnitude of the RAIM Parity Vector in Time (Real Data).

In the Figure 3.13, the magnitude of the parity vector can be mistakenly evaluated as at the acceptable levels in the cases where all the satellites are included. Moreover, in order to be able to detect all the satellites that suffer from the multipath, the differences between each calculation should be formed and analyzed in a comparative way, but finding the set that is not including erroneous measurement may not be possible.

If the percentage of the erroneous measurements exceeds 50 %, RAIM algorithm fails [130]. Moreover, since the measurement errors caused by extreme multipath and NLOS signals do not follow the white Gaussian noise pattern [131], the underlying assumption of the RAIM method does not hold all the time for multipath detection.

Furthermore, with the evolving AI world, different ML algorithms started to be applied for the multipath detection and inconsistency check of the measurements. These methods are discussed in Section 5.3.1.

Chapter 4

Design and testing of robust GNSS receiver architectures for scintillation mitigation

In this Chapter, a detailed comparative study of the different acquisition and tracking methods for GPS L5 and L1 C/A signals in order to test their robustness to the presence of real phase and amplitude scintillations in the propagation environment is presented. The analyzed scintillated data in this analysis are summarized in Table 4.1. The datasets were chosen as representative of events at equatorial and polar regions. The satellite selections are dependent on the observed scintillation effect if the area of scintillation falls between the satellite and receiver.

Table 4.1: Specifications of The Scintillated Data

	Date	Station	Coordinates
1	May 8, 2016 Aug 17, 2016	South African Antarctic Research Base (SANAE-IV), Antarctic	Lat.:71.67278°S Long.: 2.840556°W
2	Sept 13, 2017	Centro de Radioastronomia e Astrofisica Mackenzie (CRAAM), Brazil	Lat: 23.5474825°S Long: 46.6523133°E

Figure 4.1 (a) and (b) show the computed phase scintillation indices for both L1 C/A and L5 signals for the two datasets collected at the Antarctic station. For comparison, the indices computed by a Septentrio PolaRxS PRO professional receiver are also plotted. Due to the polar location of SANAE-IV, the computed S4 indices are low, and only phase scintillation indices have been plotted. The figures show 20-minute length portions of the data affected by the phase scintillation events occurred around 8 p.m. and 4 a.m., respectively. Since the ionospheric scintillation effect on GNSS signals is caused by the scattering due to irregularities

in the distribution of electrons encountered along the radio propagation path, it rarely occurs on all visible satellites simultaneously [132]. GPS signals that are broadcasted from two Block-IIF satellites (PRN 3 and PRN 9) that transmit signals both on the L1 and L5 frequencies experience strong scintillation ($\sigma_\phi > 0.7$) in these data-sets.

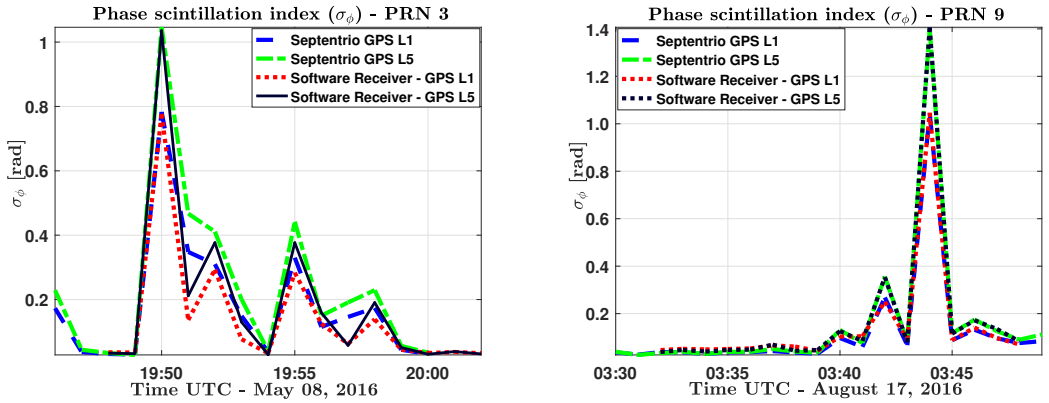

(a) Phase Scintillation (PRN3) - May 8, 2016.

(b) Phase Scintillation (PRN9) - Aug 17, 2016.

Figure 4.1: Phase scintillation index values at GPS L1 C/A and L5 signals (SANAE IV).

Moreover, another event which is observed in the data collected on September 13, 2017 at the Brazilian monitoring station has been considered. Figure 4.2 shows computed amplitude and phase scintillation indices for both L1 C/A and L5 signals. The figures refer to the portions of the data affected by the amplitude and phase scintillation events occurred starting from 2:15 a.m. as denoted by the sharp increases in the indices. As it can be seen, GPS L1 C/A and L5 signals that are broadcasted from Block IIF (PRN-10) satellite are experiencing strong (S_4,σ_ϕ>0.7) and moderate (0.5<S_4,σ_ϕ<0.7) amplitude and phase scintillations. Since ionosphere is a dispersive medium, the type of interaction between the signal and the ionosphere is dependent on the frequency of the signal and both amplitude and phase scintillation levels have an inverse relation with the signal carrier frequency [132]. Therefore, the L5 signal experiences larger signal fluctuations than the L1 C/A during the 45 minutes data collection, as expected.

To sum up, S_4 and σ_ϕ parameters reflect the intensity of the scintillation and disturbance rate on the received power and carrier phase measurements [71]. In the following, the disturbance effects of these events on the acquisition and the tracking structures are analyzed.

The significance of working with real signals has to be noted compared to the analysis often done based on the models that are oversimple with respect to reality. Moreover, although it is observed in Figures 4.1 and 4.2 that the software

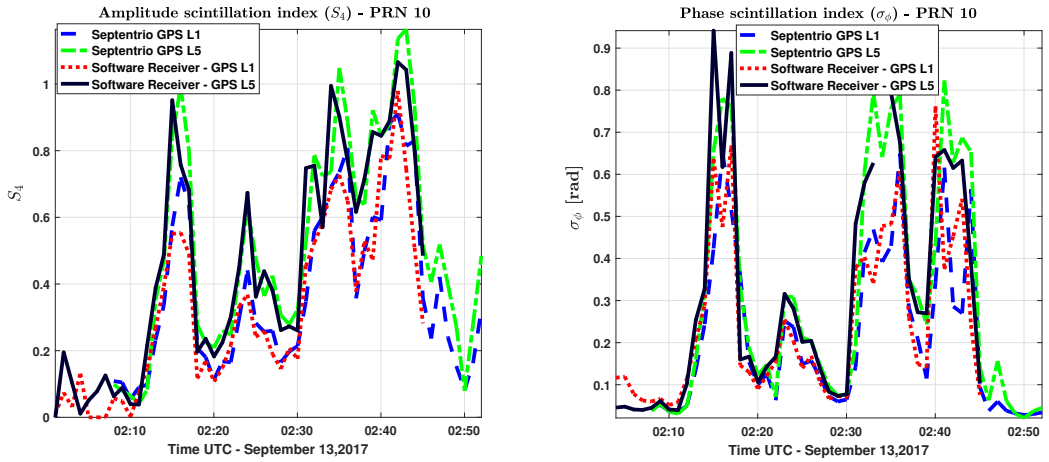

(a) Amplitude Scintillation.

(b) Phase Scintillation.

Figure 4.2: Amplitude and phase scintillation index values at GPS L1 C/A and L5 signals - September 13, 2017 (CRAAM).

receiver (post-processing) solution also provides all amplitude and phase indices continuously like Septentrio PolaRxS PRO, it does not mean both receivers are capable to operate continuously during the scintillation events. The degradation on the observables can be handled by internal algorithms specific to the receivers. In this research work, the software approach provides flexibility, and having access to the full receiver chain and to intermediate signal processing stages allows a deep analysis of the impact of scintillation and to improve the design correspondingly.

4.1 Performance of signal acquisition methods

4.1.1 Acquisition methods

In this work, four L5 and three L1 C/A acquisition methods are implemented and compared in terms of probabilities of detection/false alarm, peak-to-noise floor ratios and acquisition time duration. Although Figure 2.8 shows the time-domain implementation of the acquisition structure with cross-correlations, in this implementation, the cross-correlation of the incoming and generated signal is computed through FFT-based correlation.

The first applied technique (***Method-A***), coherent channel combining, was originally proposed in [133], [134] and [135], and it has been implemented for $T_c = 1$ ms with K non-coherent accumulations in order to be able to neglect the presence of the NH codes. The choice of $T_c = 1$ ms is due to the fact that both primary spreading code and one NH bit are 1 ms long and that a potential bit transition that could lead to degradation when finding the peak in the acquisition is aimed

to be avoided.

The second technique considered (***Method-B***) is the zero-padding algorithm presented in [136] and [42]. This algorithm takes into account the degradation effect of the possible presence of NH bit transitions. These sign transition issues are generally solved by using extended local replica with zero-padding [42]. Zero padding acquisition is implemented by circularly correlating two code periods of the incoming signal with one primary code period of locally generated code appended by one primary code period of zeros. This method produces two peaks in the output and it is possible to find a degraded peak in the second half of the correlation due to NH bit transition [42]. Although this method increases the computational load due to the augmented FFT length compared to Method-A, it also increases the chance of acquiring the satellite signal considering the effect of NH bit transitions. However, selecting FFT length for zero padding is a design parameter to consider in terms of computation issues and an interested reader can find useful materials in [137].

As third strategy (***Method-C***), $T_c = 20$ ms with non-coherent accumulations on the data-less channel is implemented. This method has been proposed in different configurations for L5 signals in [134] and [136]. Such an integration is highly effective for low signal-to-noise ratio conditions; however, it is computationally heavy with respect to the previous two aforementioned methods. Moreover, since L5 signal includes secondary NH codes (differently from L1 C/A), a misalignment of the NH code could cause false peaks in the L5 CAF output. In the scientific literature, in order to obtain a perfect synchronization with NH codes, a couple of techniques have been proposed. In the first approach, it is suggested to employ consecutive acquisitions with short integration time to detect the NH bit transitions in a tree data structure [138] or to eliminate secondary code ambiguity based on multi-hypothesis in Galileo primary code acquisition [139]. The aforementioned methods described in [138] and [139] that apply possible secondary code combinations in an evolutionary tree structure are improved by coherently extending the integration time by testing all possible combinations through the m-sequence method [140] and coherently accumulating the correlation values obtained over shorter length sequences [141]. In the second approach, the synchronization is obtained by implementing correlations with secondary codes [142] or by combining those secondary correlations [143] to reduce the number of possible secondary code delays and complexity. In this implementation, the first approach by applying an exhaustive search considering all possible combinations in a hierarchical tree structure is followed. At first consecutive zero-padding acquisitions over primary code lengths of the incoming signal are performed by including both first and second half of the correlation output. The peaks of CAF are evaluated to detect the correlation peaks which are distributed along the Doppler axis due to sign transitions. The NH code phase is obtained by exhaustive testing. Later, by generating the full-length NH code with the known phase, Method-C is applied. In Method-C, while T_c can be chosen as

20 ms for L5 pilot channel, it is set to 10 ms for L1 C/A due to possible data-bit transitions. Between two consecutive 10 ms data intervals, at most one navigation data bit phase transition exists and one of these has no data bit phase transition [144].

In the last considered option (***Method-D***), instead of detecting all the sign-transitions of the NH codes, the differentially coherent channel combining with sign recovery algorithm whose implementation details are available in [145] and that has a lower computational complexity is applied. The motivation of this algorithm is to decrease the effect of the NH bit sign-transition by combining the information of both cases where the NH bits are 1 and 0 for two consecutive 1 ms intervals of data. Since the motivation comes from the existence of the secondary codes, this method has not been applied to the L1 C/A signal.

Table 4.2 summarizes the parameters of the implemented acquisition methods for L1 C/A and L5. The first analysis has been performed under non-scintillated conditions.

Table 4.2: Specifications of the Acquisition Methods

		Method A	Method B	Method C	Method D
Coh. Integ. Time [ms]	L5	1	1	20	2
	L1 C/A	1	1	10	-
Number of Non.Coh Accumulations		3	3	3	1

In Table 4.3, the results obtained for the performance metrics are given. The test was realized by processing the data that belong to 8 May 2016 (see Figure 4.1 (a)). By considering the first 3 minutes interval of the data in which the scintillation has not started yet, the peak-to-floor ratios are computed for each method. The results in Table 4.3 are the mean values obtained. Moreover, computed mean C/N_0 values for GPS L5 and L1 C/A signals are 51 dBHz and 48 dBHz, respectively. As it can be seen in Table 4.3, when the coherent integration time is extended, an improvement in the peak-to-noise ratio is observed, but at the same time, an increment of the computational load, which is the consequence of the time dedicated by the receiver to the acquisition stage, is observed. The number of non-coherent accumulations is decided experimentally by trying to make it as lowest as possible and at the same time having an acceptable peak-to-floor ratio.

In Table 4.3, there are two different values for Method-D as being different from the other methods. The difference between the two cases corresponds to the situations where the NH bit sign transition occurred and not occurred in consecutive two 1 ms intervals. The number of non-coherent accumulations is set to 1 to make

Table 4.3: Performance Metrics of the Acquisition Methods

		Method A	Method B	Method C	Method D
Peak-to-floor ratios [dB]	L5	23.12	25.55	39.5	$14.25 - 17.81$
	L1 C/A	19.79	21.01	33.1	-
Acq. time per SV*	L5	t_5	$2.5t_5$	$14t_5$	$1.6t_5$
∼Comput. Load	L1 C/A	t_1	$2t_1$	$8.25t_1$	-

*Front-end sampling frequencies for L1 and L5 signals are 5 MHz and 30 MHz, respectively. Since the number of the samples for the chips are different, two different time-measurement parameters (t_5 and t_1) are defined, obtaining that $t_5 = 3.65t_1$.

it simpler, otherwise, the number of different peak-to-noise ratio values increase depending on the number of possible NH bit combinations. Therefore, it is inferred that the performance of Method-D is dependent on the observation of NH bit change in the considered 2 ms coherent integration time interval.

Furthermore, Figure 4.3 (a) and (b) show the ROC curves, which are the plots of the probability of detection (P_D) versus the probability of false alarm (P_{FA}) at the search space level, of the implemented acquisition algorithms for GPS L5 pilot and GPS L1 C/A signals, respectively. In fact, for example in case of non-coherent acquisition, probability of false alarm and probability of detection can be written as [146]:

$$P_{FA,K}(\beta) = \exp\left(-\frac{\beta}{2\sigma_n^2}\right) \sum_{i=0}^{K-1} \frac{1}{i!} \left(\frac{\beta}{2\sigma_n^2}\right)^i \tag{4.1}$$

$$P_{D,K}(\beta) = \mathrm{Q_K}\left(\sqrt{\frac{K\lambda}{\sigma_n^2}}, \sqrt{\frac{\beta}{\sigma_n^2}}\right) \tag{4.2}$$

where β is the detection threshold and $\mathrm{Q_K}(a, b)$ is the generalized Marcum-Q function. λ and σ_n^2 are computed from CAF outputs [13, 133, 146]. λ is the non-centrality parameter of the test statistics $S_K(\tau, f_D)$ that is a non-central χ^2 random variable with $2K$ degrees of freedom when the local signal is aligned with the received signal [145]. σ_n^2 is the variance of the in-phase ($Y^2_{I,p/d_k}$) and quadrature-phase ($Y^2_{Q,p/d_k}$) correlator outputs. Moreover, the successful acquisition of a satellite signal is declared when $S_K(\tau, f_D)$ passes the decision threshold (β) for a value of τ and f_D. ROC curves are then obtained (varying β) for each methods at each second (i.e. for the C/N_0 experienced at that epoch).

As it can be seen in Figure 4.3, the performance of the Method-A is not remarkably better than the Method-D for GPS L5 pilot channel. However, the zero-padding method (Method-B) is slightly better than the Method-A. Moreover, as expected, extending the integration time (Method-C) provides an improvement in the performance. The performance improvement in the probability of detection of GPS L5 signal compared to the L1 C/A signal is induced from 3 dBHz difference in the signal-to-noise ratio.

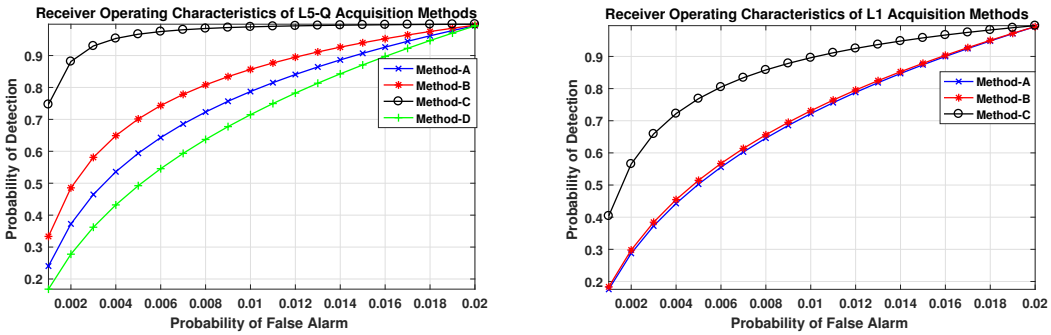

(a) GPS L5 Pilot Signal ($C/N_0 = 51$ dBHz). (b) GPS L1 C/A Signal ($C/N_0 = 48$ dBHz).

Figure 4.3: ROC curves of the implemented methods for GPS L1 C/A, L5 signals under no-scintillation.

After having analyzed the performance of the implemented methods with the non-scintillated data, a study on the scintillation effect on the L5 and L1 C/A acquisition stages is presented in the following subsection.

4.1.2 Performance Comparison of the Acquisition Methods

After the description of acquisition methods, they have been tested, at first, on the data sets that were collected on May 8 and August 17, 2016 (Figure 4.1 (a)-(b)) in the Antarctic stations SANAE IV and that are affected only by strong phase scintillation. The estimated mean C/N_0 values for the data-sets are 51 dBHz and 46 dBHz for GPS L5 signals, respectively. However, for GPS L1 C/A signals, they are estimated as 48 dBHz and 44 dBHz, respectively. In the analysis, the acquisition algorithms (with $P_{FA} = 0.001$) are run every second for the whole data collection and then the amount of time (duration) that the algorithms fail to acquire the satellites (i.e. PRN3 and PRN9) affected by strong phase scintillation has been checked. This process is repeated for all the acquisition methods for GPS L5 and L1 C/A signals. It is observed that during the phase scintillation events the signal is acquired all the time for all the methods. This result is not surprising since the phase scintillation has less impact on the acquisition stage. It points out that the rate of phase changes occurred during the phase scintillation events stays quite constant over the integration time or this effect is minimal in the acquisition

process. In order to analyze the effects of the phase scintillation, the changes in the ROC curves due to scintillation are also analyzed.

Such ROC curves are computed by employing the acquisition results at each second. Every second has been identified where the scintillation is strong ($\sigma_\phi > 0.7$) or no-scintillation exists ($\sigma_\phi < 0.2$). In this way, it has been possible to make a statistical and fair comparison between the case of no-scintillation and phase scintillation. For the two cases, the mean P_D values are computed for each given P_{FA} values. Then, the differences between the mean P_D values of no-scintillation and scintillation cases for the same P_{FA} values are computed. This procedure is repeated for the two data sets.

Figures 4.4 and 4.5 show the loss in the P_D values of the aforementioned L5 and L1 C/A acquisition methods under phase scintillations for the two events. It is observed that, in case of strong scintillation, there is a loss in P_D of only 0.013-0.002 with respect to the case without scintillation. Whereas the ROC curves in Figure 4.3 belong to a timestamp, Figures 4.4 and 4.5 cover a duration during which different levels of phase scintillation exist, and the C/N_0 changes in time as it might be expected. Therefore, due to its experimental nature in which the data are analyzed for different levels of scintillation, any conclusion related to shapes of curves would be misleading except the comparison of the loss in P_D among the methods. This is why the analysis results are limited to inferring the loss in P_D of the acquisition methods under phase scintillation.

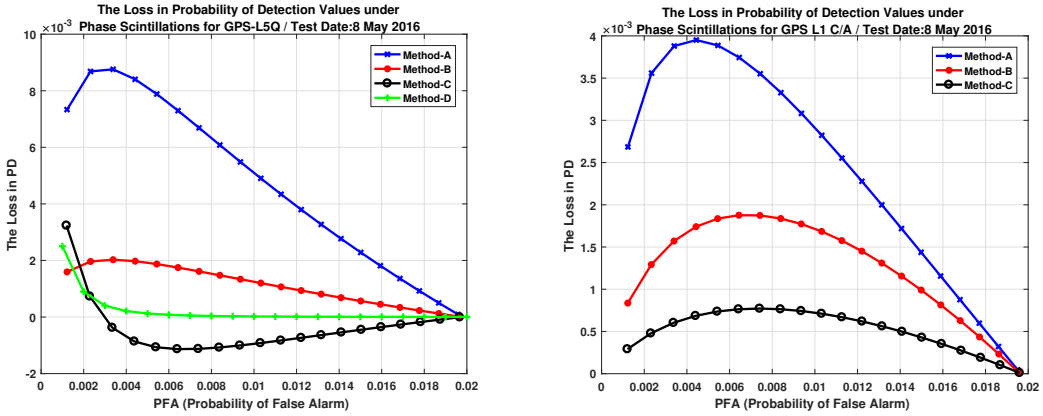

(a) GPS L5 Pilot Signal.

(b) GPS L1 C/A Signal.

Figure 4.4: The loss in PD of the acquisition methods for GPS L1 C/A, L5 signals under phase scintillation - 8 May 2016.

In the second test, the data that were collected on September 13, 2017 in Brazil have been used. In this event, phase scintillation is mixed with amplitude scintillation. Figure 4.6 shows the acquisition performance of the methods during 45 minutes length data. The percentages of successful acquisition times (with

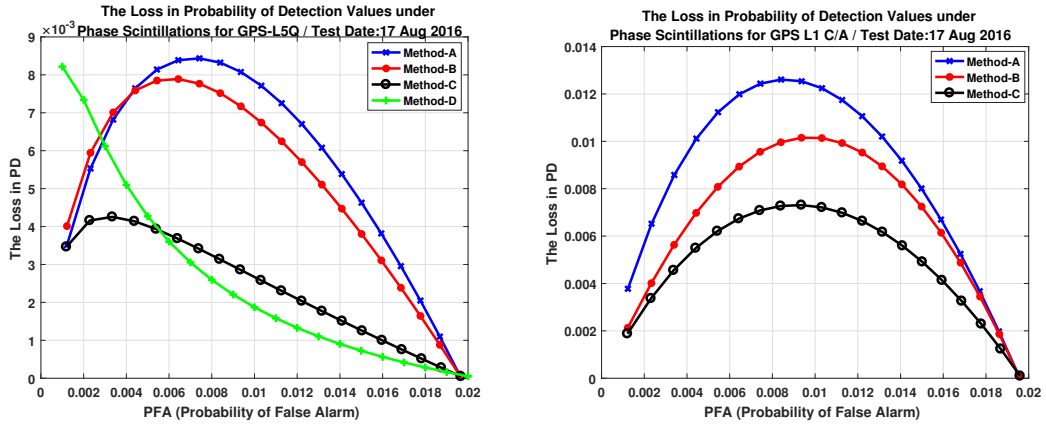

(a) GPS L5 Pilot Signal.

(b) GPS L1 C/A Signal.

Figure 4.5: The loss in PD of the acquisition methods for GPS L1 C/A, L5 signals under phase Scintillation - 17 August 2016.

$P_{FA} = 0.001$) are computed and summarized in Table 4.4.

Table 4.4: Percentages of Successful Acquisition Times under Amplitude and Phase Scintillation Event – Test Date: 13 September 2017

	Method A	Method B	Method C		Method D
	T=1 ms $K = 3$	T=1 ms $K = 3$	T=10 ms $K = 3$	T=20 ms $K = 3$	T=2 ms $K = 1$
L5-Q	79.96 %	88.73 %	98.55 %	98.90 %	64.49 %
L1 C/A	57.26 %	59.71 %	99.78 %	-	-

*T is the coherent integration time and K is the number of non-coherent accumulations.

As it can be seen in Table 4.4, the acquisition performance of the L5 outperforms L1 C/A in both Method-A and Method-B. However, as mentioned in Section 2.2.2, the signal structures and transmitted power are different in L1 C/A and L5. C/N_0 values of GPS L5 signals are higher than GPS L1 C/A signals. On the contrary the scintillation is stronger in GPS L5 signal than GPS L1 C/A signal as it can be seen in Figure 4.1 (a)-(b) and Figure 4.2 (a)-(b). At the same time, it is observed that Method-C outperforms the other methods in both cases.

Moreover, so as to compensate the C/N_0 difference between GPS L1 C/A and L5 signals and also to see whether performance difference is caused by the signal level difference, extra gain to L1 C/A signal processing is provided. If the integration

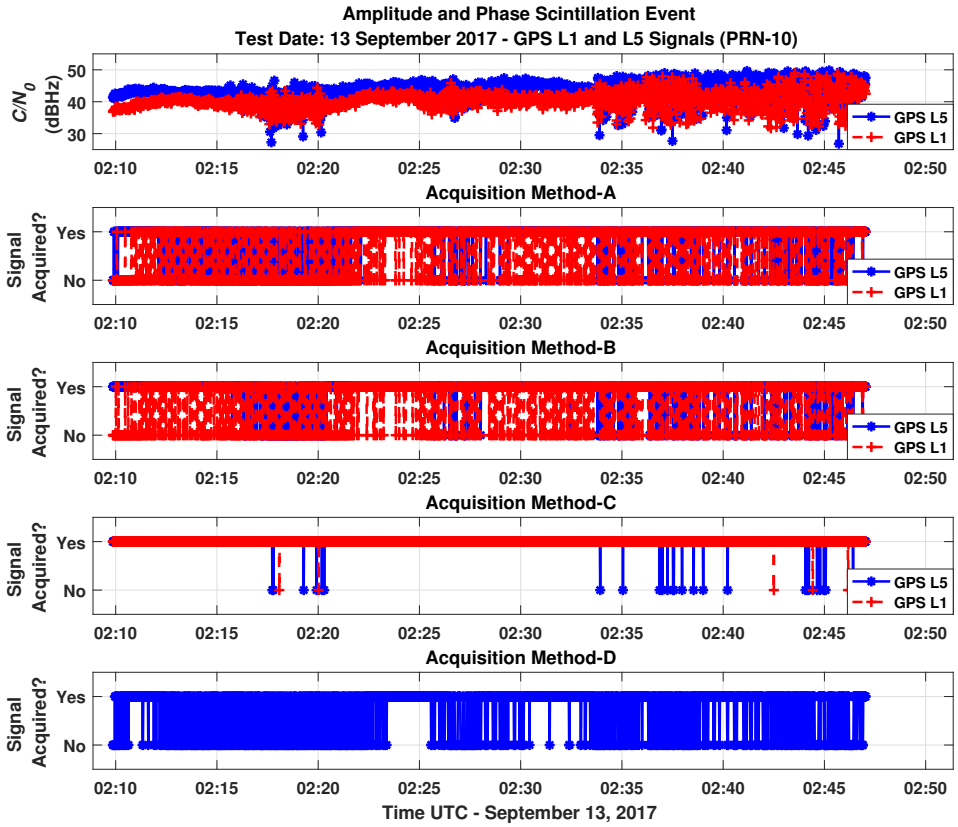

Figure 4.6: Performance comparison of GPS L1 C/A, L5 signal acquisition methods under amplitude and phase scintillation - Test Date: 13 September 2017.

time is extended to 2 ms, theoretically, an additional 3 dB coherent integration gain is obtained, and in this case, it is expected that L1 C/A performance could get better than L5. As expected, it is observed that for 2 ms and 3 ms coherent integration time implementation for GPS L1 C/A, the percentages of successful acquisition times reach up to 89.74 % - 95.18 %. However, instead of increasing the coherent integration time of L1 C/A acquisition method, if the number of non-coherent accumulations is increased to $K = 3$ and $K = 7$ for Method-A, it is observed that the percentages of successful acquisition times increase to 74.79 % and 77.16 %, respectively.

Summarizing, it is observed that while phase scintillation is not at the level to prevent the acquisition of the signal, strong amplitude scintillation can prevent the acquisition of the signal. In that case, extending integration time can be a solution, and Method-C performs best among the other methods. Moreover, in the comparison of Method-A to Method-B, which both have the lowest coherent integration

times that are equal to one code period, it is observed that the performance of Method-B is slightly better than Method-A. Although Method-B having an augmented FFT length due to zero-padded local code increases the computational load compared to Method-A, Method-B producing two peaks in the output increases the chance of acquiring the satellite signal that might be suffering from the scintillation effect and/or possible bit transitions.

4.2 Performance of signal carrier tracking methods

In the following, the analyses are limited to the signal carrier tracking stage, whose objective is to wipe off the carrier by generating a perfectly aligned one. Because carrier tracking is so susceptible to the scintillation due to PLL's stringent tracking threshold the equatorial phase scintillation adversely affects the operation of carrier tracking leading to cycle slips and complete loss of carrier lock.

To have robust architectures optimized to operate in a harsh ionospheric environment, firstly PLL tracking loops are tested by considering the different choices for the loop filter order (2^{nd} or 3^{rd}), the coherent integration time (T) and the carrier noise bandwidth (B_n). The order of the filter and noise bandwidth determine the loop filter's response to signal dynamics and in PLL loop filter design there is also a tradeoff in the decision of T and B_n parameters [147].

Figures 4.7, 4.8, 4.9 (a) and (b) show the changes in the values of correlator outputs ($I_{k,d/p}$ and $Q_{k,d/p}$), raw PLL discriminator output ($\delta\varphi_k$), C/N_0 and carrier frequency estimations during the occurrence of scintillation and no-scintillation activities for GPS L5 data, pilot channels and GPS L1 C/A signal. As it can be seen in Figures 4.7, 4.8, 4.9 (a) and (b), the amplitude of the prompt correlator output ($I_{k,d/p}$) both increases and decreases during the scintillation event. Because the diffracted signals interfere with the actual signal and they are added to the actual signal both constructively and/or destructively that yields to alternately both attenuation and strengthening in the signal amplitude and C/N_0 values measured by the user [148].

The data that were collected on 13 September 2017 are used for the analysis in this section. In the analysis shown in the figures, the PLL design parameters $B_n = 10$ Hz, $T = 10$ ms and $T = 20$ ms are selected for GPS L5 and GPS L1 C/A signals, respectively. Furthermore, at the same conditions, a KF-based tracking, of which implementation details are provided in Appendix A.2.2 and that provides more flexibility thanks to a time-varying bandwidth and gain, has been evaluated and compared in terms of the residual effects on the receiver observables and the internal parameters.

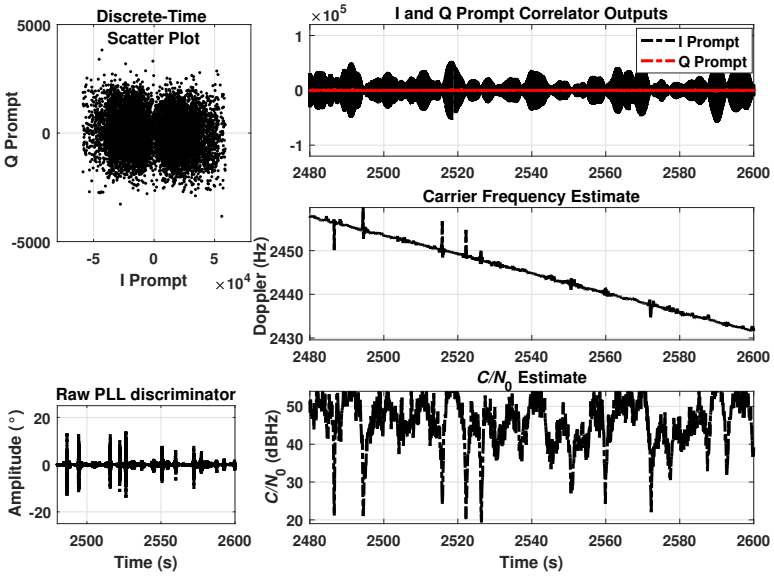

(a) GPS L5 Data Channel Outputs with 2^{nd} Order PLL, $B_n = 10$ Hz, $T = 10$ ms - under strong scintillation.

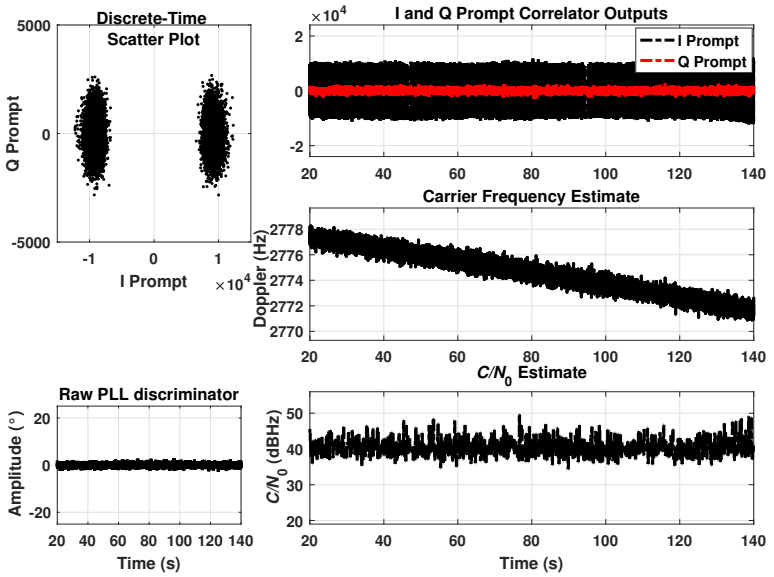

(b) GPS L5 Data Channel Outputs with 2^{nd} Order PLL, $B_n = 10$ Hz, $T = 10$ ms - no-scintillation

Figure 4.7: Comparison of the tracking observables and internal parameters for L5 data channel under strong scintillation and no-scintillation - Test Date: 13 September 2017.

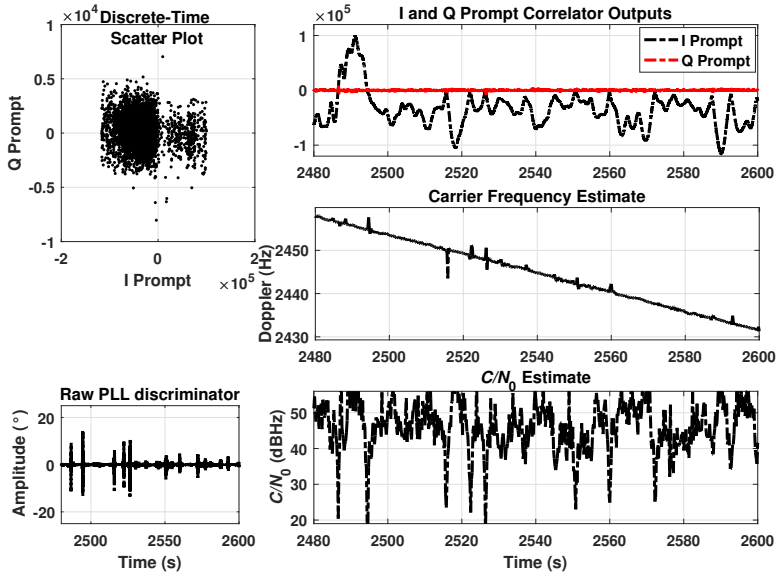

(a) GPS L5 Pilot Channel Outputs with 2^{nd} Order PLL, $B_n = 10$ Hz, $T = 20$ ms - under strong scintillation.

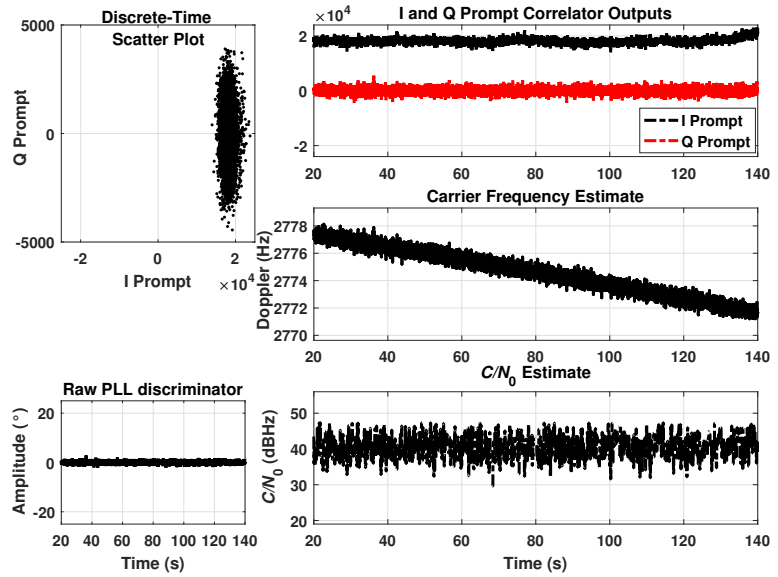

(b) GPS L5 Pilot Channel Outputs with 2^{nd} Order PLL, $B_n = 10$ Hz, $T = 20$ ms - no-scintillation.

Figure 4.8: Comparison of the tracking observables and internal parameters for L5 quadrature channel under strong scintillation and no-scintillation - Test Date: 13 September 2017.

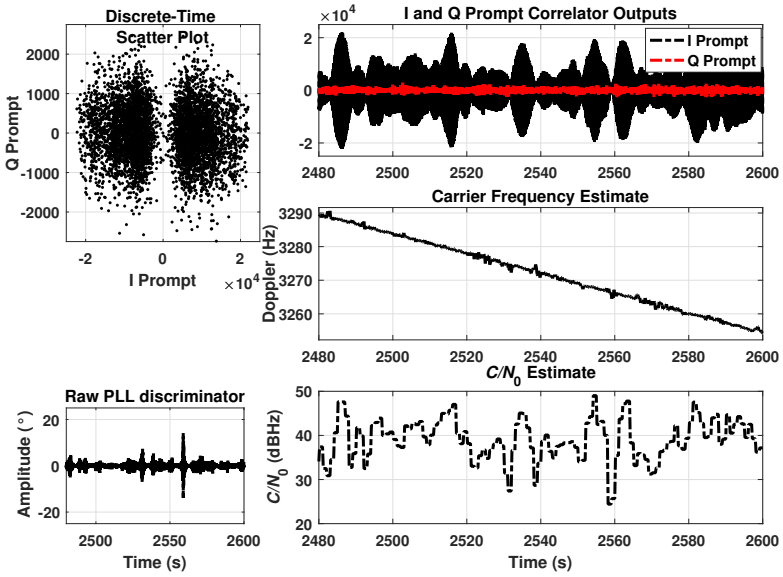

(a) GPS L1 C/A Signal Outputs with 2^{nd} Order PLL, $B_n = 10$ Hz, $T = 20$ ms - under strong scintillation.

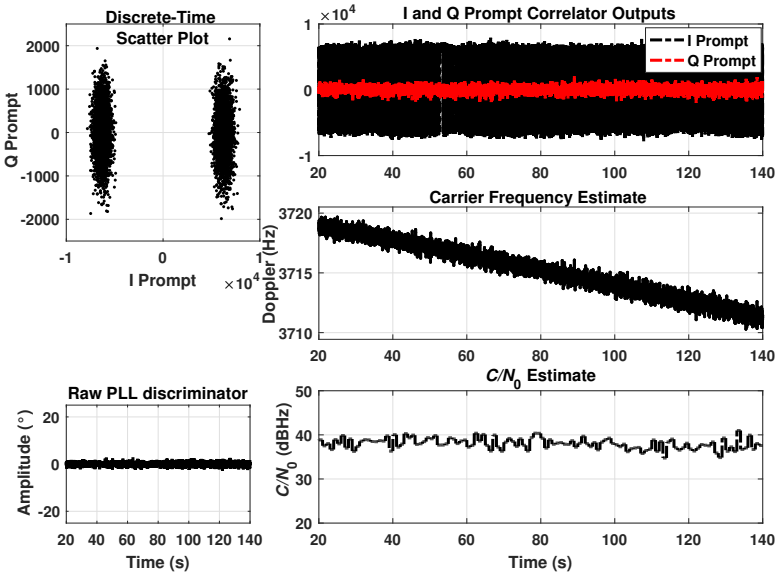

(b) GPS L1 C/A Signal Outputs with 2^{nd} Order PLL, $B_n = 10$ Hz, $T = 20$ ms - no-scintillation.

Figure 4.9: Comparison of the tracking observables and internal parameters for L1 C/A signal under strong scintillation and no-scintillation - Test Date: 13 September 2017.

4.2.1 Standard Deviation of Doppler Estimations

The best PLL parameters to be able to track the Doppler frequency accurately are tried to be found. Doppler shift measurements allow us to compare the tracking robustness in the presence of scintillation effects. Figures 4.7, 4.8, 4.9 (a) show 120 seconds portion of the Doppler estimates of the processed data, which experience both strong amplitude and phase scintillation. By applying different choices of the loop orders, bandwidth (B_n) and integration time (T), the effects of the PLL parameters on the tracking stage under scintillation have been analyzed. In the analysis, while the extended integration time is set to $T = 10$ ms in the L5 data channel by considering the data bit interval, in the L5 quadrature (dataless) channel the integration time is extended to $T = 20$ ms. Moreover, so as to provide a perceptive comparison in terms of the effect of noise bandwidth, commonly used bandwidths with 5 Hz increments are included in the analysis. Due to scintillation an increment of the standard deviation of Doppler measurements can be observed with different settings of tracking parameters.

To have better comparison, the maximum values of the standard deviations of the Doppler measurements, each value computed on a non-overlying block of 100 ms, have been estimated and all the results are summarized in Tables 4.5 and 4.6 for scintillation and no-scintillation cases, respectively.

It is observed that processing the L5 data or the pilot channel with $T = 1$ ms has no advantages over each other, as expected. Moreover, although there is not a remarkable performance difference with using L1 C/A or L5 signals in case of $T = 1$ ms, it is clear that the performance degrades with increasing B_n values which means that the noise level can be reduced by reducing the noise bandwidth. On the contrary, when the coherent integration time is extended to 10 ms for the L5 data channel and 20 ms for the L5 pilot channel and GPS L1 C/A signal, the latter shows a lower error in the Doppler measurement for low value of bandwidth (i.e. < 10 Hz).

As it can be seen in Table 4.5, there is a sharp increase in the values due to the change of B_n from 15 Hz to 20 Hz especially in the case of $T = 20$ ms. Since the product B_nT increases, the true noise bandwidth tends to be larger than the aimed value and hence the loop filter becomes unstable [147]. Moreover, although the second order is unconditionally stable, the third order can be unstable under fluctuating C/N_0 values due to scintillation. In the cases of third order loop filter with $B_n = 15$ and 20 Hz and $T = 20$ ms, tracking is completely is lost after some time.

Table 4.5: Max value of the standard deviations of the Doppler measurements [Hz]. Each std-value corresponds to 100 ms of 3-minute long signal record of the strong scintillation event - Test Date: 13 September 2017

			2^{nd} Order PLL				3^{rd} Order PLL			
			Noise Bandwidth (B_n) [Hz]				Noise Bandwidth (B_n) [Hz]			
			5	10	15	20	5	10	15	20
Integ. Time (T)	1ms	L5I	2.16	4.00	6.19	8.34	2.49	4.61	7.28	9.33
		L5Q	2.01	3.97	6.01	8.09	2.26	4.57	7.21	9.23
		L1 C/A	2.19	3.83	6.01	8.39	2.18	4.79	7.49	9.54
	L5I: 10 ms	L5I	**1.89**	5.09	7.59	10.85	2.68	5.56	7.75	10.8
	L5Q: 20 ms	L5Q	**1.96**	5.64	8.50	14.94	1.98	6.00	9.90	143
	L1 C/A: 20 ms	L1 C/A	**1.90**	5.00	7.44	15.55	2.49	5.38	34.2	167

Table 4.6: Max value of the standard deviations of the Doppler measurements [Hz]. Each std-value corresponds to 100 ms of 3-minute long signal record of the no-scintillation event - Test Date: 13 September 2017

			2^{nd} Order PLL				3^{rd} Order PLL			
			Noise Bandwidth (B_n) [Hz]				Noise Bandwidth (B_n) [Hz]			
			5	10	15	20	5	10	15	20
Integ. Time (T)	1ms	L5I	0.68	1.38	2.08	2.80	0.78	1.58	2.38	3.19
		L5Q	0.66	1.33	2.01	2.69	0.76	1.51	2.29	3.06
		L1 C/A	0.89	1.82	2.75	3.67	1.02	2.07	3.10	4.16
	L5I: 10 ms	L5I	**0.29**	0.65	1.08	1.61	0.32	0.69	1.11	1.69
	L5Q: 20 ms	L5Q	**0.28**	0.74	1.85	4.61	0.31	0.82	1.58	2.75
	L1 C/A: 20 ms	L1 C/A	**0.39**	0.93	2.17	5.49	0.45	1.03	2.02	3.53

4.2.2 Phase Error

A PLL discriminator, shown in the Figure 2.12 carrier tracking structure, computes the difference between the phase of the incoming signal and the locally generated signal. Here two-quadrant Costas PLL discriminator is used, which outputs the phase error as:

$$\delta\varphi_k = \tan^{-1}\left(\frac{Q_{k,d/p}}{I_{k,d/p}}\right) \tag{4.3}$$

where ($\delta\varphi_k$) is the estimated carrier phase error over the integration time (T).

Figures 4.7, 4.8 (a)-(b) show the tracking results of the processed L5 data and pilot signals. The tracking results of the L5 data channel show similar characteristics with L1 C/A shown in Figure 4.9. Since L1 C/A and L5 data signals have 180-degree phase ambiguity due to the navigation data, NCO creates two different

cloud of points that are visible in the Figures 4.7,4.9 (b) in the discrete-time scatter plot. However, the tracking results of the L5 pilot (Figure 4.8 (b)) channel with extended integration time (20 ms) differs from them in terms of the phase measurement. In both cases, the amplitude scintillation causes the elongation of the clouds due to the occurrence of the power fades, which can be clearly seen in the IQ prompt correlator in time graphs. When the two clouds get closer to each other while tracking the L1 C/A and the L5 data-channel signals, it causes an increase in the error with the increase in the standard deviation of the phase measurements. Moreover, the abrupt phase changes causing the phase error are seen at the output of the discriminator in the figure. Finally, the trend and the scintillation of the C/N_0 values during the scintillation can be observed in time.

Furthermore, the computed phase error values in the case of both scintillation and normal conditions are compared and their trends at different C/N_0 values are shown in Figure 4.10 (a)-(b) for L5 and L1 C/A signals, respectively. The phase error values in Figure 4.10 are the mean of the computed values at each 1 dB-Hz intervals. As expected, the phase error is higher at lower C/N_0 values and it decreases with increasing C/N_0. It is inferred that a constant degradation in the accuracy of the carrier phase measurements can be encountered due to scintillation and hence fluctuating C/N_0. It can be observed that the L1 C/A signal tracking provides a phase error that is slightly higher (few degrees) than the one computed for the L5 signal under the same condition of the scintillations, namely when they have the same C/N_0 values. In the L5 case, due to larger fluctuations when C/N_0 goes to lower values, phase error reaches to higher values than observed in L1 C/A. Besides, it is observed that the C/N_0 measurements stay in the limited range without having fluctuation when there is no-scintillation. It has to be noted that since the real data are processed in the analyses, in Figure 4.10, the computed phase error values are linked to the existing computed C/N_0 measurements in the data.

Moreover, in the first data set (8 May 2016) in which having scintillation signals with only phase variations and no amplitude fading, the same analysis is made. Phase error values at different C/N_0 values are plotted in Figure 4.11. As it can be inferred from Figure 4.11, phase changes are not as abrupt as observed in the data set (13 September 2017) that is collected in the CRAAM station. A good signal-to-noise ratio is observed due to there is no amplitude scintillation and deep fading.

As analyzed up to now, the loop order, the bandwidth (B_n) and the integration time (T) are typically a-priori set in the PLL structure. In the following subsections, in order to evaluate the robustness of a KF-based PLL with respect to a traditional 2^{nd} order PLL, two parameters have been considered: Phase Lock Indicator (PLI) and PLL noise jitter.

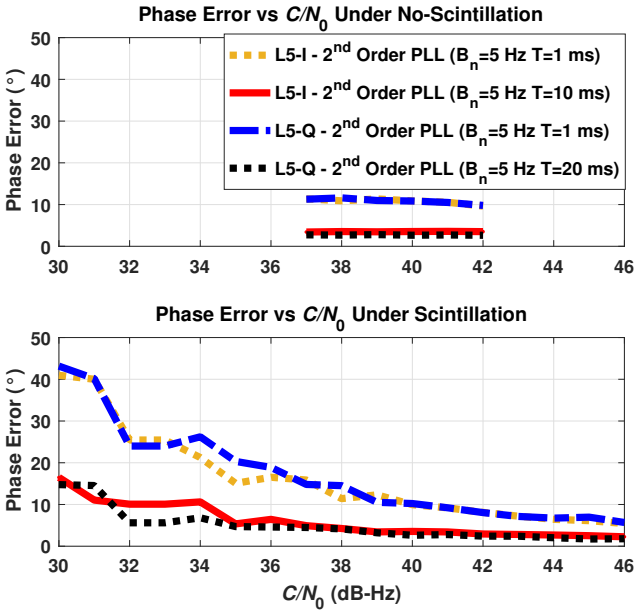

(a) GPS L5 Data - Pilot Signals.

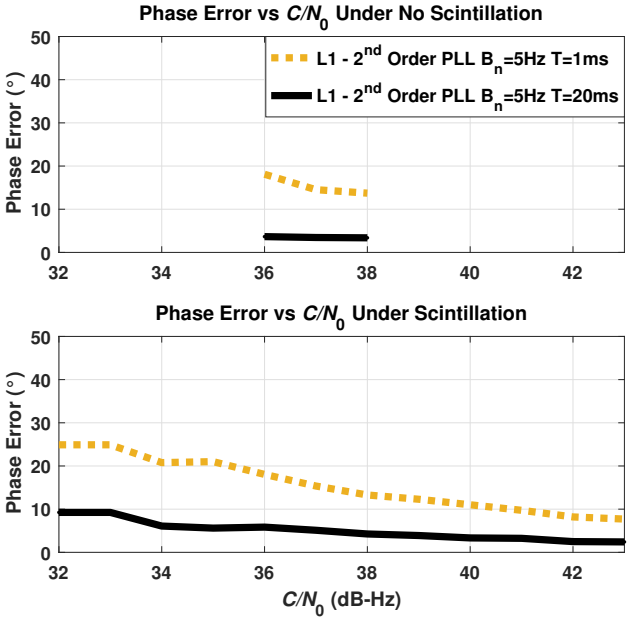

(b) GPS L1 C/A Signal.

Figure 4.10: Phase error vs C/N_0 comparison for L1 C/A, L5 data and pilot channels under scintillation (amplitude + phase) and no-scintillation cases - Test Date: 13 September 2017.

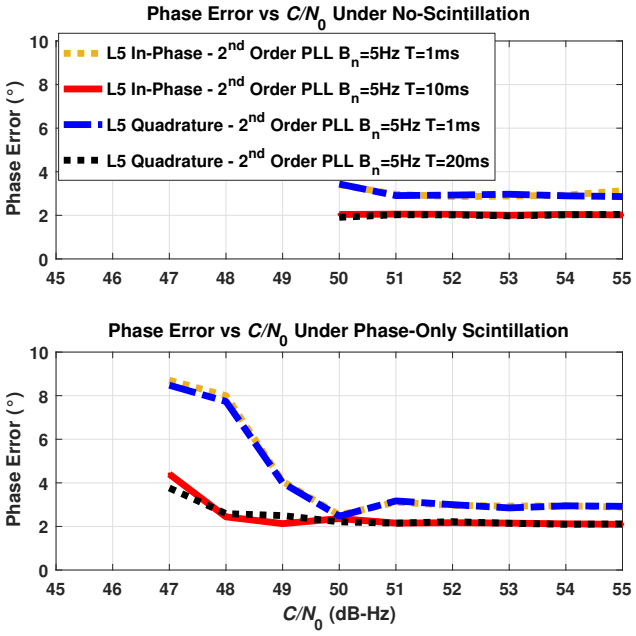

(a) GPS L5 Data - Pilot Signals.

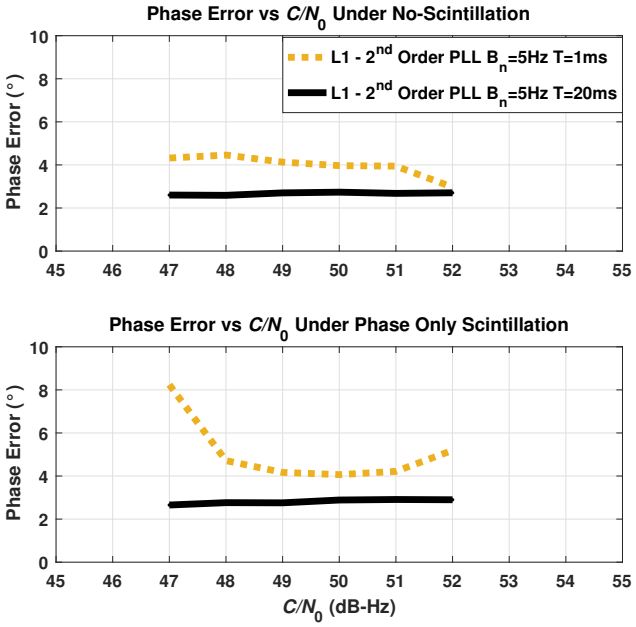

(b) GPS L1 C/A Signal.

Figure 4.11: Phase error vs C/N_0 comparison for L1 C/A, L5 data and pilot channels under phase-only scintillation and no-scintillation cases - Test Date: 8 May 2016.

4.2.3 Tracking Lock Indicator

PLI is computed by considering the prompt IQ correlator outputs of the carrier tracking algorithm [149]:

$$PLI_k = \frac{I_{k,d/p}^2 - Q_{k,d/p}^2}{I_{k,d/p}^2 + Q_{k,d/p}^2} \approx \cos(2\Delta\varphi_k) \tag{4.4}$$

where $PLI = 0.866$ is taken as the acceptable threshold which corresponds to $\Delta\varphi = 15°$ as the limit of the phase error in the implementations. The phase error threshold has been decided by considering the results provided for no-scintillation cases in the previous analysis.

In the analysis, the PLI samples which are less than 0.866 are indicated as loss of tracking points and the number of the samples is used as the performance assessment parameter for the comparison of the different algorithms. Figure 4.12 shows the computed PLI values of the L5 data, pilot channels and L1 C/A signals when the signals experience both strong phase and amplitude scintillations. It is observed that with short integration time implementation, signal tracking is lost for a long time.

Table 4.7 summarizes the unsuccessful tracking percentages for L5 data-pilot channels and L1 C/A signal with different integration times in 3 minutes length of the processed data for PLL and KF-based tracking structures. When the integration is extended to $T = 10$ ms and $T = 20$ ms, the percentages of the loss-of-tracking decrease.

Table 4.7: PLL and KF-based Carrier Tracking - Percentages of Unsuccessful Tracking During 3-minute Length Strong Scintillation Event - 13 September 2017

Carrier Tracking	L5-I		L5-Q		L1 C/A	
	$T = 1$ ms	$T = 10$ ms	$T = 1$ ms	$T = 20$ ms	$T = 1$ ms	$T = 20$ms
2^{nd} Order PLL $B_n = 5$ Hz	12.03 %	2.37 %	12.26 %	2.19 %	27.40 %	1.99 %
KF-Based	11.44 %	1.91 %	11.53 %	1.14 %	26.12 %	1.33 %

As mentioned, KF-based carrier tracking algorithm outperforms the PLL-based tracking; however, it can also fail under phase scintillation accompanied by strong amplitude scintillation conditions. With KF implementation, it has been observed that the tracking is improved and the loss-of-tracking percentages decreased for the L5 data, pilot and L1 C/A signal.

Furthermore, in the first data set (8 May 2016) in which having scintillation signals with only phase variations and no amplitude fading, both the traditional PLL and the Kalman-based carrier tracking structure have been used to process the signals. In this case, both PLL and KF-based carrier tracking performed well without experiencing any loss-of-lock. It can also be inferred from Figure 4.11

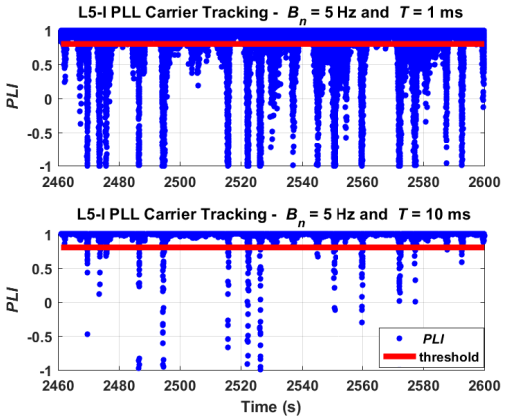

(a) GPS L5 Data Channel.

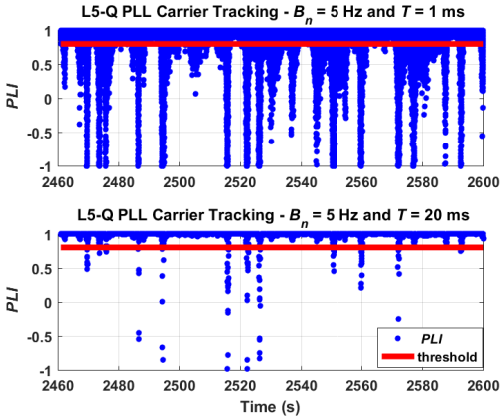

(b) GPS L5 Pilot Channel.

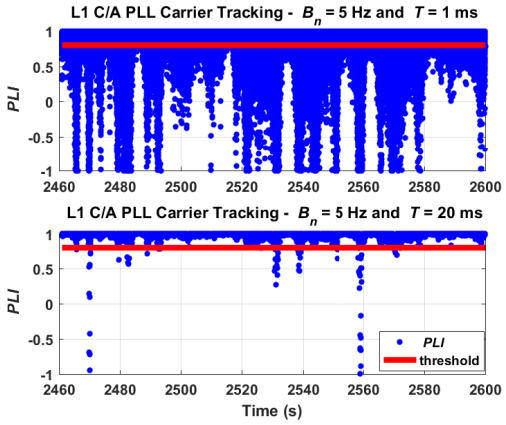

(c) GPS L1 C/A Signal.

Figure 4.12: PLL carrier tracking - PLI values of L5 data, pilot channels and L1 C/A signal under strong amplitude and phase scintillations - Test Date: 13 September 2017.

because computed phase error values are not higher than the threshold that is considered for loss of tracking.

4.2.4 Jitter

Phase jitter is the root sum square of every source of the uncorrelated phase error, such as thermal noise and oscillator noise [147]. The jitter is estimated by computing the standard deviation of the carrier phase tracking error defined in (4.3) and as the last metric, it has been used for performance comparison [150].

In the analysis, first of all by considering the phase and amplitude indices shown in Figure 4.2 (a)-(b), the scintillation effect is classified as strong, moderate, weak and no-scintillation and the starting/ending times are defined for each. For the

defined portions-in-time, the phase jitter values are computed for each method and the signal type. Figure 4.13 shows the jitter values of the tracking outputs for L5 data, pilot channels and L1 C/A signal.

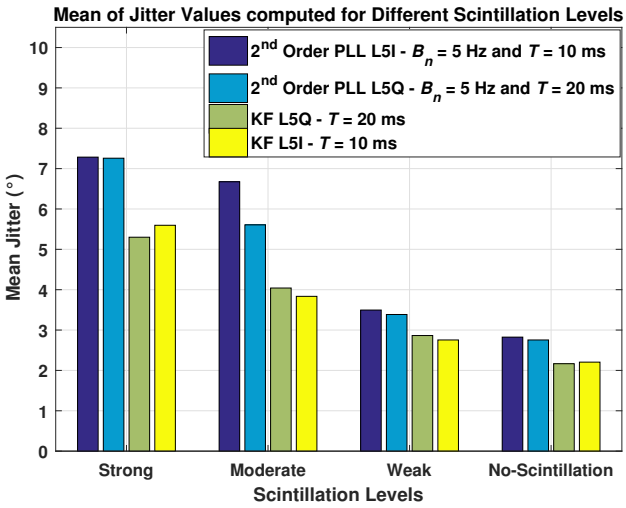

(a) GPS L5 Signal.

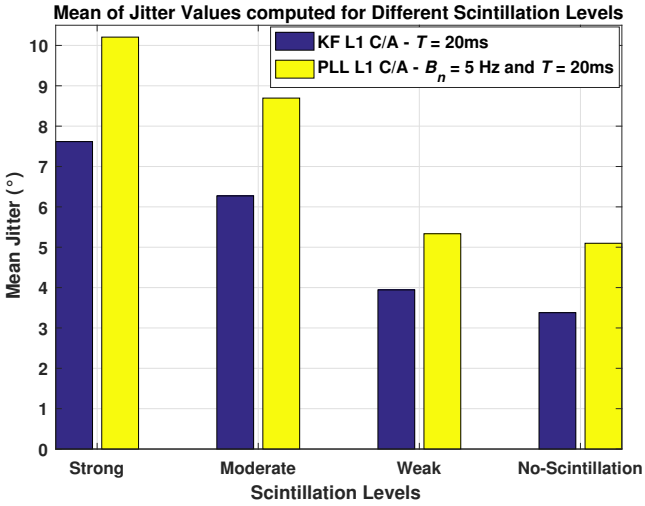

(b) GPS L1 C/A Signal.

Figure 4.13: Carrier Tracking Noise Jitter of Different Methods for L5 Data, Pilot Channels and L1 C/A Signal - Test Date: 13 September 2017.

It is expected that the L5 pilot channel, which uses a longer integration time and thus gives a higher SNR in output than the L5 data channel, provides better results. As it can be seen in Figure 4.13, L5-pilot channel tracking provides better jitter performance than the L5-data channel in both PLL and KF-based tracking methods. Furthermore, KF-based tracking provides improvement compared to the

PLL-tracking structure in terms of jitter performance in the case of both L5 and L1 C/A signals. However, it is expected that the GPS L5 signal, whose chipping rate is 10 times higher and its power is higher than L1 C/A, provides better results. As expected, tracking of L1 C/A signal experiences higher jitter compared to the L5 signal.

Chapter 5

Machine learning based methods to counteract GNSS impairments

AI refers to a broader term in the field of machine intelligence that comes up at the Dartmouth Summer Research Project on AI held at Dartmouth College in 1956 [151]. It refers to the idea that machines can execute the tasks smartly and the design of intelligent systems that perceive the environment and take actions. ML is a subset of AI as depicted in Figure 5.1.

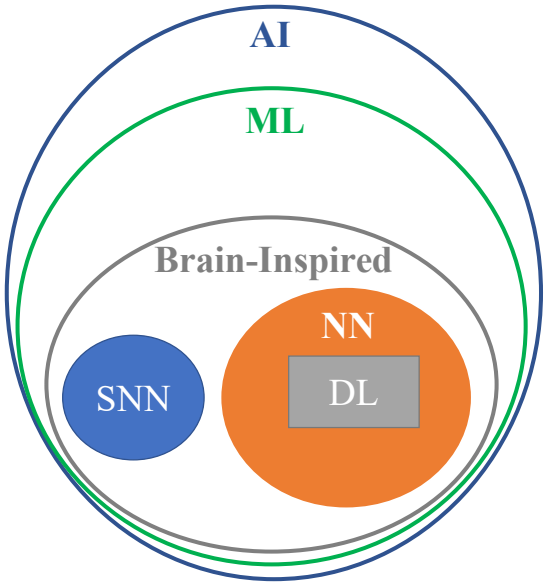

Figure 5.1: The taxonomy of Artificial Intelligence (AI) (adapted from [152]). ML: Machine Learning, NN: Neural Network, SNN: Spiking Neural Network, DL: Deep Learning.

ML automates the analytical model building by using the methods from such as Neural Networks (NNs), statistics, operations research, and physics, and it deals

with finding hidden insights in data without being explicitly programmed to where to look in the data [153]. ML is usually divided into two main types: predictive or supervised learning approach and descriptive or unsupervised learning approach [154]. In the supervised approach, the aim is to learn the mapping of inputs (x) to outputs (y) through a given labeled set of input-output pairs [154]:

$$D = \{(x_i, y_i)\}_{i=1}^{N} \tag{5.1}$$

where D is the training data set and N is the number of training examples. Each training input x_i is a d-dimensional vector of variables called features, attributes, or covariates. y_i is the output or the response variable. If y_i is real-valued, the problem is referred to as regression and when y_i is categorical the problem is known as classification, as depicted in Figure 5.2.

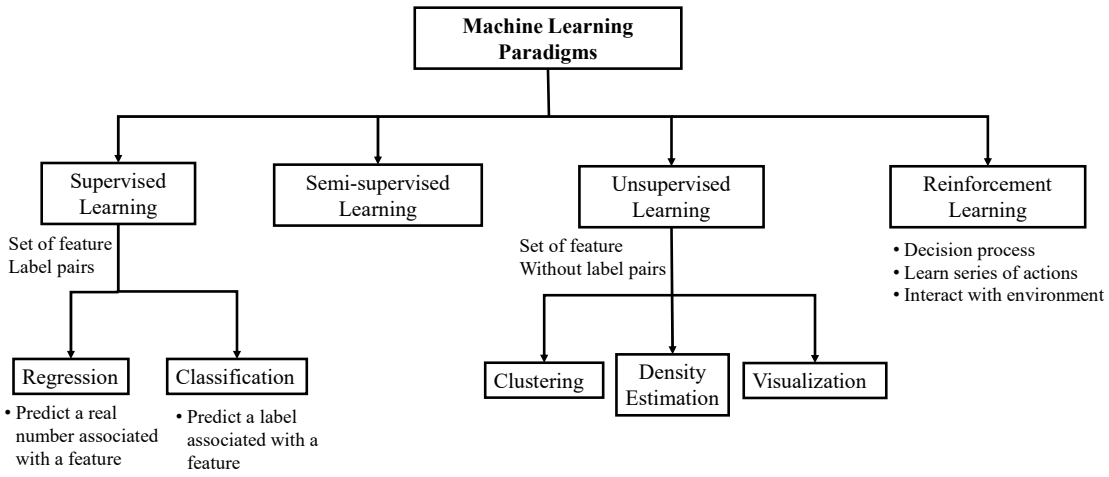

Figure 5.2: Machine Learning Paradigms.

In the descriptive or unsupervised learning approach, the aim is to find the pattern in the given inputs $D = \{x_i\}_{i=1}^{N}$. In density estimation of the unsupervised learning approach, the goal is to infer the properties of the probability density $p(x)$ [155]. In the characterization of the input values (x), density estimation methods might fail in high dimensions [155]. Hence, the dimensionality reduction method that is projecting the data to a lower-dimensional subspace is useful for visualizing high-dimensional data. The most commonly used approach is called Principal Component Analysis (PCA) [154]. Some other unsupervised learning algorithms perform dividing the data into groups of similar examples and it is referred to as clustering [156].

As depicted in Figure 5.2, semi-supervised learning approach falls between supervised learning and unsupervised learning. A combination of the labeled examples from $p(x, y)$ and unlabeled data from $p(x)$ are used to estimate $p(y|x)$ or predict y from x [156]. There is another type of machine learning named reinforcement

learning that is less commonly used and it is used for learning how to act with the existence of reward or punishment signals and a feedback loop between the learning system and experiences [154, 156].

Artificial Neural Networks (ANNs) are popular ML techniques inspired by the workings of human brain [153]. Likewise, human nervous system contains neurons and the ANNs contain computation units that are referred to neurons [157]. Spiking Neural Networks (SNNs) are inherently more biologically plausible considering the fact that neurons in the brain process binary spike-based information as a function of time; however, ANN inputs are static [158]. An NN has a particular nested function: [159]:

$$y = f_{NN}(x) = f_3\left(f_2\left(f_1(x)\right)\right) \tag{5.2}$$

where this 3-layer neural network returns a scalar y. The vector functions can be of the following form [159]:

$$f_i(x) \stackrel{\text{def}}{=} g_l\left(W_l z + b_l\right) \tag{5.3}$$

where l is layer index that can span from 1 to any number of layers. g_l is called activation function. The matrix W_l and vector b_l are learned for each layer depending on the applied task. For example, by breaking the desired complicated mapping problem into a series of simple mappings of which each is described by a different layer of the model, Deep Neural Network (DNN) learning (or, simply, Deep Learning (DL)) aims to solve complex problems.

In Figure 5.3, the flows of traditional ML and DL are shown. DL is also known as hierarchical learning that consists of multiple layers and feature extraction [160]. Every subsequent layer process the outputs of the previous layer as input (5.2) and the learning phase is not spanned on a single layer. Moreover, as depicted in Figure 5.3, while the features are learned automatically in DL implementations, ML approaches use feature extraction algorithms and then the learning algorithm is applied [152].

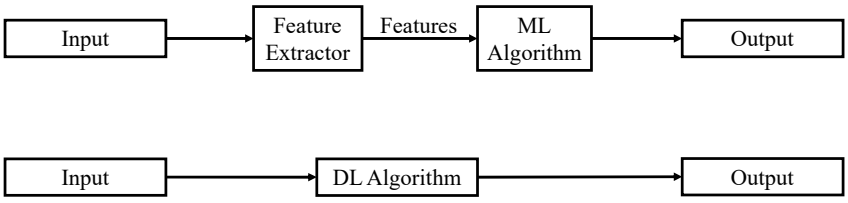

Figure 5.3: Machine Learning and Deep Learning flows (adapted from [160]).

In recent years, DL has gained huge success in a variety of applications through different methods of which some are listed in the Figure 5.4. A survey on DL theory and architectures is given in [152].

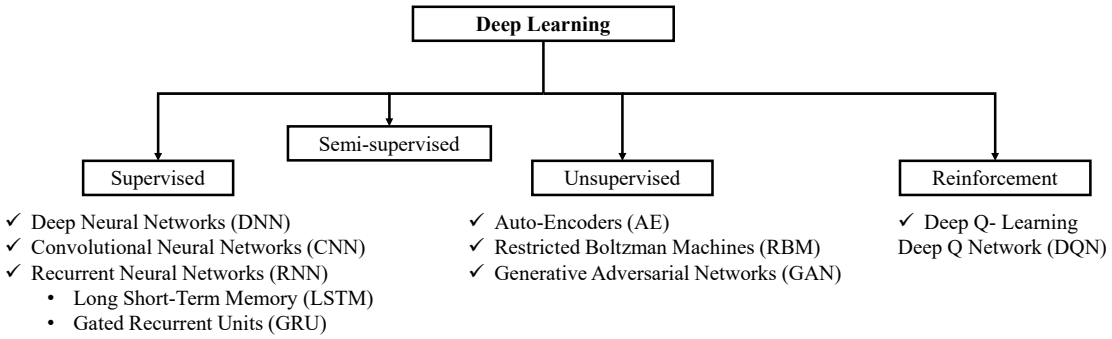

Figure 5.4: Common Deep Learning Approaches.

In this section, an overview summary of ML and DL approaches has been presented and more detailed information on theory and architectures can be found in several books [154, 155, 156, 157, 159].

5.1 Discussion on the role of ML for GNSS

With the innovative trend of SDR receivers that are flexible to implement new architectures, receiver implementations have been constantly evolving with the utilization of both ML and DL algorithms so as to alleviate the performance degradation effects of error sources such as scintillation and multipath. Scintillation and multipath detection methods in the literature are discussed in Sections 5.2.1 and 5.3.1, respectively. Furthermore, there have been possible scenarios and applications in which ML has been considered in the GNSS area.

Instead of implementing correlators and matched filters to detect noise-like signals, a NN approach including a layered architecture has been implemented and applied for radio signal detection in [161]. Moreover, DNNs that are a branch of DL algorithms have been a powerful tool achieving excellent performance on difficult problems such as speech recognition and visual object recognition [162]. A survey of implemented DL techniques for wireless signal recognition is provided in [163]. In another paper, DNN has been applied for automatic classification of different signal modulations with three hidden layers [164]. Furthermore, there are two main types of DNNs, namely, Convolutional Neural Network (CNN or ConvNet) and Recurrent Neural Network (RNN) [165]. While CNN is a hierarchical DNN including convolution and pooling layers, RNN is a sequential DNN with different memory structure. In [166], a CNN-based architecture for the modulated signal detection in the presence of noisy channel observations is proposed and the advantages over DNNs in which suffer from the curse of dimensionality are presented. Although, recently, in [167] a DL approach to GNSS signal acquisition by addressing a classification problem from CAF delay/Doppler maps has been proposed, in the literature the GNSS receiver side has not been fully studied yet; however, DL-based applications

have been highly investigated in the different implementations of communication engineering.

GNSS signals are vulnerable to intentional interference and spoofing attacks which have been becoming an increasing threat to, in particular, critical applications such as aviation. Therefore, detection, mitigation, and classification methods for GNSS interference and spoofing have been crucial. A survey on coping with intentional interference for manned and unmanned aircraft [168] covers both traditional and ML algorithms applied by the research community at different stages (e.g. front-end, pre- and post-correlation). For example, in [169], GNSS spoofing jamming recognition based on SVM classifier has been applied after applying several nonlinear dimensionality reduction and feature extraction algorithms such as classical ISOmetric MAPping (ISOMAP), Laplacian Eigen (LE) mapping , PCA, and Wavelet Transform - Singular Value Decomposition (WT-SVD). Likewise, in [170], monitoring the cross-correlation of multiple GNSS observables and measurements that are input for SVM algorithm to detect spoofing is realized. A better understanding of the relation between the selected variables and the indicator of spoofing-jamming attacks is considered as a prerequisite for the success of the algorithm. Moreover, a real-time interference monitoring technique has been applied by means of Twin Support Vector Machine (TWSVM) algorithm that is claimed to be faster than conventional SVM in [171]. Although ML algorithms seem promising, their performance and complexity on GNSS interference classifications have yet to be fully investigated and studied.

In a GNSS receiver, predictions of the satellite orbits are based on the physics-based models and broadcasted ephemeris. In order to improve the orbit prediction and reduce the required time to provide the first position estimate, supervised ML algorithms have started to be applied. In [172], besides the applied orbit prediction model, CNN algorithm is used to improve the performance of the mechanistic model. A generalized hybrid implementation approach that employs both SVM and physics-based model for Resilient Space Objects' (RSOs') orbit predictions are defined in [173]. In the same manner, another key parameter to be predicted along with satellite orbit prediction is the satellite clock offset. A comparison of implemented polynomial regression, Kalman filtering, and Least Squares Support Vector Machine (LSSVM) algorithms for predicting the clock offset of GPS and GLONASS satellites have been provided in [174].

Due to the fact that unpredictable variability of the ionospheric parameters due to space weather limits the efficiency of trans-ionospheric communication systems, forecasting TEC values is crucial for GNSS, as well [175]. There are various NN-based implementations to forecast ionospheric parameters where a summary of the approaches with prediction lead times and main features are provided in [176]. For example, while Nonlinear Autoregressive with External Input (NARX) network is applied for 24 h TEC forecasting in [176], a CNN-based architecture for image sequence (i.e. TEC maps) prediction is designed for a longer range forecasting up

to 48 h in [177].

RF Fingerprinting (RFF) is the process of gathering information about the radio transmitters by examining their electromagnetic wave characteristics and signatures to identify unique features that a device possesses [178, 179]. Mostly in wireless networks, it has been applied as a solution to reduce the vulnerability of the networks against security threats and attacks [178, 180] and for indoor positioning by using mainly Received Signal Strength (RSS) measurements [181]. ML algorithms also assist RFF in providing automatic identification of the unique aspects of the individual RF emitters [182]. Furthermore, so far in the GNSS area, fingerprinting approach has been investigated by selecting features for automatic receiver identification [179, 183]. In [183], the usage of clock-derived metrics for GNSS receiver fingerprinting by means of the application of Gaussian Naïve Bayes Classifier (NBC) is investigated for security-enhanced applications. For urban positioning problems, the shadow-matching technique (i.e. a type of pattern-matching positioning) for smartphone-based positioning using 3D city models is proposed in [184]. In [184], a modified k-Nearest Neighbors (kNN) is applied to estimate the location averaging the grid positions with the highest satellite visibility scores. For spoofing detection, after applying a feature extraction algorithm that is based on Axial Integrated Wigner Bispectrum (AIWB) of the received GNSS signal, SVM is used in [185]. Furthermore, in [186], with a summary of the RFF approaches in the literature, SVM- and CNN-based classifications processing different frequency transforms (e.g. wavelet, spectrogram) of the received GNSS signals are investigated through a controlled simulation environment.

In this section, a summary of possible ML implementations considered in the literature has been provided. With the increasing interests and needs day by day, researches on ML-based applications have been very active in the GNSS area.

5.2 Scintillation detection

5.2.1 Scintillation detection methods

One of the proposed methods is based on a SVM algorithm [187] that belongs to the class of supervised machine learning algorithms [188]. Supervised algorithms require large data sets to properly train the algorithm so that it is able to recognize the scintillation presence during the analysis of new measurements. In [6], another type of supervised learning algorithm, namely, the decision tree, is applied to enable early scintillation alerts. In [189], the performance of SVM implementations for phase and amplitude scintillation detection have been evaluated. The main weakness of these works is that the impact of the design parameters of the different algorithms on the achieved performance has not been carefully analyzed in detail as witnessed by the limited literature addressing the application of machine learning

to GNSS. Since the success of the SVM algorithm can be attributed to the joint use of a robust classification procedure and of a versatile way of pre-processing the data, the parameters of the machine learning phase must be carefully chosen [190].

SVM algorithm is the most widely used kernel learning algorithm [187]. Kernel method enables the SVM algorithm to find a hyperplane in the kernel space by mapping the data from the feature space into higher dimensional kernel space and leading to achievement of non-linear separation in the kernel space [191]. Kernel representations offer an alternative solution to increase the computational power of the linear learning machines [192]. In SVM implementations, the kernel functions are linear, Gaussian Radial Basis Function (RBF), and polynomial are widely used. Hence, the problem of choosing an architecture for an ML-based application is equivalent to the problem of choosing a suitable kernel for an SVM implementation [192]. Moreover, when training an SVM algorithm, besides choosing a suitable kernel function a number of decisions should also be made in the preparation of the data, by labeling them, and setting the parameters of the SVM [193]. Otherwise, uninformed choices might result in degraded performance [194].

In this thesis study, linear and Gaussian kernels, the implementation of different order polynomial kernels, and the performance comparison on the cross-validation results are the original core of the study. The impact of the kernel function on the scintillation detection performance by considering the related design parameters (e.g. scale parameter, polynomial order) is discussed. Performance is assessed by exploiting the ROC curves, confusion matrix results and the related performance metrics. This study is performed using real GNSS signals that are affected by significant phase and amplitude scintillation effect, collected at SANAE IV and Hanoi.

5.2.2 Overview of Support Vector Machines (SVM) method

An SVM algorithm classifies the data by finding the best hyper-plane that separates all the data of one class from those of the other class [195]. Figure 5.5 shows a pictorial example of two data sets that can be separable into two classes. However, as it can be seen in Figure 5.5 (a) that there could be an infinite number of separating hyper-planes. The classes can be separated by the linear boundaries as well as non-linear boundaries. SVM approaches to this problem through the concept of the smallest distance between the decision boundary and any of the data samples [196]. In Figure 5.5 (b), as an example of linear classifiers, the best hyper-plane that corresponds to the one providing the largest margin between the classes is depicted. The margin is the maximum width of the slice, parallel to the hyper-plane, that has no data samples within [195]. The data samples that are closest to the separating hyper-plane are called support vectors as shown in Figure 5.5 (b).

In SVM linear classification, the idea is to take the projection of an unknown

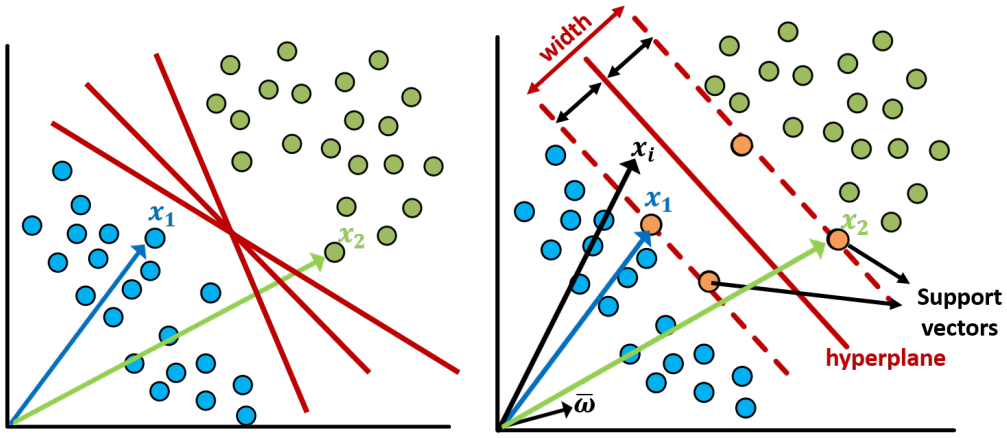

(a) Separating hyper-planes. (b) Best hyper-plane.

Figure 5.5: An overview sketch of Support Vector Machines (SVM) algorithm linear classifier.

vector x_i along vector $\bar{\omega}$, which has to be perpendicular to the decision boundary medium (e.g. it has to be in the third dimension if the decision boundary is spanned in two dimensions), and to check whether it crosses the boundary or not in order to decide the classification. The implementation starts with the derivation of the optimal hyper-plane of SVM. The derivation of the optimum hyper-plane is given in Appendix B.1.

The decision function of SVM is computed as:

$$\hat{y}(x_i) = \text{sign}\left(\sum_{j=1}^{N_s}[\hat{a}_i t_i \kappa(x_j, x_i)] + b_0\right) \tag{5.4}$$

where $\{x_1, x_2, ..., x_N\}$ is the input data-set. Corresponding target values $\{t_1, t_2, ..., t_N\}$ to the input values are decided according to y_i and b_0 is the parameter of the optimum hyperplane. $\hat{a}$ is the set of Lagrange multiplier used to compute the optimal parameters of the hyperplane and κ is the kernel function.

Kernel Extension

A kernel is a function κ that for all $x, y \in X$ satisfies [197]

$$\kappa(x, y) = \langle \phi(x), \phi(y) \rangle \tag{5.5}$$

where ϕ is a mapping from X to F_κ that is an inner product feature space associated with the kernel κ:

$$\phi : x \in X \rightarrow \phi(x) = \kappa(x, \cdot) \in F_\kappa \tag{5.6}$$

Any finite subset of the space X are positive semi-definite and the kernel function satisfies positive semi-definite condition as mentioned. Actually, corresponding space F_κ is referred as Reproducing Kernel Hilbert Space (RKHS), which is a Hilbert space containing Cauchy sequence limit condition [197]. Theory of reproducing kernels were published by Aronszajn in 1950, and detailed theory can be found in [198]. Moreover, the kernel concept was introduced into the pattern recognition field by Aizerman in 1964 [196].

In most cases, the samples may not be linearly separable. The linear kernel can be expressed as

$$\kappa(x_i, x_j) = x_i^T x_j \tag{5.7}$$

If the classification problem is not linearly separable, SVM can be powered up by a proper kernel function. Kernel method enables SVM to find a hyperplane in the kernel space and hence non-linear separation can be achieved in that feature space [191].

An example of non-linear kernels is Gaussian RBF, which can be written as

$$\begin{aligned} \kappa(x_i, x_j) &= \exp\left(-\frac{\|x_i - x_j\|^2}{2\sigma^2}\right) \\ &= \exp\left(-\gamma \|x_i - x_j\|^2\right) \end{aligned} \tag{5.8}$$

where σ defines the width of the kernel. If the parameter σ is close to zero, SVM tends to over-fitting which means all the training instances are used as support vectors [191]. Assigning a bigger value to σ may cause under-fitting leading all the instances to be classified into one class. Therefore, a proper value must be selected for the kernel width. In the same manner, kernel scale parameter corresponds to γ parameter in the RBF definition as being different from the σ representation.

Another most commonly used kernel function is the polynomial that can be represented as

$$\kappa(x_i, x_j) = \left(1 + x_i^T x_j\right)^p \tag{5.9}$$

where p is the order of the polynomial kernel. The lowest degree polynomial corresponds to the linear kernel and it is not preferred in case of having nonlinear relationship between the features. The degree of the polynomial kernel controls the flexibility of the classifier and higher-degree allows a more flexible decision boundary compared to linear boundaries [199].

The performance of linear, Gaussian and polynomial kernels are compared in the implementation in the next section.

5.2.3 Training Data Preparation and Labeling

Some of the scintillated data sets that are collected via Fourtune and analyzed are summarized in Table 5.1. Scintillation monitoring and data collection setup is given in Figure 3.4. PRN codes are ranging code components of the transmitted satellite signals and are unique for each satellite signal. In Table 5.1, they refer to the satellites from which the scintillation effect observed in the received signals.

Table 5.1: Specifications of the Analyzed Scintillated Data Sets

	Dates	PRNs	Station	Coordinates
1	Jan 21, 2016 Feb 3, 2016 Feb 8, 2016 Aug 17, 2016	$11-14-22$ $3-6$ $1-12-14$ 9	South African Antarctic Research Base (SANAE-IV), Antarctic	Lat.: 71.67°S Long.: 2.84°W
2	April 10, 2013 April 12, 2013 April 16, 2013 October 4, 2013	11 17 $01-20-28$ $15-21-24$	Hanoi, Vietnam	Lat.: 21.00°N Long.: 105.84°E

The preparation of the data is the most important step in the machine-learning implementations. Amplitude and phase scintillation indices have to be put into a format so that the SVM algorithm can detect the scintillation in the correct way. As it is mentioned, it is difficult to model the occurrence of scintillation due to temporal and spatial variabilities of the ionosphere [71]. Statistical analysis has been highly benefited and also chosen fixed period (T) for the computations of S_4 and σ_ϕ indices is quite important given in (3.9) and (3.3). Generally, T is adjusted to 60 seconds in ISMR receivers. In this case, by considering only one value to feed the algorithm, early detection of the scintillation seems not to be possible. Moreover, according to performed analysis of high-latitude and equatorial ionospheric scintillation events in [71], phase scintillation lasts around 5.6 minutes at high latitude regions and 10.2 minutes in the equatorial region. On the other hand, it has been observed that amplitude scintillation events last around 3.1 minutes at the high-latitude region and 12.4 minutes in the equatorial region. Therefore, so as to enable early scintillation detection, the training data is put into a format by partitioning the data into 3 minutes blocks via a moving time window.

In this work, only two class labels, namely, scintillation and no-scintillation are assigned as follows:

$$class(x_i) = \begin{cases} C_1 & \{\text{Scintillation}\} \quad , t_i = 1 \, (\sigma_\phi \geq 0.3 \text{ or } S_4 \geq 0.4) \\ C_2 & \{\text{No-Scintillation}\} \quad , t_i = 0 \, (\sigma_\phi < 0.3 \text{ or } S_4 < 0.4) \end{cases} \tag{5.10}$$

The class definitions in (5.10) have been decided according to the limit values of σ_ϕ and S_4 indices given in [201, 200] that are observed in high-latitude and equatorial

scintillation events. The list of the training data segments is reported in Table 5.1. The data collected on different days at SANAE IV and Hanoi stations are put in the defined structure and labeled according to the class definition above. Figure 5.6 (a)-(b) shows an example of labeling for both amplitude and phase scintillation data-sets.

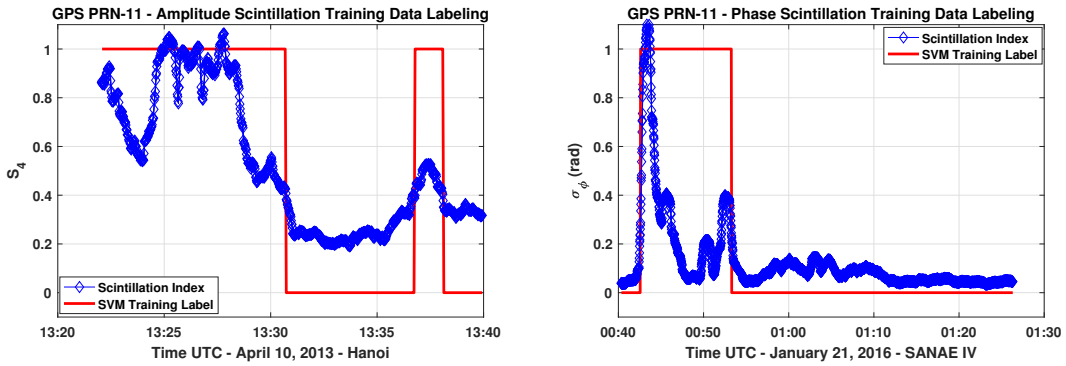

(a) Amplitude Scintillation. (b) Phase Scintillation.

Figure 5.6: Labeling of the amplitude and phase scintillation index values in the training data sets.

In Figure 5.6 (a), S_4 indices computed from the received GPS L1 signal broadcast from the satellite PRN-11 are plotted. It belongs to the data collected on April 10, 2013 in Hanoi. The figure indicates that amplitude scintillation events occurred starting around 1:20 p.m.

Another event which is observed in the data collected on January 21, 2016 at the Antarctic station SANAE IV is analyzed and the computed σ_ϕ indices are plotted in Figure 5.6 (b). The figure shows the phase scintillation event occurred starting from 12:40 a.m. as denoted by the sharp increase in the indices. Although the σ_ϕ values go to values lower than 0.3 around 12:50 a.m., such a time interval is still considered to be part of the scintillation event and then accordingly labeled as. In fact, the data portion between the consecutive scintillation events is anyway affected by a residual scintillation effect that can be observed in the receiver tracking outputs and GNSS measurement observables. Therefore, labeling has been done manually, by inspection, for all the training data sets.

5.2.4 Experimental Tests

In this section, the implementation and performance analysis of the scintillation detection based on the SVM method that exploits different kernel functions are provided through the collected data.

Cross Validation

After class labels are assigned to the data-sets for amplitude and phase scintillation events, SVM methods with different kernel functions are trained. In this section, the performance of validation of the methods is evaluated in terms of ROC curves.

As it has been already discussed in Section 4.1.1 for the performance comparison of different signal acquisition methods, the ROC curve, which has been widely used in signal detection theory, is a plot of the probability of detection (P_D) versus the probability of false alarm (P_{FA}). Furthermore, in recent years, it has been increasingly used for binary classification problems in ML with the corresponding different metrics as well.

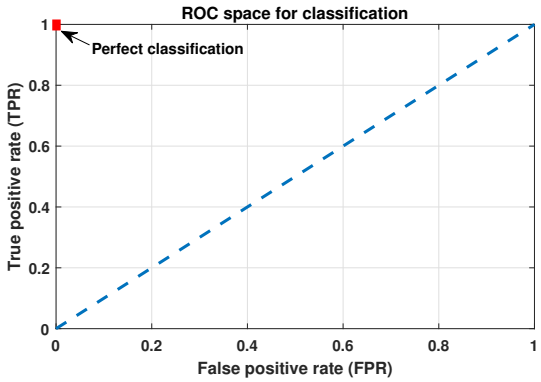

Figure 5.7: An example of Receiver Operating Characteristics (ROC) space for classification evaluation.

Figure 5.7 shows an example of the ROC graph. It is a two-dimensional plot of a classifier indexed in one dimension by the False Positive Rate (FPR) and in the other by the True Positive Rate (TPR). A ROC graph depicts relative trade-offs which a classifier makes between benefits (true positives) and costs (false positives) [202]. TPR (i.e. sensitivity) and the True Negative Rate (TNR) (i.e. specificity) are the terms which split the predictive performance of the classifier into the proportion of positives and negatives correctly classified, respectively.

In ROC space, the point (0,1) represents the perfect classification as shown in Figure 5.7. The dashed diagonal line represents the case of random assignment of an element to a class. If one point is closer to the upper left corner (i.e. higher TPR, lower FPR), its classification performance is better than another. Classifiers appearing on the left side of the ROC space are named as conservative such that they make classification with strong evidence so they have small FPR, but they generally have low TPR [203]. On the other hand, the classifiers on the right side of the ROC space are thought as liberal. They make classifications with low evidence so they classify all the positives correctly with a drawback of high FPR.

Each point on the ROC curve represents a trade-off, in other words, a cost ratio [204]. Cost ratio is equal to the slope of the line tangent to the ROC curve at a given point.

SVM implementation for both phase and amplitude scintillation detection has been done by employing MATLAB's statistics and machine learning toolbox [205]. In order to evaluate the performance of the implemented SVM methods, 10-fold cross-validation technique has been applied. In this technique, the partitions are put into 10 randomly chosen subsets of equal size. Then, each subset is used to validate the model by using the trained remaining 9 subsets. This process is repeated 10 times so that each subset is used once for the validation.

Figure 5.8 (a) and (b) show the ROC curves of SVM methods with different kernel functions for amplitude and phase scintillation, respectively. In general, it shows that in amplitude scintillation case the performance of the SVM methods is better than the phase scintillation case. However, due to the fact SVM performance depends on the data-sets, each scintillation case is evaluated separately and the performance of the kernel functions under the same conditions is compared.

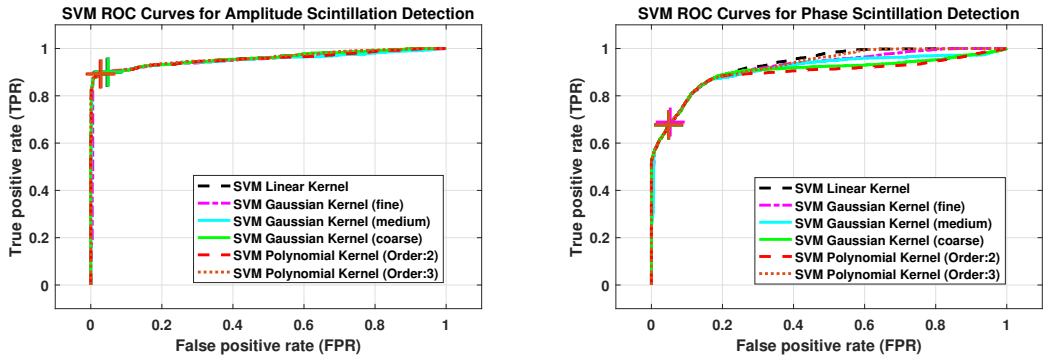

(a) Amplitude Scintillation. (b) Phase Scintillation.

Figure 5.8: ROC curves of SVM methods with different kernel functions.

In the analysis, Gaussian RBF kernel scale parameter γ in (5.8) is adjusted to different values according to following assumptions [206]:

$$\begin{aligned} \gamma_{fG} &= \sqrt{n/4}, \text{ for fine Gaussian} \\ \gamma_{mG} &= \sqrt{n}, \text{ for medium Gaussian} \\ \gamma_{cG} &= 4\sqrt{n}, \text{ for coarse Gaussian.} \end{aligned} \tag{5.11}$$

where n is the number of features or the dimension size of x_i in (5.4). Moreover, second and third-order polynomial kernels are included in the analysis. The different colored plus symbols on the figures indicate the operating points of each method in Figure 5.8. Since the ROC curves are close to each other and it is not easy to

differentiate the differences between each method, the results are summarized in Table 5.2 and Table 5.3.

Table 5.2: Phase scintillation detection performance comparison in terms of complexity, True Positive Rate (TPR), False Positive Rate (FPR), and Area Under Curve (AUC) under 10-fold cross-validation test.

SVM Method	**Kernel Scale**	**Running Time**	**Validation Accuracy (%)**	**Operating Point**		**AUC** (%)
				TPR	**FPR**	
Linear	1	t_p	86.01	0.6772	0.0468	91.98
Coarse Gaussian	6.9	$1.28t_p$	86.29	0.6755	0.0482	90.10
Medium Gaussian	1.7	$1.55t_p$	86.16	0.6751	0.0480	90.85
Fine Gaussian	0.43	$1.70t_p$	85.95	0.6890	0.0530	93.16
Polynomial (Order:2)	1	$1.37t_p$	86.26	0.6768	0.0485	89.38
Polynomial (Order:3)	1	$3.20t_p$	86.04	0.6779	0.0488	92.67

In Table 5.2 and 5.3, the time complexity values which are dedicated time to both training and testing are compared. The complexity of a classifier is divided into two kinds of complexity, namely, time complexity and space complexity [207]. While time complexity deals with the time spent on the execution of the algorithm, space complexity considers the amount of memory used by the algorithm [207]. For example, run-time complexity of linear and RBF kernels differ from each other. While the complexity of the RBF kernel is shown to be $\mathrm{O}\left(n_{SV} \times d\right)$, which is dependent on the number of support vectors (n_{SV}) and the input dimension (d), linear method has $\mathrm{O}\left(d\right)$ prediction complexity [208]. Therefore, as it is seen in both Table 5.2 and 5.3, running time increases in the cases of the kernel functions in which the samples are uplifted into higher dimensions and it also becomes dependent on the number of samples.

Table 5.3: Amplitude scintillation detection performance comparison in terms of complexity, True Positive Rate (TPR), False Positive Rate (FPR), and Area Under Curve (AUC) under 10-fold cross-validation test.

SVM Method	**Kernel Scale**	**Running Time**	**Validation Accuracy (%)**	**Operating Point**		**AUC** (%)
				TPR	**FPR**	
Linear	1	t_a	90.44	0.8990	0.0460	95.37
Coarse Gaussian	6.9	$1.02t_a$	90.72	0.9004	0.0487	95.18
Medium Gaussian	1.7	$1.18t_a$	91.65	0.9004	0.0487	95.19
Fine Gaussian	0.43	$1.33t_a$	91.56	0.9018	0.0378	96.01
Polynomial (Order:2)	1	$1.08t_a$	91.42	0.8920	0.0265	95.61
Polynomial (Order:3)	1	$1.80t_a$	91.56	0.8927	0.0292	95.88

The parameter, Area Under Curve (AUC), represents the estimated area under the ROC curve and it is used as a performance measure for the machine learning

algorithms [209]. AUC is accepted as an indicator for the overall accuracy of the classifier, both Table 5.2 and 5.3 show the importance of kernel scale parameter. While the overall accuracy of coarse and medium Gaussian kernel SVM methods are less than the linear SVM, fine Gaussian SVM outperforms the linear. Moreover, the third-order polynomial kernel provides improved performance compared to linear, coarse and medium Gaussian kernel SVMs, but it comes with a cost of increased complexity and time.

Tests and Evaluation

In this section, as a performance cross-check, the collected data which are not included in the training sets are also used to evaluate the performance of scintillation detection methods. Figure 5.9 (a,b) show the decisions of the different kernel SVM methods for the data sets for both amplitude and phase scintillation.

In order to evaluate the performance comparison, the confusion matrix technique, which is a two-dimensional matrix indexed in one dimension by the true class of an object and in the other by the class that the classifier assigns [210] as it is seen in Table 5.4, is applied. A confusion matrix represents the dispositions of a set of instances (i.e., test data) according to a defined classification model that maps the set of instances to predicted classes [203]. Actually, each different point in a ROC curve corresponds to a confusion matrix.

In the two-class data classification problem, the four cells of the confusion matrix correspond to the values of true positives (TP), false positives (FP), true negatives (TN), and false negatives (FN). By considering the numbers of the measures, this matrix forms the basis for the terms, namely, accuracy, precision, sensitivity, specificity, and error rate. Accuracy is the ratio of the correct predictions (i.e., the sum of true positives and true negatives) to the total predictions made by the classifier. In the same sense, the error rate is the ratio of the incorrectly classified objects to the total objects. In Table 5.5, the performance of different kernels for the data sets in terms of accuracy and error rate are summarized.

Table 5.4: Confusion matrix.

CONFUSION MATRIX		ACTUAL	
		Scintillation	No-Scintillation
PREDICTION	Scintillation	True Positive (TP)	False Positive (FP)
	No-Scintillation	False Negative (FN)	True Negative (TN)

As it is expected, the results in Table 5.5 are consistent with the cross-validation results. With the correct setting of the kernel scale parameter, the fine Gaussian SVM method outperforms in terms of accuracy rate. Furthermore, although the differences in the accuracy of the methods seem not to be at a considerable level,

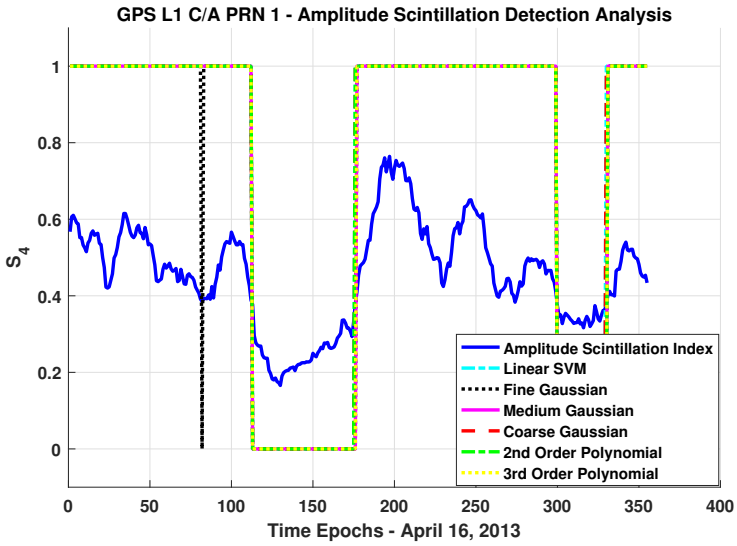

(a) Amplitude scintillation detection.

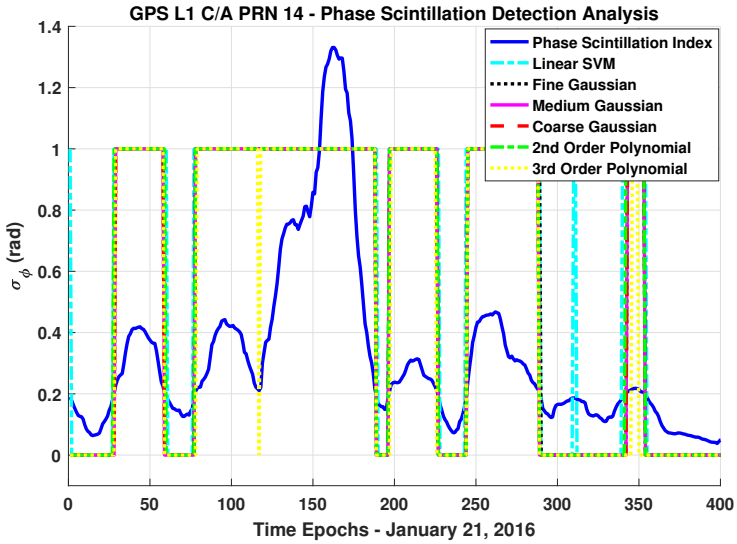

(b) Phase scintillation detection.

Figure 5.9: Scintillation detection results based on Support Vector Machines (SVM) with different kernel functions. "1" corresponds to the points in which the related method points out the scintillation event and "0" means no-scintillation event is detected. Both amplitude and phase scintillation indices synchronized in time can be evaluated as ground truth in the graph to evaluate the performances of different kernels.

in terms of early detection, the method that provides higher accuracy gains importance. For example, in the cases of the computation rate of the scintillation indices

being around one minute, the method having a higher accuracy rate will provide quite advantageous conditions in terms of early detection. However, the third order polynomial kernel provides an improvement in the accuracy compared to the linear kernel, but its performance should be evaluated with increased time and space complexity.

Table 5.5: Accuracy and error rate performances of different kernel SVMs for scintillation detection

	Phase Scintillation		**Amplitude Scintillation**	
	Accuracy	**Error Rate**	**Accuracy**	**Error Rate**
Linear	90.98%	9.02%	94.46%	5.54%
Coarse Gaussian	92.61%	7.39%	94.18%	5.82%
Medium Gaussian	92.61%	7.39%	94.18%	5.82%
Fine Gaussian	92.50%	7.50%	95.02%	4.98%
Polynomial (Order:2)	92.28%	7.72%	94.46%	5.54%
Polynomial (Order:3)	93.59%	6.41%	94.74%	5.26%

To sum up, through this research work selecting a suitable kernel function in SVM-based scintillation detection has been mainly questioned. However, considering obtained validation accuracies, the addition of different possible features (e.g. tracking stage correlator outputs, signal intensity measurement, etc.) and extension of training datasets could be studied to improve the performance and consolidate the work.

Furthermore, it has to be also noted that the SVM approach that is well-founded on maximum margin-based classification offers one of the most robust and accurate solutions in today's ML applications [211]. By the way, the main disadvantage of the algorithm is computational inefficiency that can be encountered in the case of finding maximum margin hyperplanes to a large number of instances (e.g. thousands and millions) at once. Thus, breaking this large optimization problem into smaller problems and working on subset (i.e. core) sets have been shown to provide a good and fast approximation for SVM learning in [212]. In this implementation, it has been decided that the dataset size is not at that level by considering the dedicated durations spent on both training and test.

In the literature, quantitative measures, in other words, classification performance metrics such as TPR, FPR, AUC, etc., have been widely exploited for performance assessment of training dataset selection [213]. An example combined quality function used for training set selection by maximizing the classification accuracy and decreasing the execution time that is in parallel to minimizing the

number of support vectors is

$$Q(\mathrm{AUC}, n_{SV}) = q\,\frac{\mathrm{AUC}}{\mathrm{AUC}^{B}} + (1-q)\,\frac{n_{SV}^{B}}{n_{SV}} \tag{5.12}$$

where n_{SV}^{B} is the lowest number of support vectors and AUC^{B} is the largest AUC obtained across the investigated test sets [213]. q is denoted for the importance of the objective and resides between 0 and 1. The largest Q value indicates the best training data set. However, in this implementation, depending on the availability of the scintillated dataset, training datasets are processed, and the attained overall accuracy are evaluated after design and implementation for parameter tuning. The AUC in (5.12) can be replaced by any other metrics for performance evaluation as well.

5.3 Multipath detection

5.3.1 Multipath detection methods

Different ML algorithms started to be applied for the multipath detection and inconsistency check of the measuremens. In [214], the author proposed a classifier based on the SVM method, which is a supervised ML algorithm, by training a large amount of collected GNSS data to distinguish clean, multipath, and NLOS measurements. In a similar way, an ML algorithm characterizing the measurement quality and detecting the multipath is proposed in [215]. Multipath error estimation is considered as a regression problem and epsilon-insensitive Support Vector Regression ($\varepsilon-$SVR) method is employed to estimate the multipath error at most ϵ deviation from the actual target for all training data in [216, 118]. Moreover, CNN utilizing deep neural networks to span the feature learning on multiple layers has been applied recently for multipath detection in the GNSS receiver [217, 218]. While the pseudorange and carrier phase observations are utilized in [217], the correlator outputs at the signal processing level are trained through the CNN algorithm in [218]. Furthermore, an RNN-based NLOS classifier that discriminates LOS and NLOS satellites implemented in [219] has been claimed to have 20 % better discrimination performance has been claimed in comparison to the conventional SVM-based NLOS classifier. However, in the aforementioned ML implementations, the algorithms are trained with the collected multipath-affected and clean data sets so that the algorithm learns the features of multipath thanks to the labeling, and then it could be able to recognize the multipath presence during the analysis phase of the new measurements. As expected, the supervised algorithms require considerable large data sets in order to properly train the algorithm due to a large variety of stations and scenarios that might be classified as a GNSS multipath event.

In this thesis study, a new approach for multipath detection based on unsupervised machine learning algorithms in a GNSS receiver has been proposed. In this

research, the preliminary results of K-means clustering implementation [12] have been extended to a comprehensive analysis, and the Self-Organizing Map (SOM) based multipath detection algorithm has been included. The scope of this approach is multi-fold:

- A post-receiver technique that utilizes common GNSS stand-alone receiver observables, namely, carrier phase, pseudorange, and signal carrier-to-noise ratio is applied. The algorithm processes the measurement sets computed for each satellite. Since the algorithm works at the measurement level, it can be applied widely in GNSS applications exploiting commercial GNSS receivers and it is flexible to modifications that might be required.
- The implemented ML algorithms belong to the class of unsupervised ML algorithms; therefore, the limitation of the availability of training data sets a-priori obtained and required as representative of multipath and no-multipath conditions has been overcome.
- Unsupervised learning in ML has sufficient flexibility to be used in a kinematic environment where the boundary conditions change over time.
- A robust algorithm that is not sensitive to the percentage of erroneous measurements and is able to sustain clustering in case of having a higher percentage of erroneous measurements has been targeted.

5.3.2 Overview of K-means and Self-Organizing Method (SOM)

In this section, an overview of clustering and a brief description of the K-means and SOM algorithms are provided.

Clustering

A cluster is a collection of the data items, which are similar between them and are dissimilar to the data items in other clusters, and clustering means partitioning a set set into set of clusters [220]. Figure 5.10 depicts an example of clustering a two-dimensional data set consisting of N samples into five clusters.

Clustering can be realized through two different approaches, namely, hierarchical and partitive [220]. The hierarchical approach can also be divided into methods such as agglomerative and divisive algorithms that correspond to bottom-up and top-down strategies aiming to build a hierarchy of clusters, respectively. However, partitive clustering targets partitioning the data simultaneously without forming a hierarchical structure [221]. Partitive clustering is preferred and used more frequently than other clustering algorithms due to the fact that it is not dependent

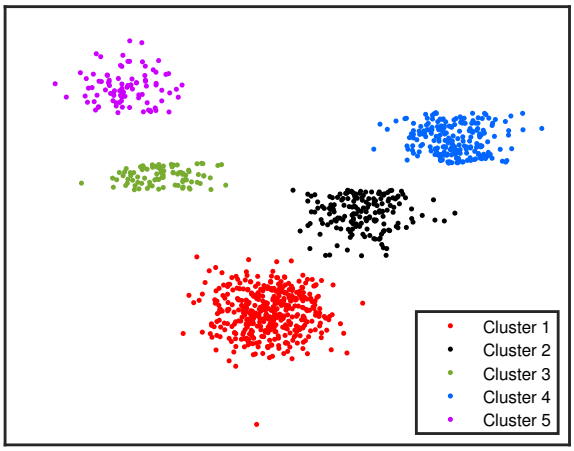

Figure 5.10: Clustering of N-samples data in 2D space.

on previously founded clusters and partitive methods make implicit assumptions on the representation of the data that can be represented by prototypes and hence clusters [220, 221]. In partitive clustering, it is supposed that the data can be represented by a set of prototypes, and hence it is also called prototype-based clustering. Moreover, it can further be classified into two groups: point-prototype-based clustering and prototype-based clustering [221]. One of the well-known and most used point-prototype-based clustering methods in the literature is K-means clustering that assumes each cluster is represented by a point in the feature space [221]. SOM is a type of ANN proposed by Kohonen [222] and known as a clustering tool, too. SOM performs vector quantization to divide an input space of n-dimensional data vectors into a reduced subset of prototype vectors organized in a regular grid [223] as depicted in Figure 5.11. Then clustering of the prototypes is realized instead of directly clustering the data.

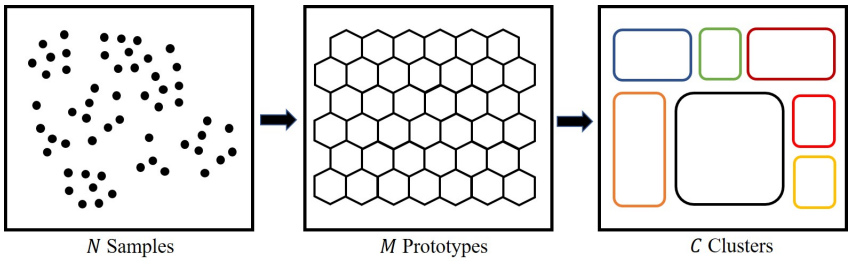

Figure 5.11: SOM Prototype-Based Clustering in 2D space.

In the following subsections, an overview of K-means and SOM algorithms is provided.

K-means Clustering

In K-means algorithm, the data is divided into k clusters and each cluster has a center that is called centroid. The number of clusters (k) is decided in advance. The implementation of the algorithm can be summarized by starting with the definitions of the data set [196]:

$$\begin{aligned} X &= \{x_1, x_2, \ldots, x_N\} \\ x_i &= (a_{i1}, a_{i2}, \ldots, a_{i\mu}) \end{aligned} \tag{5.13}$$

where X is the set of data points, N is the number of observations, x_i is a vector in X, and μ is the dimension of the data set. Initially, k points are randomly chosen as the initial centroids and the points that are closest to the centroid are assigned to the related cluster. Cluster set is written as follows:

$$C = \{C_1, C_2, \ldots, x_k\} \tag{5.14}$$

where C_j is the j^{th} cluster and the centroid of the cluster is defined as $m_j = (m_{j1}, m_{j2}, \ldots, m_{j\mu})$.

A score is assigned to each data point by considering its distance to the centroid the cluster. The objective function (J) is defined by computing the sum of squares of the distances of each data point to its assigned cluster centroid [12]:

$$\begin{aligned} J &= \sum_{j=1}^{k} \sum_{x \in C_j} d\left(x, m_j\right)^2 \\ d\left(x_i, m_j\right) &= \sqrt{\sum_{l=1}^{\mu} \left(x_i^{(l)} - m_j^{(l)}\right)^2} \end{aligned} \tag{5.15}$$

where $d\left(x, m_j\right)$ is the Euclidean distance between the data points (x) and the centroid. The aim is to minimize J by finding the correct separation and it is implemented through a two-step iterative procedure [196]. After having chosen the initial values for the m_j, in the first phase minimizing J is aimed with respect to the data points when m_j is fixed. In the second phase, by keeping the data points in the clusters are fixed, minimizing J is targeted by re-computing the m_j points. This two-stage optimization is repeated until convergence or up to predefined iteration value (t).

If each data points are assigned to a single cluster, it is called hard clustering that is not applicable for complex data sets containing overlapping clusters. The important aspects of the K-means algorithm are that its speed of convergence is high and little storage space is required [221]. Its complexity is denoted as $\mathrm{O}(n\mu kt)$ where n is the number of data points in X referred above.

SOM Prototype-Based Clustering

SOM is a prototype based clustering algorithm and it was proposed by Kohonen [222] as a data visualization technique that reduces the dimensionality of the data [221]. SOM forms an "elastic surface" that folds onto the "cloud" fitted to the input data [220, 222]. Prototype vector p represents the each unit i

$$\boldsymbol{p_i} = [p_{i1}, \ldots, p_{i\mu}] \tag{5.16}$$

where μ is the input vector dimension. SOM is trained iteratively and in each step, one vector from the input data set X is chosen randomly to compute the distances between x and prototype vectors p (i.e. weight vectors representing neurons) of the SOM. The best-matching unit (BMU) denoted as p_b is the closest neuron or map unit with prototype vector closest to x: [220, 224]

$$\|x - p_b\| = \min_i \{\|x - p_i\|\} \tag{5.17}$$

where $\|.\|$ denotes Euclidean distance. After finding the BMU, the prototype vectors are updated so that the BMU is moved towards the input sample in the input space. The update rule of the prototype vector of the unit i is:

$$p_i(t+1) = p_i(t) + \alpha(t) h_{bi}(t) \left[x(t) - p_i(t)\right] \tag{5.18}$$

where t is time, $\alpha(t)$ is the adaptation coefficient or learning rate factor with $0 < \alpha(t) < 1$, and h_{bi} is the neighborhood kernel centered on the winner unit. h_{bi} defines the region of influence that the input sample has and widely applied neighborhood kernel is the Gaussian function [222]:

$$h_{bi}(t) = \exp\left(-\frac{\|r_b - r_i\|^2}{2\sigma^2(t)}\right) \tag{5.19}$$

where σ defines the width of the kernel (i.e. neighborhood radius). r_b and r_i are the positions of the neurons b and i on SOM grid map. Both $\alpha(t)$ and $\sigma(t)$ are monotonically decreasing functions of time. In training, at first, relatively large initial learning rate and radius are used to adjust SOM approximately to the same space of the input data, then the values are decreased for the fine-tuning of the map [224].

In SOM algorithm computational complexity increases linearly with the number of data samples [220]. In the case of clustering N samples through K-means by means of M prototypes, the total complexity is proportional to $NM + \sum_k^{k_{max}} Mk$. For example, when the number of clusters k_{max} is set to $\sqrt{N}$ and $M = 5\sqrt{N}$, the reduction of the computational load is about $\sqrt{N}/15$ compared to clustering the data directly [220]. Therefore, using a set of prototypes as an intermediate step provides a reduction in the total complexity of the clustering.

After briefly describing K-means and SOM algorithms, their application to multipath detection is defined in the following section.

5.3.3 Implementation of Multipath Detection Algorithm

The implementation flow chart of the algorithm realized and evaluated in this study is shown in Figure 5.12. After the GNSS measurements are put into a format in the data preparation part, two different implementations are carried out as shown in two cases in Figure 5.12. In Case-2, as depicted in Figure 5.11, the SOM output space consists of a regular, and usually two-dimensional, grid of map units. This is the input for the clustering procedure differently from Case-1 where the data are directly fed to the clustering algorithm. The number of clusters is fixed to two, namely, multipath and no-multipath sets, also maintaining the information of the satellite PRN numbers. Once the measurements are gathered into two clusters (C_1 and C_2), a decision mechanism has to be implemented in order to decide which cluster includes the satellites suffering from the multipath or not.

The details of the data preparation and implementation of the algorithm are provided in the following.

Data Preparation and Details of the Implementation

Data preparation is, in general, the most important step in machine learning applications. GNSS measurements have to be put into a format so that the algorithm could cluster them in the correct way, eventually gathering the satellites affected by multipath into the same group.

In this implementation, the dimension (μ) of the data set (X) where the definitions are provided in Section 5.3.2 is set to three by including the carrier phase, pseudorange and C/N_0 measurements for each tracked satellites. In Figure 5.13, the data preparation procedure for the pseudorange measurements is depicted. The implementation for the carrier phase and C/N_0 measurements is repeated in the same way.

As it can be seen in Figure 5.13, a sliding window of size T_{w} is applied to include a number of measurements at the consecutive epochs. The pseudorange measurements of each visible satellite during the considered window duration are passed through a designed feed-forward filter depicted in Figure 5.14:

$$\Delta\rho^{k}_{W_j}(t_i) = \sum_{k=0}^{M} b_k \, \rho^{k}(t_i - k) \tag{5.20}$$

where $\rho^{k}(t_i)$ is the last pseudorange measurement of the satellite PRN k at time t_i in the applied window W_j. The applied filter is referred to as a tapped-delay line filter or finite-duration impulse response (FIR) filter [225] that consists of three basic elements, namely, unit delay elements (z^{-1}), multipliers with respective tap

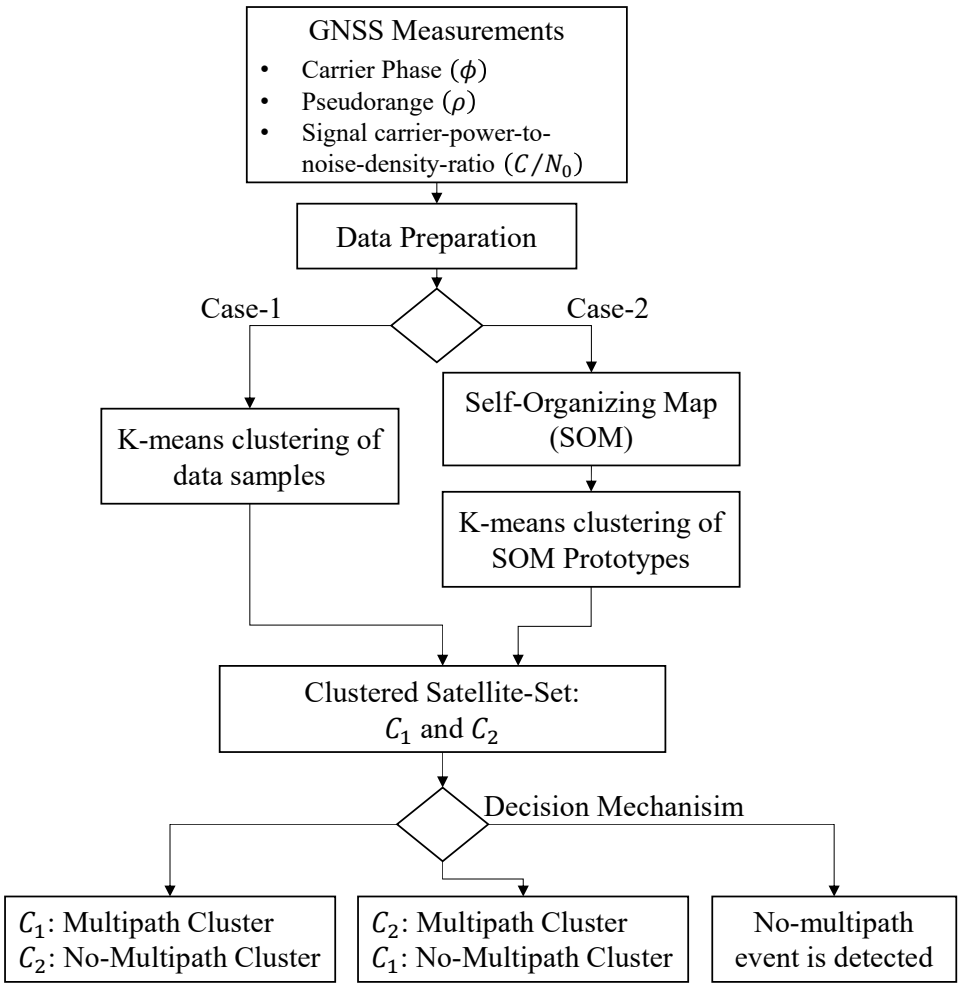

Figure 5.12: Flow chart of the implemented algorithm.

weights (b_k), and adders that sum individual multiplier outputs yielding the filter output $\Delta\rho^k_{W_j}(t_i)$. M is the number of delay elements and referred to as the filter order. The scope of this filter is detrending of the time-series of the pseudorange values, in other words, the removal of the deterministic variability over time of the psedorange values. For this reason, the tap weights (b_k) of the FIR filter are determined from the computed finite-difference coefficients for different orders [226]:

$$\left.\frac{d^m f}{d\,x^m}\right|_{x=x_0} \approx \sum_{\nu=0}^{n} \delta^m_{n,\nu}\, f(\alpha_\nu), \quad m = 0,1,...,M \quad \text{and} \quad n = m, m+1, ..., N \tag{5.21}$$

where M is the order of the highest derivative to be approximated. α_ν is a set of $N+1$ grid points having uniform spacing and centered at $x = x_0$ (i.e. at the first point). $\delta^m_{n,\nu}$ are the coefficients of the forward differences that are applied in the

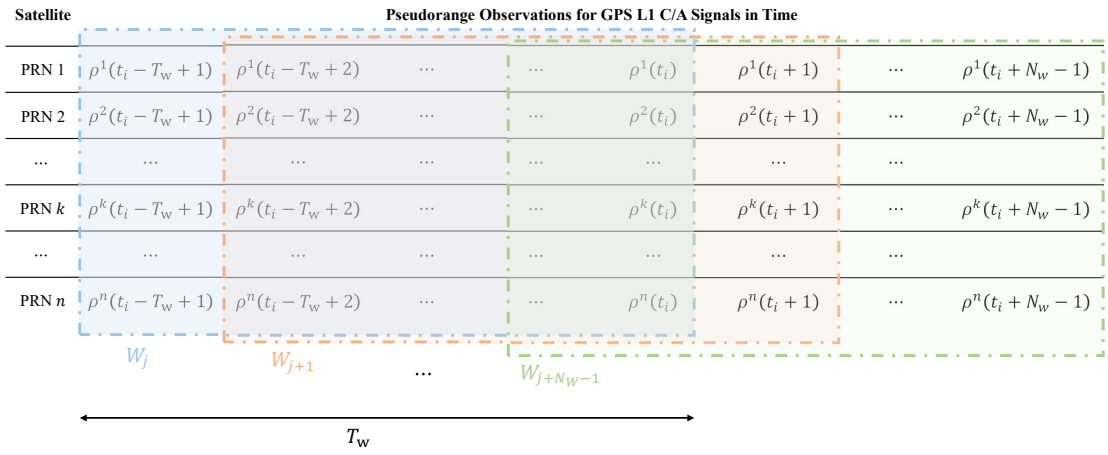

Figure 5.13: Preparation of the pseudorange measurements to clustering algorithm through the sliding windows of size T_W.

FIR filter above. For example, in case of the number of observations is set to five in the window (i.e. $T_w = 5$), the applied tap-weights in the filter to approximate different orders of derivations are listed in Table 5.6.

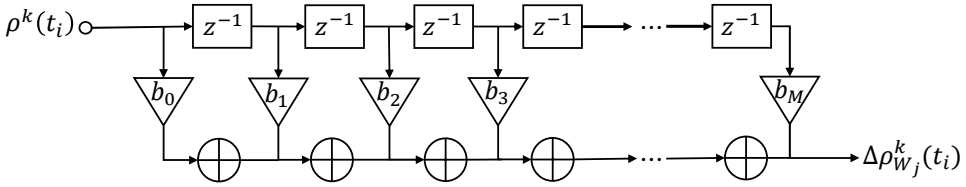

Figure 5.14: Feed-forward filter applied to the measurements during the duration of the window W_j.

Table 5.6: Tap Weights in the Applied FIR Filter for $T_w = 5$ to Approximate Different Orders of Derivatives

Order of derivative (M)	Tap-weights of the filter				
	b_0	b_1	b_2	b_3	b_4
2	35/12	−26/3	19/2	−14/3	11/12
3	−5/2	9	−12	7	−3/2
4	1	−4	6	−4	1

Furthermore, through differentiation operation, deterministic errors common to consecutive pseudorange values are removed. Then, the filter outputs are organized in a vector

$$x^k_\rho = \begin{bmatrix} \Delta\rho^k_{W_j}(t_i) & \Delta\rho^k_{W_{j+1}}(t_i+1) & \cdots & \Delta\rho^k_{W_{j+N_w-1}}(t_i+N_w-1) \end{bmatrix} \tag{5.22}$$

where N_{w} is the number of windows applied. $(t_i + N_{\mathrm{w}} - 1)$ corresponds to the last time index of the applied windows depicted in Figure 5.13. After collecting the results of the N_{w} consecutive sliding windows, the standard deviation of the measurements is computed:

$$\sigma_{\rho}^{k} = \sqrt{\frac{1}{N_{\mathrm{w}} - 1} \sum_{i=1}^{N_{\mathrm{w}}} \left(x_{\rho}^{k}(i) - \frac{\sum_{i=1}^{N_{\mathrm{w}}} x_{\rho}^{k}(i)}{N_{\mathrm{w}}} \right)^{2}} \tag{5.23}$$

All the computed standard deviation values for the carrier phase (σ_{ϕ}), pseudorange (σ_{ρ}), and C/N_0 (σ_{C/N_0}) measurements are then organized in the data set matrix (5.13)

$$X = \begin{bmatrix} \sigma_{\phi}^{1} & \sigma_{\rho}^{1} & \sigma_{C/N_0}^{1} \\ \cdots & \cdots & \cdots \\ \sigma_{\phi}^{k} & \sigma_{\rho}^{k} & \sigma_{C/N_0}^{k} \\ \cdots & \cdots & \cdots \\ \sigma_{\phi}^{n} & \sigma_{\rho}^{n} & \sigma_{C/N_0}^{n} \end{bmatrix} \tag{5.24}$$

is ready to be fed as input to the clustering algorithm.

In the implementation the number of sliding windows (N_{w}) and window sizes (T_{w}) were chosen as $N_{\mathrm{w}} = 3$ and $T_{\mathrm{w}} = 5$. Such values could be increased; however, it comes to the cost of data buffering during which an output cannot be provided. On the other hand, a shorter observation time $(N_{\mathrm{w}} + T_{\mathrm{w}} - 1)$ might not be adequate to perceive the changes in the measurements that reflect inconsistency. In our implementation, as it can be inferred from Figure 5.13, in this case during the first 7 measurement epochs the clustering algorithm is not able to produce a result; however, after this data buffering period, clustering outputs at every measurement epochs. In a dynamic environment the shorter is this transient time better is since the propagation condition may change in a fast way.

In this study, as being different from the general K-means clustering algorithm, the computation of the objective function (J) [see (5.15)] is needed to be modified by applying a weighting ($\bar{w}$) to the parameters (i.e. the dimensions (μ) of the data set) [12]:

$$\bar{w} = \begin{bmatrix} w_{\phi} & w_{\rho} & w_{C/N_0} \end{bmatrix} \tag{5.25}$$

$$J = \sum_{j=1}^{k} \sum_{x \in C_j} \bar{w}\, d\,(x, m_j)^2 \tag{5.26}$$

where $\bar{w}$ is the weighting vector for the carrier phase, pseudorange, and C/N_0 measurements. The summation of the weighting parameters is equal to 1. As it has been indicated, since the carrier multipath is much smaller than the code multipath, w_{ρ} is higher than w_{ϕ} and w_{C/N_0} in order to balance the different contributions.

Moreover, in order to decide which cluster includes the satellites suffering from the multipath and also to take into account a case of the no-multipath scenario, a decision mechanism has been developed. After the satellite set is gathered in the clusters C_1 and C_2, the mean values of the C/N_0 measurements of the satellites in the same cluster are computed as $\bar{c}_1$ and $\bar{c}_2$. The values are compared to a threshold in order to decide which cluster includes the satellites suffering from the multipath or not:

- $(\bar{c}_1 > \bar{c}_2) \wedge (\bar{c}_2 < \text{th}) \implies C_2 : \text{multipath cluster}, C_1 : \text{no-multipath cluster}$
- $(\bar{c}_1 < \bar{c}_2) \wedge (\bar{c}_1 < \text{th}) \implies C_1 : \text{multipath cluster}, C_2 : \text{no-multipath cluster}$
- $((\bar{c}_1 < \bar{c}_2) \vee (\bar{c}_1 > \bar{c}_2)) \wedge ((\bar{c}_1 > \text{th}) \wedge (\bar{c}_2 > \text{th})) \implies \text{No-multipath}$

At the decision mechanism, especially considering a no-multipath scenario, a threshold is needed to be defined. It is not so straightforward to develop an adaptive algorithm taking into account both multipath effect and NLOS reception since the changes of the C/N_0 measurements with changing elevation angles under a multipath environment are dependent on many factors. In this work such a threshold was heuristically set by means of an extensive analysis of simulated and real GNSS data sets.

The other setting parameters of the algorithm have been tuned by means of a simulation campaign as described in the following.

Algorithm Setting

In this study, both real GNSS data and simulated data, in which the ionospheric, tropospheric, and multipath errors are modeled, are exploited. An example of simulated multipath data is provided in Section 3.3.2. Through the simulated data implementation, the setting parameters of the implemented algorithm have been decided. The implementation of the algorithms and the analyses have been done by employing the SOM Toolbox [224] and MATLAB (R2016b, The Mathworks, Inc., Natick, MA, USA) [205].

The input data are put into the format defined in X in (5.24) and depicted in Figure 5.15. This is the input to K-means clustering in the Case-1 implementation where the data are directly fed to the clustering algorithm. For the same input data, in Case-2 implementation, the input space of the SOM algorithm consisting of the initialization of neurons (represented as black dots) and their neighborhood links (depicted as gray lines) is shown in Figure 5.16 (a).

As it can be observed in Figure 5.16 (a), SOM algorithm requires prototype vectors (i.e. weight vectors representing neurons) that have the same vector dimensionality of the input data in order to form a surface that interpolates at its best the input data. However, the SOM algorithm output space depicted in Figure 5.16

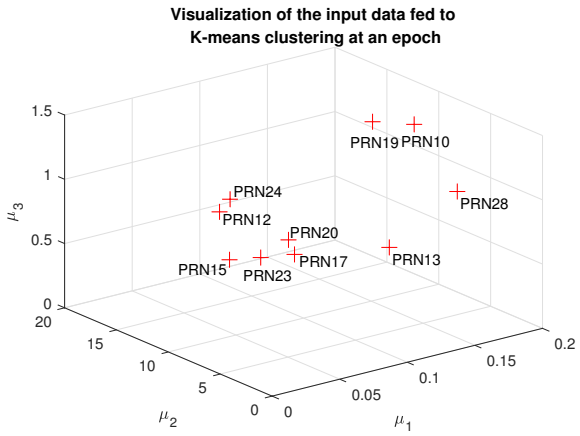

Figure 5.15: Case 1 - Visualization of the simulated input data for K-means clustering.

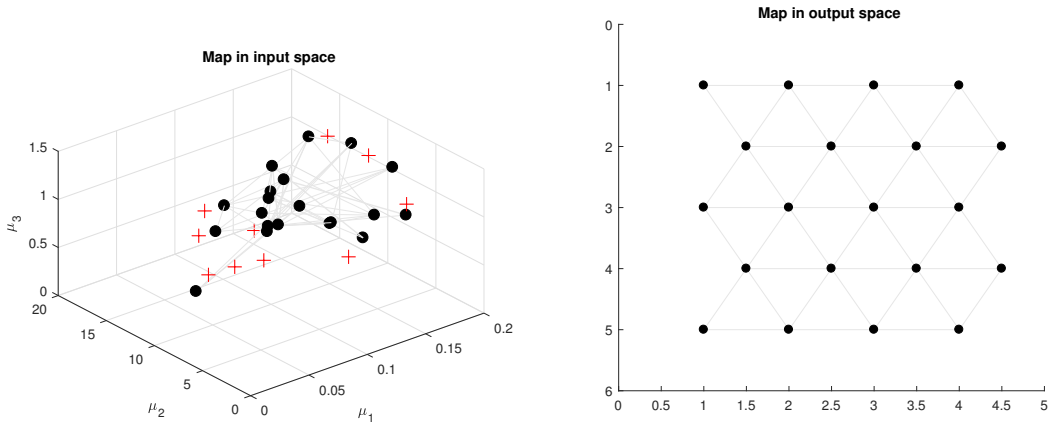

(a) SOM input space.

(b) SOM output space.

Figure 5.16: Case 2 - Visualization of the SOM input space and SOM output space that is input to K-means clustering.

(b) is arranged in 2-dimensional space with hexagonal lattice considering its better visual effect compared to rectangular lattice [222]. The map size is adaptively adjusted depending on the number of PRNs. Then this map is fed to the K-means clustering in the Case-2 implementation.

Parameter tuning has been heuristically implemented searching for suitable values of the parameters through the simulated data analysis and they are summarized in Table 5.7.

In the SOM algorithm detailed in Section 5.3.2, the neighborhood radius $\sigma(t)$ of the widely applied Gaussian kernel function $h_{bi}(t)$ is set to a relatively large value

Table 5.7: Summary of Setting Parameters

Stage	Parameters	Values
Data Preparation	Dimension (μ) of the data set	3
	Number of observations	Number of visible satellites
	Window size T_w	5
	Number of consecutive windows N_w	3
	The order (M) of the FIR filter	2,3,4
Self-Organizing Map	Dimensionality	2-dimensional space
	Map size and map lattice	Adaptive and hexagonal
	Neighborhood function $h_{bi}(t)$	Gaussian
	Neighborhood radius $\sigma(t)$	Linearly decreasing: $\sigma_{init} = 5$ and $\sigma_{final} = 1$
	Learning rate function $\alpha(t)$	Inverse of time: $\alpha(t) = \alpha_0/(1 + 100t/T)$
	Training length T	10
	Initial learning rate α_0	0.05
K-means Clustering	Number of clusters	2
	Iteration value	5
	Weighting	$\bar{w} = \boxed{0.15 \quad 0.45 \quad 0.40}$
Decision Mechanism	Threshold (th) C/N_0	38-40 dBHz

σ_{init} in the first phase of training so that SOM approximately is tuned to the same space of the input data. It ends with a smaller value σ_{final} for the fine tuning of the map. It has to be also noted that the neighboring function influences the training results, and selecting a proper function depending on the characteristics of the datasets is quite important. In the same sense, learning rate function $\alpha(t)$ is a non-increasing function and can be linear, power series, or inversely proportional to time t [227]. In this study, inverse of time function having an initial learning rate α_0 has been used for SOM training during the training time T. These two hyperparameters, namely, the learning rate and neighborhood function radius, are important to adjust the compatibility between the model and data distribution.

Furthermore, in the K-means algorithm, a predefined iteration value has been decided to avoid a case of that convergence is not reached. The quality of final clustering is dependent on the convergence check, stop criterion, and also the way applied for the initialization of the data. The cost of the optimal solution decreases with increasing number of clusters, which is fixed in this study. Although K-means is the most widely used clustering algorithm due to its simplicity, reasonably scalability, and modifiability to deal with datasets, there are some drawbacks such as being highly sensitive to initialization and description of the data [211].

5.3.4 Experimental Tests

After the algorithms have been set and tuned by means of the simulated data sets, their performance has been analyzed through static and kinematic real data sets.

Visual Analysis of the SOM

In order to visualize and analyze the results of the SOM algorithm, U-matrix technique is exploited [222]. Figure 5.17 shows an example of the results on a graphic display called the U-matrix. The U-matrix shows the average distances between neighboring prototype vectors represented by pseudo-color scales [220, 222]. Whereas dark shades represent large distances, light shade is used for a small average distance of neighboring [224]. Moreover, the U-matrix located on the top left is shown along with three component planes of carrier-phase, pseudorange, and C/N_0 related measurements. As it is depicted on an empty grid below, each hexagon corresponds to a different PRN in the component planes shown.

In this example, Figure 5.17 also consists of the K-means clustering of the SOM prototypes based on the measurement-sets that belong to duration between 17:37:43 and 17:37:50 UTC of a real static data collected on 29 May 2016. In other words, the algorithms are run once for one observation time ($N_\mathrm{w}+T_\mathrm{w}-1=7\,\mathrm{s}$). In Figure 5.17, it can be observed that the U-matrix does not show a clear separation among the satellites of which the PRN labels are given on the empty grid. However, from the component planes, it can be seen that some correlation exists between carrier-phase and pseudorange related measurements indicating a close relation of some satellites in terms of observed effect on the measurements. With the application of K-means clustering, three satellite signals (e.g. PRN 10, PRN 11, and PRN 17) are clustered into the same subset, and through the designed detection mechanism they are claimed to be the satellite signals suffering from the multipath effect.

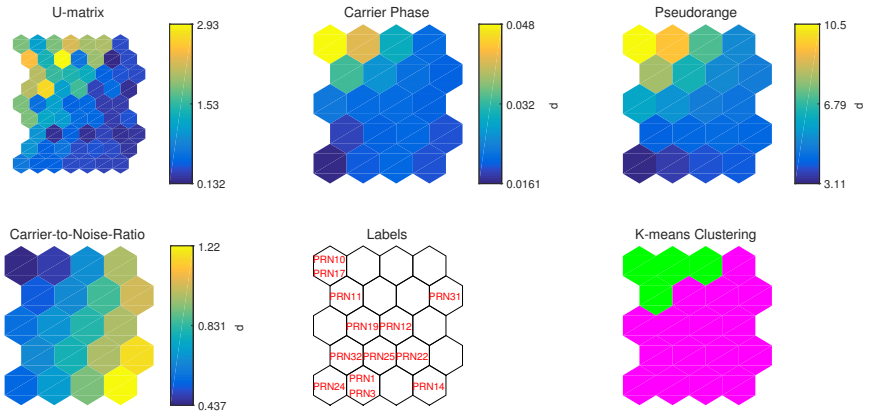

Figure 5.17: K-means clustering of the SOM prototypes based on the measurement-sets that belong to duration between 17:37:43 and 17:37:50 UTC of the data collected on 29 May 2016 at SANAE IV.

Real Static Multipath Data

In the analyses, different data sets that were collected at the Antarctic station SANAE-IV have been used. The collected data is obtained from a scintillation monitoring station by means of a data grabber and an implemented GNSS software radio receiver [47, 65]. These data are interesting because they might be affected by scintillation and multipath. They can be exploited to demonstrate the effectiveness of a good multipath estimation. In fact, exclusion of multipath affected PRNs improves the positioning performance, but multipath is also a threat for the scintillation monitoring operations.

- Degradation in the positioning accuracy due to multipath

  As it has been exemplified in Section 3.3.2, when the satellites that suffer from the multipath effect are included in the position computation, a degradation in the accuracy and precision of the position solution is inevitably expected. Figure 5.18 (a) shows the sky plot of the visible satellites considering an elevation mask angle of 5 degrees by processing data collected between 17:30 and 17:40 on 29 May 2016 at the station. Figure 5.18 (b) shows the computed positions with different satellites in UTM coordinate system by processing the same data. The differences between the different clouds of points can be noticed in Figure 5.18 (b), and it is observed that the estimated receiver position is pulled toward erroneous solutions when the satellite signals influenced by the multipath effects are not eliminated. Moreover, it is explained and detailed how this degradation is attributed to the multipath effect for some satellite signals through the analysis of the same data in the following of the thesis.

- False scintillation due to multipath

  Scintillation is caused by the ionospheric irregularities affecting GNSS signals in both refractive and diffractive ways associated with random propagation delay and signal attenuation factor as observed in the multipath effect. Two parameters, namely, S_4 index and σ_ϕ index, are used to indicate the amount of scintillation effect in a received GNSS signal [56]. Both indices are computed from the signal tracking stage outputs and whereas the S_4 index is the standard deviation of the received power that is computed from the normalized prompt correlator samples, the σ_ϕ index is the standard deviation of the detrended carrier phase measurements [56].

  As an example, Figure 5.19 (a) and (b) show the computed S_4 index values for the tracked GPS L1 C/A signals at the same time of the consecutive days at the Antarctic station. Although it is likely that due to the polar location of the SANAE IV station it is expected that phase scintillation occurs more frequently, increases in the amplitude scintillation levels of some satellites

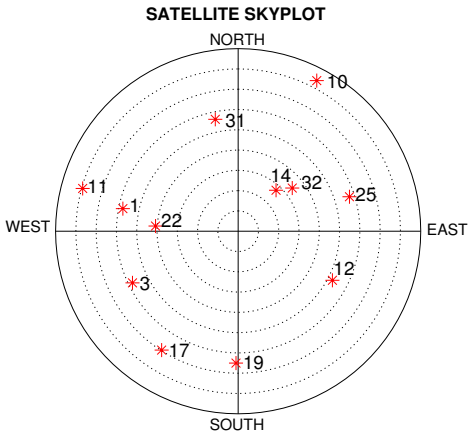

(a) Sky plot of the GPS satellites during the collection interval.

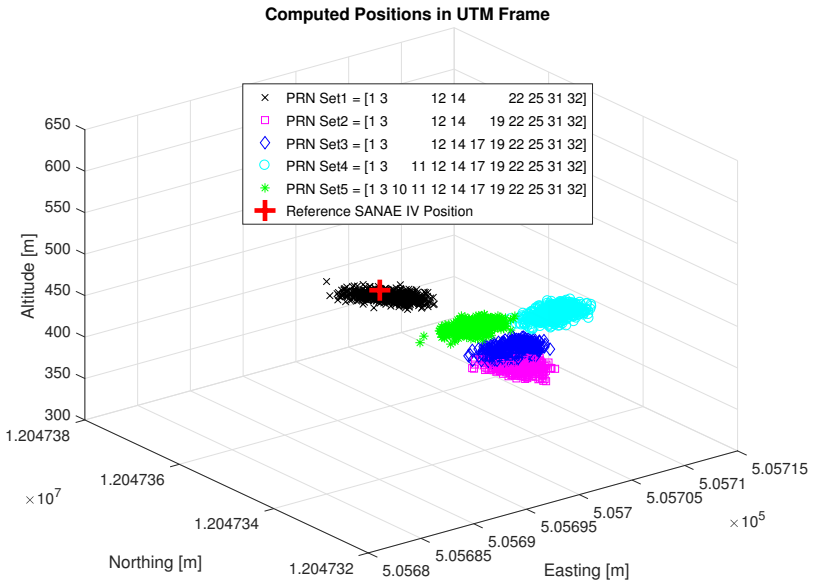

(b) GPS L1 C/A position solution in UTM frame with different PRN sets.

Figure 5.18: Sky-plot of GPS satellites and positioning solution computed using the data collected between 17:30-17:40 on 29 May 2016 at SANAE IV station.

are observed. However, as it can be noticed in Figure 5.19 (a) and (b), the changes in the computed S_4 index values of some satellites (e.g. PRN 10, PRN 11, PRN 17 etc.) repeat and follow almost the same trend daily depending

on the satellite motion since the station position is fixed. This is why the observed effect is attributed to multipath influence on the received signals of the aforementioned satellites.

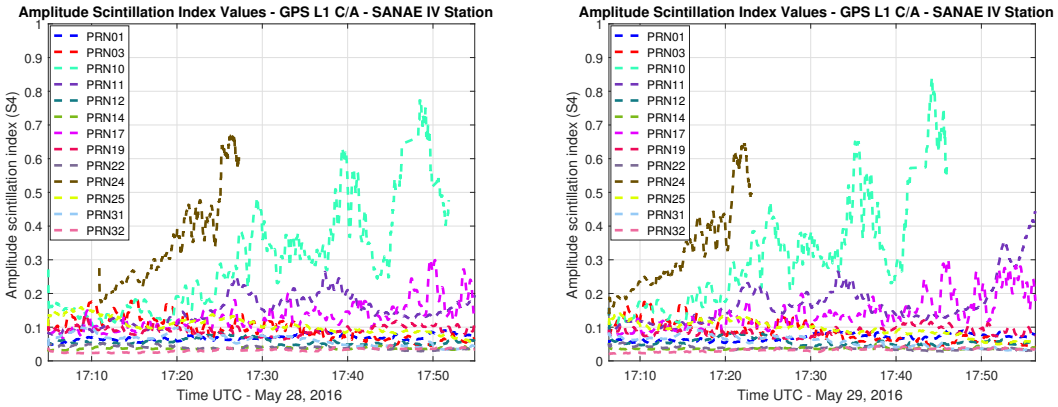

(a) GPS L1 C/A Signals - S4 Index Values - 28 May 2016.

(b) GPS L1 C/A Signals - S4 Index Values - 29 May 2016.

Figure 5.19: Amplitude scintillation index values at GPS L1 C/A signals - 28-29 May 2016 SANAE IV Station.

By following the data preparation procedure, GPS measurements computed from the processed data set collected on 29 May 2016 are put into the format and processed. In Figure 5.20, clustering percentages of the tracked GPS satellites into the multipath class for a 10-minute period are shown. It has been observed that the received signal of satellite PRN 10 of which the computed S_4 index is mostly higher than 0.3 as depicted in Figure 5.19 (b) has been classified as multipath signal with an accuracy of 90 %.

Tests of the clustering algorithm

The multipath events have been identified by inspection of the cases in which similar trends on the S_4 indices on the consecutive days exist and having S_4 indices higher than 0.3. Then, the clustering algorithms have been applied and the performance of the algorithms is reported in Table 5.8.

The results given in Table 5.8 clearly shows that clustering algorithm can be used to classify the multipath signals considering the accuracy values reported. With the results obtained specific to static data set at the monitoring station, the algorithm provides us to overcome the need of the computation of scintillation indices, the comparison of the indices for the same satellites on the consecutive days, and collection of large training data sets a-priori for an application of a possible supervised algorithm for multipath detection.

As it is mentioned in Section 5.3.2, in terms of computational complexity, it is more convenient to cluster a set of prototypes rather than directly the data [220].

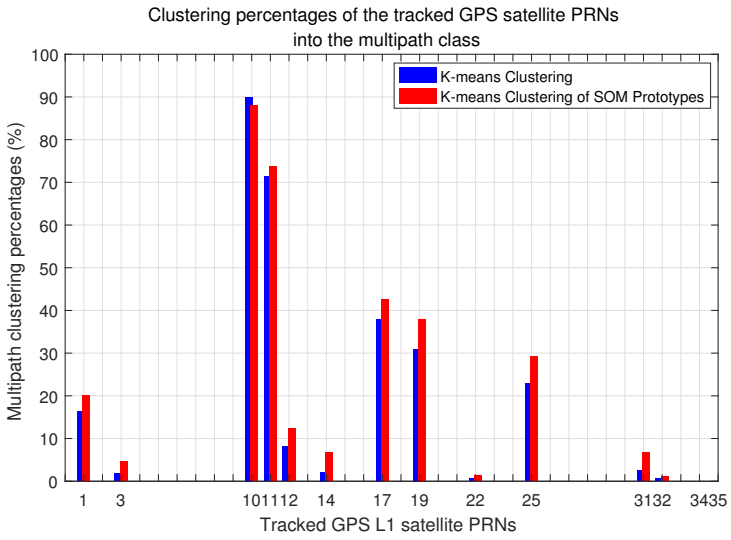

Figure 5.20: Clustering percentages of tracked GPS satellite PRNs into the multipath class for a 10-minute period between 17:30 and 17:40 on 29 May 2016 at SANAE IV Station.

Table 5.8: Multipath Clustering Performance of Real Static GPS L1 C/A Measurements Collected at SANAE IV Station.

Date	**Start-End Times (UTC)**	**GPS PRNs affected**	**K-means clustering (Case-1) with the FIR filter having**			**SOM Prototype Based Clustering (Case-2) with the FIR filter having**		
			Order=2	**Order=3**	**Order=4**	**Order=2**	**Order=3**	**Order=4**
01/02/16	05 : 40 – 05 : 50	31	88.26 %	**88.82** %	88.14 %	85.06 %	86.46 %	87.27 %
	05 : 10 – 05 : 20	5	89.54 %	90.22 %	90.60 %	91.28 %	91.12 %	**91.57** %
06/03/16	16 : 20 – 16 : 30	9	90.50 %	90.18 %	90.35 %	**91.85** %	91.68 %	91.68 %
02/06/16	09 : 40 – 09 : 50	9	86.54 %	86.21 %	86.38 %	89.20 %	89.20 %	**89.37** %
03/12/16	07 : 40 – 07 : 50	25	93.85 %	93.85 %	94.19 %	93.02 %	94.35 %	**94.68** %
04/01/17	10 : 00 – 10 : 05	10	91.03 %	89.53 %	90.03 %	**93.69** %	93.36 %	92.69 %

Besides, when the accuracies of the clustering operations are compared it has been observed that the percentages of correctly clustering the satellite signal suffering from multipath has improved through the application of SOM algorithm as well. Moreover, thanks to the projection realized from three-dimension to two-dimension through the SOM algorithm, clustering run-time complexity that deals with the time spent on the execution of the algorithm has decreased. For example, in the case of having tracked 11 visible satellites, it has been measured that running time of directly clustering the data is around 1.5 times the spent time for clustering the prototypes.

Real Kinematic Multipath Data

The urban testing environment allowed collecting the GPS L1 C/A data sets containing multipath interference and NLOS reception through the road test that was conducted in The Hague, The Netherlands utilizing a USRP N210 front-end. Figure 5.21 shows the trajectory of the data collection campaign obtained from the commercial receivers (e.g. Trimble and Septentrio) that are able to process multi-constellation multi-frequency satellite signals. Throughout the implementations and analysis carried out in this study, only L1 C/A signal of the GPS constellation is considered to make the single frequency position computation robust to the multipath effect by detecting the satellite signals that suffer from the multipath effect and excluding them from the computation of the position.

Figure 5.21: The Google Earth trajectory of the collected GNSS raw data using a car equipped with GNSS antenna, front-end (USRP N210) and commercial GNSS receivers (Septentrio and Trimble) in The Hague, The Netherlands.

Figure 5.22 shows a portion of the trajectory during which multipath/NLOS effects are quite visible in the positioning estimations obtained through the processing of GPS L1 C/A signals. The red car icons show the position estimations from the commercial receiver that has the ability of processing multi-frequency and multi-constellation satellite signals and of which the estimations are improved with

the support of float-ambiguity fixed PPP results. The blue car icons indicate the position estimations computed from the GPS measurements obtained by processing the front-end outputs (i.e. raw GPS IF data) through the software receiver. It has been computed that the 2D positioning difference between the red car icons, which are accepted as ground-truth, and the blue car icons is around 9.5 meters.

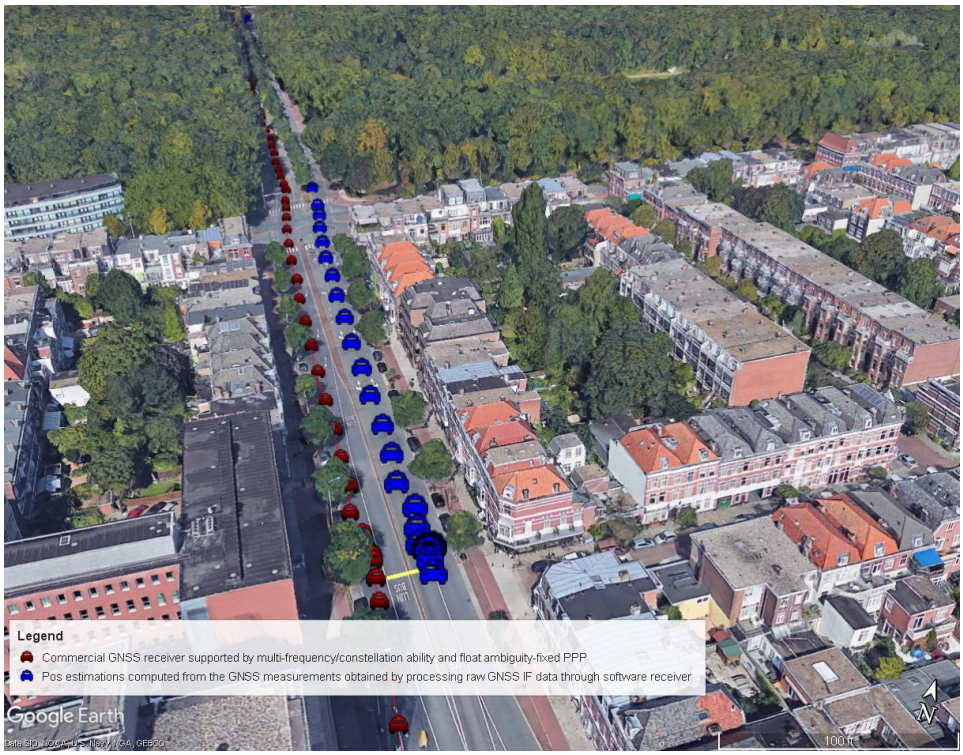

Figure 5.22: Biased position estimation due to the multipath effect and/or NLOS reception.

Whereas the number of visible GPS satellites is around $10-11$ in the forestry area shown in Figure 5.22, it decreases to $6-7$ by losing the track of the low-elevation satellite signals that are circled in Figure 5.23 on the road between tall buildings located on both sides of the road. It is confirmed by the increase of the Geometric Dilution of Precision (GDOP) jumping from 1.717 to 3.128.

During the conducted road tests, when the portion of the roads in which tall buildings have adverse effects on the number of visible satellites by the receiver, clustering algorithm has run. Figure 5.24 (a) shows the sky plot of GPS satellites. As being different from the sky plot depicted in Figure 5.23, the satellite signal broadcast by PRN 30 has also been acquired and tracked. Figure 5.24 (b) shows the K-means clustering of the SOM prototypes based on the measurement sets of the tracked satellites. It is observed that two satellites, PRNs 8 and 30, are clustered as multipath signals. When the measurements obtained from these satellite signals are

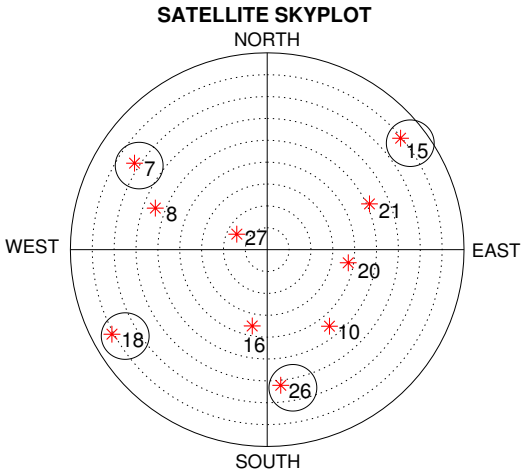

Figure 5.23: Sky plot of the GPS satellites observed during the portion of the conducted real kinematic test.

not included in the positioning computation, the positioning errors have decreased around 2.3 meters in the 2D positioning estimations, getting closer to the ground-truth solutions.

When the data preparation procedure is considered, during the first 7 measurement epochs the clustering algorithm is not able to produce a result due to data buffering although it might not be so significant for the static scenarios. However, after this data buffering period, it has been observed clustering provides a remarkable information on the satellite selection at every measurement epochs.

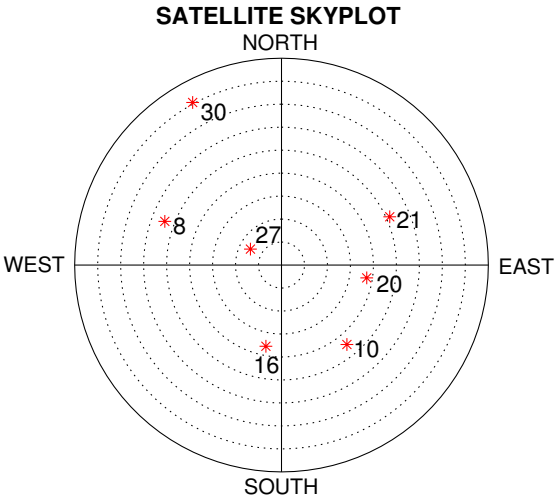

(a) Sky plot of the GPS satellites.

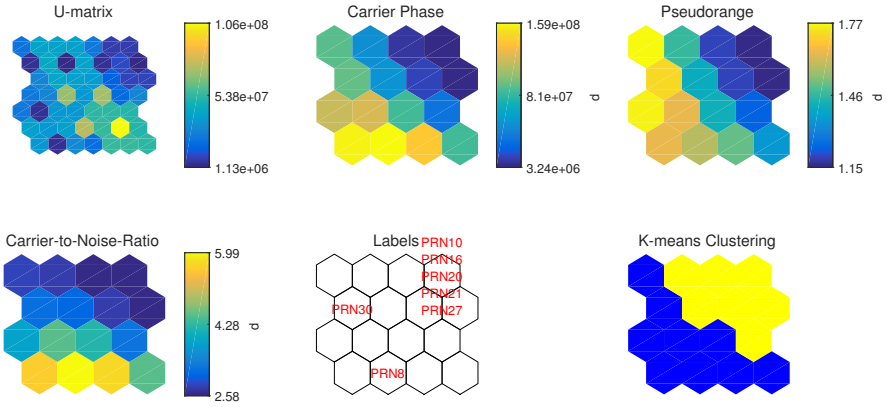

(b) K-means clustering of SOM prototypes.

Figure 5.24: SOM Prototype Based K-Means Clustering of Real Kinematic GPS Measurements under Multipath Effects and/or NLOS Receptions.

Chapter 6

Conclusions and future activities

The thesis deals with analyzing the scintillation and multipath effects on the receiver side by means of a designed and developed multi-frequency and multi-constellation software GNSS receiver. The main objective of the work has been to investigate and develop new approaches to the receiver design focusing on the signal processing stages. In particular, it has addressed the AI solutions through different ML- and DL-based methods.

As an introduction, Chapter 2 provides an overview of a GNSS receiver architecture, main GNSS error sources, and the concept of SDR-based GNSS receiver, which has been considered in the development of the work.

In Chapter 3, scintillation and multipath effects are specified in detail. With the description of scintillation measurements on the receiver side, as an introduction to the experimental part of the thesis, the data collection setup utilizing the SDR receiver approach and some analysis of the real scintillation data have been provided. Having discussed the scintillation models and classical detection strategies proposed in the literature, the significance of real data collection to observe the actual effects of the scintillation on the receiver side and the need for new approaches for scintillation detection have been defined. Likewise, after analyzing the multipath effect on the GNSS measurements and observables, classical multipath detection strategies in the literature have been discussed. The analyses have contributed to the development of the multipath detection algorithm that has been proposed in the thesis.

In Chapter 4, different signal acquisition techniques and different carrier tracking methods, namely, traditional PLL and KF-based PLL for GPS L1 C/A and L5 signals have been used to analyze their performance under strong amplitude and phase scintillations and the no-scintillation environment by exploiting the real GNSS signals. Even if the implemented acquisition and tracking structures are well known in the literature, the scope of this research is to select the optimal acquisition and tracking parameters able to make a GPS receiver robust enough to work even under strong scintillation conditions.

- In acquisition stage, it has been observed that the usage of only one channel for the GPS L5 signal, namely the pilot channel, provides simplicity and reduction in the computational load. In addition, having compared the performance of the algorithms for L5 and L1 C/A in terms of ROC curves, peak-to-floor ratios, the signal acquisition time or computational load, the trade-off between sensitivity and complexity has been provided to evaluate better the performances of the acquisition methods. Concerning the performance under scintillation, under phase-only scintillation, although the signal is acquired all the time, a loss in the probability of detection is computed around $0.013 - 0.002$. Although the phase scintillation is not at the level to prevent the acquisition of the scintillated signal, the phase scintillation accompanied by the strong amplitude scintillation can prevent the acquisition of the signal. In that case, extending the integration time can be considered as a solution and Method-C performs best among the other methods. Among Method-A and Method-B, which both have the lowest coherent integration times that are equal to one code period, Method-B employing the zero-padding approach provides slightly better performance at the cost of an increased computational burden compared to Method-A.

- In tracking stage, with the performance analysis in terms of the residual errors on the receiver observables and internal parameters, it is observed that although L5 signal experiences larger fluctuations under scintillation due to its lower frequency, the tracking outputs of the processed L1 C/A signal have provided more errors, mostly due to lower power with respect to the L5 signal. It has been showed that extending the integration time and lowering the noise bandwidth have benefits on the accuracy and loss-of-lock durations of the tracking measurements up to a point. Furthermore, although KF-based carrier tracking outperforms the PLL-based tracking, it can also fail under both strong amplitude and phase scintillation conditions, yet it performs with having no loss-of-lock duration under phase-only scintillation events.

In Chapter 5, after providing an overview of AI solutions and discussing the role of ML in a GNSS receiver, the implementations of the designed scintillation and multipath detection methods have been defined. The main contributions on these approaches can be summarized as follows:

- The linear, Gaussian, and polynomial kernel SVM algorithms for both phase and amplitude scintillation detection have been reviewed and analyzed. Performance comparison has been assessed by exploiting the ROC curves, confusion matrix results, and the performance metrics associated with the confusion matrix. It has been observed that, if the kernel scale parameter of Gaussian RBF kernel SVM algorithm is optimized, the performance of the RBF kernel SVM method outperforms the linear kernel SVM method in terms of overall

accuracy. Moreover, although third order polynomial kernel SVM performs better than the linear kernel, it comes with a cost of increased time and space complexity. Furthermore, although the differences in the accuracy rates of the methods seem not to be at a considerable level (e.g. around 1 % among different kernel functions), the method providing higher accuracy gains critical importance in terms of early detection considering that the fed scintillation indices to the algorithm have a sampling interval of 60 s.

- GNSS multipath detection algorithms based on unsupervised machine learning algorithms, namely, K-means and SOM, have been designed, implemented, and tested. By processing common GNSS receiver observables, namely, carrier phase, pseudorange, and carrier-to-noise-ratio creating clusters of consistent measurements to allow the identification of satellite signals suffering from the multipath error has been targeted. The test results realized with both static and kinematic data sets exploited in the study have an outcome of improved accuracy in the positioning. It has been observed that correctly clustering of the satellite signals suffering from multipath with accuracies reaching 90 % in the output of the algorithm has been possible. However, the improvement in the overall positioning accuracy is dependent on the conducted test scenario where type and strength of multipath signals (e.g. NLOS and LOS), number of satellites suffering from the multipath, and test type (e.g. static or kinematic) can be various. For example, in specific static and kinematic test configurations, it has been possible to obtain around 10 m and 2.5 m improvement in 2D positioning accuracy, respectively.

  Moreover, it has been shown that applying the SOM algorithm before the K-means clustering is more convenient, less computationally complex, and having more accuracy rather than clustering the data directly through K-means algorithm. However, during a transient time (e.g. 7 measurement epochs) the clustering algorithm is not able to produce a result due to data buffering and this might be a limitation in high dynamics scenarios. The use of unsupervised algorithms, even if needs a proper initial tuning, allows for automatic detection of the multipath events, thus allowing the GNSS receiver to adapt to the environment and provide better performance.

Future activities could include investigations on the implementation of a DL algorithm for GNSS signal acquisition and tracking in a receiver architecture that can cope with harsh ionospheric scintillation and multipath conditions. Moreover, considering regression-based ML algorithms and DL approaches, prediction of satellite clock and orbital parameters to improve applied corrections and reach better accuracy in the positioning could be worked in case of non-availability of related information.

Appendix A

Software GNSS Receiver

A multi-frequency multi-constellation GNSS SDR receiver is developed in MATLAB language, and it is intended as a non-real time tool that is able to implement full processing chain from the received signal to the PVT computation including scintillation analysis capability.

A.1 Flow of the Algorithms

The flow diagram of software GNSS algorithms is shown in Figure A.1. Moreover, in order to ease the configuration of the receiver, a GUI has been created, and it is depicted in Figure A.2.

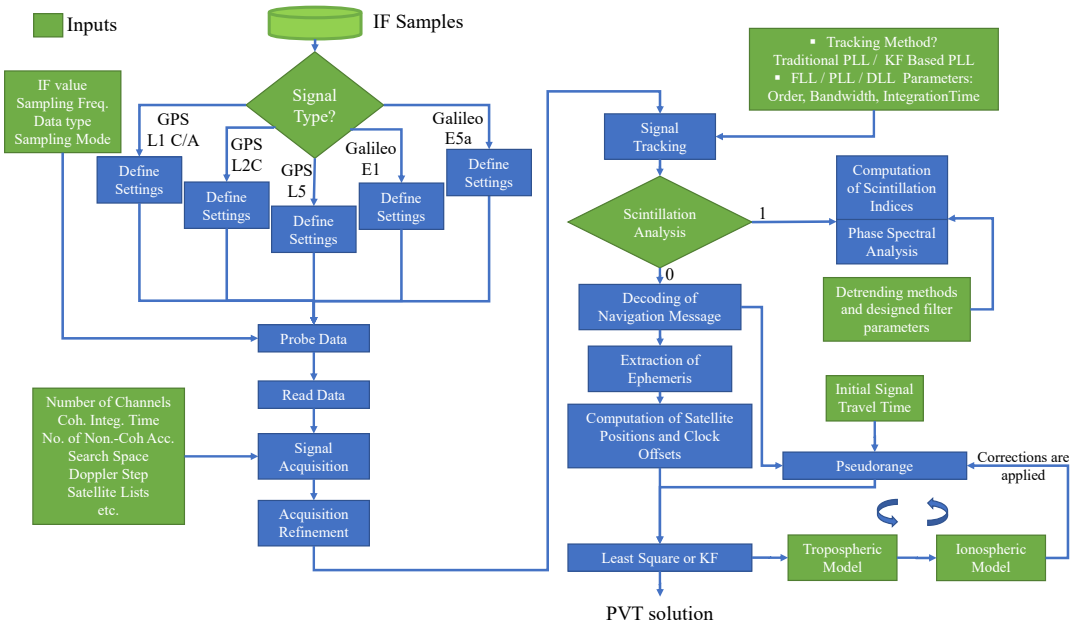

Figure A.1: Flow diagram of software GNSS receiver algorithms.

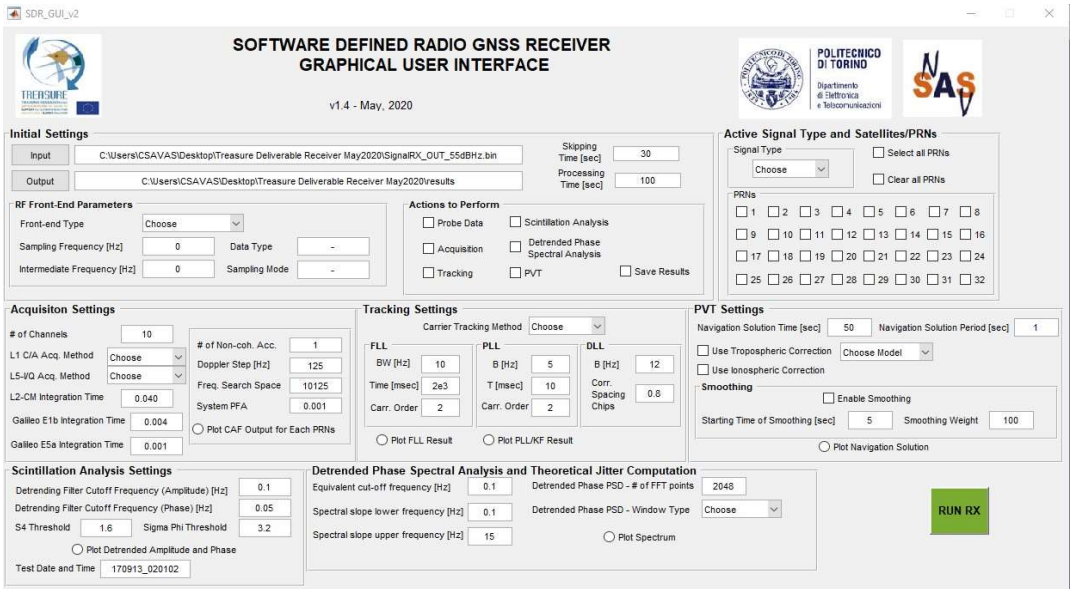

Figure A.2: Graphical User Interface (GUI) of MATLAB based Software Defined Radio (SDR) receiver.

A.2 Signal Carrier Tracking Strategies - Filter Designs

A key block in the carrier phase tracking loop is the loop filter that reduces the noise and tracks the variations of the signal.

A.2.1 Traditional PLL

A PLL discriminator computes the difference between the phase of the incoming signal and the locally generated signal. Here, a two-quadrant Costas PLL discriminator is given, which outputs the phase error as:

$$\delta\hat{\varphi}_k = \tan^{-1}\left(\frac{Q_k}{I_k}\right) \tag{A.1}$$

where I_k and Q_k are the in-phase and quadra-phase correlations at time k in the tracking stage. In Table A.1, the basics of second and third-order analog PLL filter architectures are summarized.

The parameter ω_n in the equations in Table A.1, is the natural frequency of the loop filter and it is computed from the bandwidth B_n, which is the designer's choice.

Table A.1: Specifications of the Analog Phase Lock Loop Filters

	Second Order Loop	**Third Order Loop**
Closed Loop Transfer Functions	$H_2(s) = \frac{\alpha_2\omega_n s+\omega_n^2}{s^2+\alpha_2\omega_n s+\omega_n^2}$	$H_3(s) = \frac{\beta_3\omega_n s^2+\alpha_3\omega_n^2 s+\omega_n^3}{s^3+\beta_3\omega_n s^2+\alpha_3\omega_n^2 s+\omega_n^3}$
Noise Bandwidth (Hz)	$B_n = \left(\frac{1+\alpha_2^2}{4\alpha_2^2}\right)\omega_n$	$B_n = \left(\frac{\alpha_3\beta_3^2+\left(\alpha_3^2-\beta_3\right)}{4(\alpha_3\beta_3-1)}\right)\omega_n$

Digital PLL transfer loop functions can be computed from their analog counterparts through the conversion of $s = \frac{1-z^{-1}}{T}$ where T is the integration time. The numerically controlled oscillator (NCO) that generates a sinusoid of which phase is related to the filtered discriminator output has a transfer function equal to $N(z)$:

$$N(z) = \frac{z^{-1}}{1 - z^{-1}} \tag{A.2}$$

Table A.2 shows the digital counterpart of the analog PLL filters. Moreover, the typical values, which are used in the literature to compute the PLL parameters, are given in Table A.2.

Table A.2: Specifications of the Digital Phase Lock Loop Filters

	Second Order Loop	**Third Order Loop**
Closed Loop Transfer Functions	$H_2(z) = \frac{(\alpha_1+\alpha_2)z-\alpha_1}{(z-1)^2+\alpha_1(z-1)+\alpha_2 z}$	$H_3(z) = \frac{\alpha_2}{(z-1)^3+\alpha_1(z-1)^2+\alpha_2 z(z-1)+\alpha_3 z^2}$
Loop Parameters	$\alpha_1 = \alpha_2\omega_n T$ $\alpha_2 = \omega_n^2 T^2$ Typically, $\alpha_2 = 1.414$ $B_n = 0.53\omega_n$	$\alpha_1 = \beta_3\omega_n T$ $\alpha_2 = \alpha_3\omega_n^2 T^2$ $\alpha_3 = \omega_n^3 T^3$ Typically, $\alpha_3 = 1.1$ & $\beta_3 = 2.4$ $B_n = 0.7845\omega_n$

In PLL loop filter design, there is a tradeoff in the decision of integration time (T) and loop bandwidth (B_n) parameters. In fact, in order to get more accurate carrier measurements, the integration time should be long and noise bandwidth should be narrow. However, under dynamic scenarios, the integration time should be kept short and the bandwidth of the filter should be maintained narrow [3]. Furthermore, the order of the filter that is related to the capacity of the filter to track the different types of signal dynamics also determines the loop filter's response [228].

A.2.2 Kalman Filter Based PLL

Kalman Filter (KF) based tracking is the recursive estimation of the time-varying states with the incoming observations by using the prior statistical knowledge about the variations. Generally, the following state-space system dynamic model [98]:

$$x_{k+1} = A_k X_k + G_k w_k \tag{A.3}$$

and the measurement model:

$$z_k = H_k x_k + v_k \tag{A.4}$$

are used, where the dimension and description of the variables are listed in Table A.3.

Table A.3: Description of the Kalman Filter (KF) based carrier tracking variables

Variables	**Vector/Matrix**	**Dimensions**
State vector	x_k	(3×1)
State transition matrix	A_k	(3×3)
Process noise matrix	G_k	(3×3)
Process noise vector	w_k	(3×1)
Measurement	z_k	(1×1)
Observation matrix	H_k	(1×3)
Measurement noise	v_k	(1×1)

In a conventional GNSS receiver, the state vector and the states in the KF-based PLL tracking are

$$x_k = \begin{bmatrix} \Delta\varphi & \Delta f & \Delta\dot{f} \end{bmatrix}_k \tag{A.5}$$

where $\Delta\varphi$ is the carrier phase error, Δf is the carrier frequency error and $\Delta\dot{f}$ is the carrier frequency rate error. The state transition matrix has the following form in this three state vector design [97]:

$$A_k = \begin{bmatrix} 1 & T & T^2/2 \\ 0 & 1 & T \\ 0 & 0 & 0 \end{bmatrix} \tag{A.6}$$

Having defined dynamic and measurement models, KF implementation is summarized in two steps [229], namely, prediction steps:

$$\hat{x}_{k+1}^{-} = A_{k+1}\hat{x}_k \tag{A.7}$$

$$P_{k+1}^{-} = A_k P_k A_k^T + Q_k \tag{A.8}$$

and correction steps:

$$K_k = P_k^- H_k^T \left[H_k P_k^- H_k^T + R_k \right]^{-1} \tag{A.9}$$

$$\hat{x}_k = \hat{x}_k^- + K_k \left[z_k - H_k \hat{x}_k^- \right] \tag{A.10}$$

$$P_k = \left[I - K_k H_k \right] P_k^- \left[I - K_k H_k \right]^T + K_k R_k K_k^T \tag{A.11}$$

where $\hat{x}_{k+1}^-$ is priori state estimates after the projection of the transition matrix on the states, P_{k+1}^- is priori estimate of state covariance matrix, Q_k is process noise covariance matrix, K_k is the KF gain vector with three elements which weight the error between the measurements and predictions. H_k is observation matrix defined as follows:

$$H_k = \begin{bmatrix} 1 & \frac{T}{2} & \frac{T^2}{6} \end{bmatrix} \tag{A.12}$$

R_k is measurement noise covariance matrix which is computed from $\mathrm{E}\left[v_k v_k^T \right]$. $\hat{x}_k$ is posteriori state estimates after measurements are included and z_k is the measurement and in this case, it will be equal to average phase error which is the output of the carrier loop discriminator during the integration time T. $\left[z_k - H_k \hat{x}_k^- \right]$ is named as residuals and it shows the discrepancy between the measurements and estimates. P_k is posteriori error covariance matrix.

The process noise covariance matrix Q_k and the measurement noise covariance matrix R_k should be set carefully in the KF design [230]. The process noise covariance matrix is related to the process noise ω_k, and can be modelled as

$$\omega_k = \begin{bmatrix} \omega_{bias} & \omega_{drift} & \omega_{accel} \end{bmatrix}_k \tag{A.13}$$

where ω_{bias}, ω_{drift} and ω_{accel} are zero mean white noises ($\omega_k \sim N\left(0, Q_k\right)$) with the power spectral densities S_{bias}, S_{drift} and S_{accel}, respectively:

$$S_{bias} = \frac{h_0}{2} \tag{A.14}$$

$$S_{drift} = 2\pi^2 h_{-2} \tag{A.15}$$

that depend on the h_0 and h_{-2} Allan variance (AV) coefficients for timing standards (e.g. TCXO, OCXO, Rubidium, Cesium) and S_{accel} can be determined by the LOS jerk [229]. Process noise covariance matrix is computed as:

$$Q = \mathrm{E}\left[G \omega \omega^T G^T \right] = \begin{bmatrix} f_{RF}^2 S_{bias} & 0 & 0 \\ 0 & f_{RF}^2 S_{drift} & 0 \\ 0 & 0 & \frac{f_{RF}^2 S_{accel}}{c^2} \end{bmatrix} \tag{A.16}$$

$$Q_k \approx \frac{1}{2}\left[A_k\, Q + Q\, A_k^T\right]\, T \tag{A.17}$$

Furthermore, the measurement noise covariance matrix R_k is the noise variance of v_k, which is a zero-mean white noise, and is computed as:

$$R_k = \mathrm{E}\left[v_k v_k^T\right] = \sigma_v^2 = \frac{1}{2\,C/N_0}\left(1 + \frac{1}{2\,C/N_0\,T}\right) \tag{A.18}$$

Appendix B

Support Vector Machines (SVM) Algorithm

B.1 Derivation of the Optimum Hyper-plane

With the given input data-set $\{x_1, x_2, ..., x_N\}$ where $x_i \in R^n$, the two-class data classification problem using linear models are written in the following form [196]:

$$y_i = f(x_i) = \omega_0^T x_i + b_0 \tag{B.1}$$

where $\omega_0^T x$ corresponds to the projection of x over the direction spanned by ω_0. ω_0 and b_0 are parameters of the optimum hyperplane [188]. Corresponding target values $\{t_1, t_2, ..., t_N\}$ to the input values are decided according to y_i:

$$class(x_i) = \begin{cases} C_1, & \omega_0^T x_i \geq -b_0 \quad \rightarrow \quad t_i = +1 \\ C_2, & \omega_0^T x_i < -b_0 \quad \rightarrow \quad t_i = -1 \end{cases} \tag{B.2}$$

where $t_i \in \{-1, +1\}$ defines the class labels. If all the points are classified correctly, it leads to $t_i y_i > 0$ for all i. The distance of x_i from the hyperplane is computed as [231]

$$d(x_i) = \frac{|f(x_i)|}{\|\omega\|} = \frac{t_i \left(\omega_0^T x_i + b_0\right)}{\|\omega\|} \tag{B.3}$$

Up to this point, there are not enough constraints to fix specific values for b and ω. Therefore, in order to define a decision rule and have an optimum hyper-plane, the parameters should be optimized by considering the maximum width for the margin that can be obtained by solving [196]

$$\arg\max_{\omega_0, b_0} = \left\{ \frac{1}{\|\omega\|} \min_i \left[t_i \left(w^T x_i + b \right) \right] \right\} \tag{B.4}$$

The direct optimization problem would be very complex and this constrained optimization problem is solved by using Lagrange Multipliers [196]. The cost function is written as

$$L = \frac{1}{2}\|\omega\|^2 - \sum_{i=1}^{N} a_i \left\{ t_i \left(\omega^T x_i + b \right) - 1 \right\} \tag{B.5}$$

where $a = (a_1, a_2, ...a_N)^T$ are Lagrangian multipliers with $a_i \geq 0$. The solutions are saddle points of the cost function L. There is a minus sign before the multipliers, because saddle points are obtained by minimizing with respect to ω and b and maximizing with respect to a [196, 188]. The derivatives of the cost function with respect to ω and b are then set to zero:

$$\frac{\partial L}{\partial \omega} = 0 \rightarrow \omega_0 = \sum_{i=1}^{N} \alpha_i t_i x_i \tag{B.6}$$

$$\frac{\partial L}{\partial b} = 0 \rightarrow \sum_{i=1}^{N} \alpha_i t_i = 0 \tag{B.7}$$

Replacing (B.6) and (B.7) in (B.5) leads to the dual representation of the maximum margin problem [196]

$$\tilde{L}(a) = \sum_{i=1}^{N} a_i - \frac{1}{2} \sum_{i=1}^{N} \sum_{j=1}^{N} a_i a_j t_i t_j \kappa(x_i, x_j) \quad \text{subject to} \tag{B.8}$$

$$a_i \geq 0, \quad i = 1, ..., N \tag{B.9}$$

where $\kappa(x_i, x_j) = x_i^T x_j$ is kernel function. A necessary and sufficient condition for a function $\kappa(x_i, x_j)$ to be a valid kernel, the function $\kappa(x_i, x_j)$ should be positive semi-definite for all the possible choices and this also ensures that the Lagrangian function $\tilde{L}(a)$ is bounded [196]. The Lagrange multipliers are obtained by solving

$$\hat{a} = \arg\max_{a} \tilde{L}(a) \tag{B.10}$$

with respect to a subject to the constraints

$$\hat{a} \geq 0, i = 1,2, ..., N \tag{B.11}$$

$$\sum_{i=1}^{N} \hat{a}_i ti = 0 \tag{B.12}$$

where all the points which have $\hat{a} \neq 0$ are on the margin, in other words they are support vectors [191]. For all the points that do not lie on the margin, the corresponding Lagrange multiplier is $\hat{a} = 0$. Now, y_i, defined by (B.1), can be evaluated as

$$y_i = f(x_i) = \sum_{j=1}^{N} \hat{a}_j t_j \kappa(x_i, x_j) + b \tag{B.13}$$

The optimization of this form satisfies the following Karush-Kuhn-Tucker (KKT) conditions which are both necessary and sufficient for optimum SVM solution [195, 196, 231]:

$$\begin{aligned} \hat{\alpha}_i &\geq 0, \ \forall i \\ t_i y_i - 1 &\geq 0, \ \forall i \\ \hat{\alpha}_i \left\{ t_i y_i - 1 \right\} &= 0, \ \forall i \end{aligned} \tag{B.14}$$

After obtaining the Lagrange multipliers $\hat{a}$ by solving (B.10), the optimal parameters w_0 and b_0 can be computed by considering the set of support vectors S. Because, any data point for which $\hat{a} = 0$ plays no role in making predictions for the new data points. Having obtained the $\hat{a}$ and support vector x_i values that satisfy KKT conditions and (B.13), the value of the threshold parameter b can be determined [196]

$$w_0 = \sum_{i \epsilon S} \hat{a}_i t_i x_i \tag{B.15}$$

and

$$b_0 = \frac{1}{N_S} \sum_{i \epsilon S} \left(t_i - \sum_{j \epsilon S} \hat{a}_j t_j \kappa(x_i, x_j) \right) \tag{B.16}$$

where N_S is the total number of support vectors in the set S and averaging over all support vectors provides a numerically more stable solution for b_0 [196]. Eventually, the decision function of SVM is computed as

$$\hat{y}(x_i) = \text{sign} \left(\sum_{j=1}^{N_s} \left[\hat{a}_i t_i \kappa(x_j, x_i) \right] + b_0 \right) \tag{B.17}$$

Bibliography

[1] P. Enge. *GPS Modernization: Capabilities of the New Civil Signals*. Paper presented at the meeting of 10th Australian International Aerospace Congress, Brisbane, Australia. 2003. URL: http://web.stanford.edu/group/scpnt/gpslab/pubs/papers/Enge_AIAC_2003.pdf.

[2] S. Söderholm et al. "A Multi-GNSS Software-Defined Receiver: Design, Implementation, and Performance Benefits". In: *Annnals of Telecommunications* 71.7-8 (Aug. 2016), pp. 399–410.

[3] E. Kaplan and C. Hegarty. *Understanding GPS: Principles and Applications*. 2nd Ed. 685 Canton Street Norwood, MA 02062: Artech House, Inc., 2006.

[4] S. Priyadarshi. "A Review of Ionospheric Scintillation Models". In: *Survey in Geophysics* 36.2 (Jan. 2015), pp. 295–324.

[5] R. K. Crane. "Ionospheric Scintillation". In: *Proceedings of the IEEE* 65.2 (Feb. 1977), pp. 180–199.

[6] N. Linty et al. "Detection of GNSS Ionospheric Scintillations Based on Machine Learning Decision Tree". In: *IEEE Transactions on Aerospace and Electronic Systems* 55.1 (Feb. 2019), pp. 303–317.

[7] P. D. Groves. *GNSS Solutions: Multipath vs. NLOS signals. How does non-line-of-sight reception differ from multipath interference?* Inside GNSS. Nov.–Dec. 2013. URL: https://insidegnss-com.exactdn.com/wp-content/uploads/2018/01/novdec13-Solutions.pdf.

[8] D. Akos. "A Software Radio Approach to Global Navigation Satellite System Receiver Design". PhD thesis. OH, USA: Fritz J., Dolores H. Russ College of Engineering, and Technology, Ohio University, Aug. 1997.

[9] C. L. Rino. *The Theory of Scintillation with Applications in Remote Sensing*. Hoboken, New Jersey: John Wiley & Sons, Inc. - IEEE Press, 2011.

[10] C. Savas and F. Dovis. "The Impact of Different Kernel Functions on the Performance of Scintillation Detection Based on Support Vector Machines". In: *Sensors* 19.23 (Nov. 2019), p. 5219.

[11] C. Savas, G. Falco, and F. Dovis. "A Comparative Performance Analysis of GPS L1 C/A, L5 Acquisition and Tracking Stages under Polar and Equatorial Scintillations". In: *IEEE Transactions on Aerospace and Electronic Systems* (2020), pp. 1–1.

[12] C. Savas and F. Dovis. "Multipath Detection based on K-means Clustering". In: *32nd International Technical Meeting of the Satellite Division of The Institute of Navigation (ION GNSS+ 2019)*. Miami, Florida, USA, Sept. 2019, pp. 3801–3811.

[13] C. Savas, F. Dovis, and G. Falco. "Performance Evaluation and Comparison of GPS L5 Acquisition Methods under Scintillations". In: *31st International Technical Meeting of The Satellite Division of the Institute of Navigation (ION GNSS+ 2018)*. Miami, Florida, USA, Sept. 2018, pp. 3596–3610.

[14] C. Savas, G. Falco, and F. Dovis. "A Comparative Analysis of Polar and Equatorial Scintillation Effects on GPS L1 and L5 Tracking Loops". In: *2019 International Technical Meeting of The Institute of Navigation*. Reston, Virginia, USA, Jan. 2019, pp. 632–646.

[15] C. Savas and F. Dovis. "Comparative Performance Study of Linear and Gaussian Kernel SVM Implementations for Phase Scintillation Detection". In: *2019 International Conference on Localization and GNSS (ICL-GNSS)*. Nuremberg, Germany, June 2019, pp. 1–6.

[16] H. Ghobadi et al. "A Comparative Study of Different Phase Detrending Algorithms for Scintillation Monitoring". In: *2020 XXXIIIrd General Assembly and Scientific Symposium of the International Union of Radio Science*. Rome, Italy, Oct. 2020, pp. 1–4.

[17] F. Dovis et al. "Opportunistic Use of GNSS Signals to Characterize the Environment by Means of Machine Learning Based Processing". In: *ICASSP 2020 - 2020 IEEE International Conference on Acoustics, Speech and Signal Processing (ICASSP)*. Barcelona, Spain, May 2020, pp. 9190–9194.

[18] P. D. Groves. *Principles of GNSS, Inertial, and Multisensor Integrated Navigation Systems*. 2nd Ed. 16 Sussex Street London SW1V 4RW, UK: Artech House, 2013.

[19] S. Revnivykh et al. "GLONASS". In: *Springer Handbook of Global Navigation Satellite Systems*. Ed. by Peter J. G. Teunissen and O. Montenbruck. Gewerbestrasse 11, 6330 Cham, Switzerland: Springer International Publishing AG, 2017. Chap. 8, pp. 219–246.

[20] European GNSS Service Centre - Constellation Information. European Global Navigation Satellite Systems Agency (GSA). URL: https://www.gsc-europa.eu/system-service-status/constellation-information.

[21] Y. Yang, J. Tang, and O. Montenbruck. "Chinese Navigation Satellite Systems". In: *Springer Handbook of Global Navigation Satellite Systems*. Ed. by Peter J. G. Teunissen and O. Montenbruck. Gewerbestrasse 11, 6330 Cham, Switzerland: Springer International Publishing AG, 2017. Chap. 10, pp. 273–304.

[22] Official Signal in Space Interface Control Documents (ICDs). BeiDou Navigation Satellite System (BDS). URL: http://en.beidou.gov.cn/SYSTEMS/ICD/.

[23] Official Signal in Space Interface Control Document (ICD). European GNSS (GALILEO) Open Service. URL: https://www.gsc-europa.eu/sites/default/files/sites/all/files/Galileo-OS-SIS-ICD.pdf.

[24] C. J. Hegarty. "The Global Positioning System (GPS)". In: *Springer Handbook of Global Navigation Satellite Systems*. Ed. by Peter J. G. Teunissen and O. Montenbruck. Gewerbestrasse 11, 6330 Cham, Switzerland: Springer International Publishing AG, 2017. Chap. 7, pp. 197–218.

[25] M. Falcone, J. Hahn, and T. Burger. "Galileo". In: *Springer Handbook of Global Navigation Satellite Systems*. Ed. by Peter J. G. Teunissen and O. Montenbruck. Gewerbestrasse 11, 6330 Cham, Switzerland: Springer International Publishing AG, 2017. Chap. 9, pp. 247–272.

[26] E. Kaplan and C. Hegarty. *Understanding GPS: Principles and Applications*. 3rd Ed. Nordwood, MA: Artech House, Inc., 2017.

[27] M. Pratap and P. Enge. *Global Positioning System: Signals, Measurements, and Performance*. 2nd Ed. Lincoln, Massachusetts, USA: Ganga-Jamuna Press, 2011.

[28] B. Hofmann-Wellenhof, H. Lichtenegger, and J. Collins. *Global Positioning System Theory and Practice*. 1st Ed. Wien, Austria: Springer-Verlag, 1992.

[29] M. S. Grewal, L. R. Weill, and A. P. Andrews. *Global Positioning Systems, Inertial Navigaion, and Integration*. New York, NY, USA: John Wiley and Sons, Inc., 2001.

[30] R. B. Langley, P. J. G. Teunissen, and O. Montenbruck. "Introduction to GNSS". In: *Springer Handbook of Global Navigation Satellite Systems*. Ed. by Peter J. G. Teunissen and O. Montenbruck. Gewerbestrasse 11, 6330 Cham, Switzerland: Springer International Publishing AG, 2017. Chap. 1, pp. 3–23.

[31] J. J. Jr. Spilker and B. W. Parkinson. "Overview of GPS Operation and Design". In: *Global Positioning System: Theory and Applications, Volume I*. Ed. by J. J. Spilker Jr. et al. 370 L'Enfant Promenade, SW, Washington, DC: American Institute of Aeronautics and Astronautics, Inc., 1996. Chap. 2, pp. 29–56.

[32] Guenter W. Hein. *Multi-Frequency Multi-System GNSS and SBAS*. Lecture Notes in International Summer School on GNSS 2018. Loipersdorf, Austria: ESA/JRC, July 2018.

[33] K. Borre et al. *A Software-defined GPS and Galileo Receiver. A Single-frequency Approach*. Ed. by J. J. Benedetto. Applied and Numerical Harmonic Analysis. Boston, MA, USA: Birkhäuser, 2007.

[34] A. Ucar. "A Subsampling Delta-sigma Modulator for Global Navigation Satellite Systems". PhD thesis. London, UK: University of Westminster School of Electronics and Computer Science, Nov. 2010.

[35] Official U.S. government information about the Global Positioning System (GPS) and related topics. National Coordination Office for Space-Based Positioning, Navigation, and Timing. URL: https://www.gps.gov/systems/gps/modernization/civilsignals/.

[36] Official GLONASS Interface Control Documents (ICDs). Russian Space Systems, JSC. URL: http://russianspacesystems.ru/bussines/navigation/glonass/interfeysnyy-kontrolnyy-dokument/.

[37] GPS Directorate Systems Engineering and Integration. *IS-GPS-705D Navstar GPS Space Segment/User Segment L5 Interfaces Document*. Sept. 2013. URL: https://www.gps.gov/technical/icwg/IS-GPS-705D.pdf.

[38] S. J. Hrbek, D. H. Won, and D. M. Akos. "Power Characterization for L1 and L5 Transmissions". In: *2016 International Technical Meeting of The Institute of Navigation*. Monterey, California, USA, Jan. 2016, pp. 873–880.

[39] J. W. Betz. "Binary Offset Carrier Modulations for Radionavigation". In: *NAVIGATION* 48.4 (2001), pp. 227–246.

[40] R. Romero et al. "On the Use and Performance of New Galileo Signals for Ionospheric Scintillation Monitoring over Antarctica". In: *2017 International Technical Meeting of The Institute of Navigation*. Monterey, California, USA, Jan. 2017, pp. 989–997.

[41] B. Eissfeller and J.-H. Won. "Receiver Architecture". In: *Springer Handbook of Global Navigation Satellite Systems*. Ed. by Peter J. G. Teunissen and O. Montenbruck. Gewerbestrasse 11, 6330 Cham, Switzerland: Springer International Publishing AG, 2017. Chap. 13, pp. 365–400.

[42] C. Mongrédien, G. Lachapelle, and M. E. Cannon. "Testing GPS L5 Acquisition and Tracking Algorithms Using a Hardware Simulator". In: *19th International Technical Meeting of the Satellite Division of The Institute of Navigation (ION GNSS 2006)*. Fort Worth, TX, USA, Sept. 2006, pp. 2901–2913.

[43] J.-H. Won and T. Pany. "Signal Processing". In: *Springer Handbook of Global Navigation Satellite Systems*. Ed. by Peter J. G. Teunissen and O. Montenbruck. Gewerbestrasse 11, 6330 Cham, Switzerland: Springer International Publishing AG, 2017. Chap. 14, pp. 401–442.

[44] J. Qi and P. Song. "Research on The Bit Synchronization Algorithm and Multiplexing Technology in GNSS Receiver". In: *China Communications* 11.14 (2014), pp. 30–36.

[45] D. Olesen, J. Jakobsen, and P. Knudsen. *Are there low-cost and low-weight options for GNSS IF storage?* Inside GNSS. Sept.–Oct. 2016. URL: https://insidegnss-com.exactdn.com/wp-content/uploads/2018/01/sepoct16-SOLUTIONS.pdf.

[46] MATLAB. *version 9.1.0.441655 (R2016b)*. Natick, Massachusetts: The MathWorks Inc., 2016.

[47] C. Cristodaro et al. "Design of a Configurable Monitoring Station for Scintillations by Means of a GNSS Software Radio Receiver". In: *IEEE Geoscience and Remote Sensing Letters* 15.3 (Mar. 2018), pp. 325–329.

[48] D. Sinha, A. K. Verma, and S. Kumar. "Software Defined Radio: Operation, Challenges and Possible Solutions". In: *10th International Conference on Intelligent Systems and Control (ISCO)*. Jan. 2016, pp. 1–5.

[49] J. Mitola. "Software Radios: Survey, Critical Evaluation and Future Directions". In: *IEEE Aerospace and Electronic Systems Magazine* 8.4 (Apr. 1993), pp. 25–36.

[50] J. Mitola. "The Software Radio Architecture". In: *IEEE Communications Magazine* 33.5 (May 1995), pp. 26–38.

[51] L. L. Presti et al. "Software Defined Radio technology for GNSS receivers". In: *2014 IEEE Metrology for Aerospace (MetroAeroSpace)*. May 2014, pp. 314–319.

[52] G. Strang and K. Borre. *Linear Algebra, Geodesy, and GPS*. Wellesley MA 02181 USA: Wellesley-Cambridge Press, 1997.

[53] NovAtel Inc. *An Introduction to GNSS*. 2nd Ed. Calgary, Alberta, Canada: NovAtel Inc., 2015. URL: https://novatel.com/an-introduction-to-gnss.

[54] B. W. Parkinson. "GPS Error Analysis". In: *Global Positioning System: Theory and Applications, Volume I*. Ed. by J. J. Spilker Jr. et al. 370 L'Enfant Promenade, SW, Washington, DC: American Institute of Aeronautics and Astronautics, Inc., 1996. Chap. 11, pp. 469–484.

[55] P. M. Kintner, T. E. Humphreys, and J. C. Hinks. *GNSS and Ionospheric Scintillation – How to Survive the Next Solar Maximum*. Inside GNSS. July–Aug. 2009. URL: https://www.insidegnss.com/auto/julyaug09-kintner.pdf.

[56] A. J. Van Dierendonck, J. Klobuchar, and Q. Hua. "Ionospheric Scintillation Monitoring Using Commercial Single Frequency C/A Code Receivers". In: *6th International Technical Meeting of the Satellite Division of The Institute of Navigation (ION GPS 1993)*. Salt Lake City, UT, USA, Sept. 1993, pp. 1333–1342.

[57] J. Vilà-Valls et al. "Survey on signal processing for GNSS under ionospheric scintillation: Detection, monitoring, and mitigation". In: *NAVIGATION* 67.3 (Sept. 2020), pp. 511–536.

[58] A. O. Adewale et al. "A Study of L-band Scintillations and Total Electron Content at An Equatorial Station, Lagos, Nigeria". In: *Radio Science* 47.02 (2012), pp. 1–12.

[59] Y. Jiao et al. "Characterization of High-Latitude Ionospheric Scintillation of GPS Signals". In: *Radio Science* 48.6 (2013), pp. 698–708.

[60] G. D'Angelo et al. "GNSS Data Filtering Optimization for Ionospheric Observation". In: *Advances in Space Research* 56.11 (2015), pp. 2552–2562.

[61] S. C. Mushini et al. "Improved Amplitude- and Phase-Scintillation Indices Derived from Wavelet Detrended High-Latitude GPS Data". In: *GPS Solutions* 16 (July 2012), pp. 363–373.

[62] M. Najmafshar, S. Skone, and S. Ghafoori. "GNSS Data Processing Investigations for Characterizing Ionospheric Scintillation". In: *27th International Technical Meeting of the Satellite Division of The Institute of Navigation (ION GNSS+ 2014)*. Tampa, Florida, USA, Sept. 2014, pp. 1190–1202.

[63] F. Ghafoori and S. Skone. "Impact of Equatorial Ionospheric Irregularities on GNSS Receivers Using Real and Synthetic Scintillation Signals". In: *Radio Science* 50.4 (May 2015), pp. 294–317.

[64] J. T. Curran et al. *Developing an Ionospheric Scintillation Monitoring Receiver*. Inside GNSS. Sept.–Oct. 2014. URL: https://insidegnss.com/developing-an-ionospheric-scintillation-monitoring-receiver/.

[65] N. Linty, F. Dovis, and L. Alfonsi. "Software-defined Radio Technology for GNSS Scintillation Analysis: Bring Antarctica to the Lab". In: *GPS Solutions* 22.4 (Oct. 2018).

[66] J. T. Curran et al. "Developing a Multi-Frequency for GNSS-Based Scintillation Monitoring Receiver". In: *27th International Technical Meeting of the Satellite Division of The Institute of Navigation (ION GNSS+ 2014)*. Tampa, Florida, USA, Sept. 2014, pp. 1142–1152.

[67] S. Peng and Y. Morton. "A USRP2-based Reconfigurable Multi-constellation Multi-frequency GNSS Software Receiver Front End". In: *GPS Solutions* 17.1 (Jan. 2013), pp. 89–102.

[68] N. Linty et al. "Benefits of GNSS Software Receivers for Ionospheric Monitoring at High Latitudes". In: *2015 1st URSI Atlantic Radio Science Conference (URSI AT-RASC)*. Las Palmas, Spain, May 2015, pp. 1–6.

[69] L. Alfonsi et al. "First Observations of GNSS Ionospheric Scintillations From DemoGRAPE Project". In: *Space Weather* 14.10 (Oct. 2016), pp. 704–709.

[70] K. S. Jacobsen and M. Dähnn. "Statistics of Ionospheric Disturbances and Their Correlation with GNSS Positioning Errors at High Latitudes". In: *J. Space Weather Space Clim.* 4 (Sept. 2014), A27.

[71] Y. Jiao, Y. Morton, and S. Taylor. "Comparative Studies of High-latitude and Equatorial Ionospheric Scintillation Characteristics of GPS Signals". In: *2014 IEEE/ION Position, Location and Navigation Symposium - PLANS 2014*. Monterey, CA, USA, May 2014, pp. 37–42.

[72] V. I. Tatarskii. *Effects of the Turbulent Atmosphere on Wave Propagation*. Tech. rep. Springfield, VA 22161: US Department of Commerce National Technical Information Service, 1971. URL: https://ntrl.ntis.gov/NTRL/dashboard/searchResults/titleDetail/TT6850464.xhtml.

[73] K. C. Yeh and C.-H. Liu. "Radio Wave Scintillations in The Ionosphere". In: *Proceedings of the IEEE* 70.4 (Apr. 1982), pp. 324–360.

[74] M. Grzesiak et al. "Regional Short-Term Forecasting of Ionospheric TEC and Scintillation". In: *Radio Science* 53.10 (Oct. 2018), pp. 1254–1268.

[75] E. J. Fremouw and C. L. Rino. "An Empirical Model for Average F-layer Scintillation at VHF/UHF". In: *Radio Science* 8.3 (Mar. 1973), pp. 213–222.

[76] J. Aarons. "Construction of A Model of Equatorial Scintillation Intensity". In: *Radio Science* 20.3 (June 1985), pp. 397–402.

[77] S. J. Franke and C. H. Liu. "Modeling of Equatorial Multifrequency Scintillation". In: *Radio Science* 20.3 (June 1985), pp. 403–415.

[78] J. M. Retterer. "Forecasting Low-latitude Radio Scintillation with 3-D Ionospheric Plume Models: 2. Scintillation Calculation". In: *Journal of Geophysical Research: Space Physics* 115.A3 (Mar. 2010).

[79] K. N. Iyer et al. "A Model of Equatorial and Low Latitude VHF Scintillation in India". In: *Indian Journal of Radio and Space Physics* 35 (Apr. 2006), pp. 98–104.

[80] S. Basu, S. Basu, and B. K. Khan. "Model of equatorial scintillations from in-situ measurements". In: *Radio Science* 11.10 (Oct. 1976), pp. 821–832.

[81] A. W. Wernik, L. Alfonsi, and M. Materassi. "Scintillation Modeling Using In Situ Data". In: *Radio Science* 42.1 (Feb. 2007).

[82] D. Bilitza. "International Reference Ionosphere—Status 1995/96". In: *Advances in Space Research* 20.9 (1997), pp. 1751–1754.

[83] C. L. Rino. "A Power Law Phase Screen Model for Ionospheric Scintillation: 1. Weak scatter". In: *Radio Science* 14.6 (1979), pp. 1135–1145.

[84] NorthWest Research Associates, Inc. Accessed Jan. 10, 2021. Space Weather Services. URL: https://spawx.nwra.com/spawx/.

[85] NASA - Community Coordinated Modeling Center. Accessed Jan. 10, 2021. WBMOD Ionospheric Scintillation Model. URL: https://ccmc.gsfc.nasa.gov/modelweb/ionos/wbmod.html/.

[86] E. J. Fremouw and J. A. Secan. "Modeling and Scientific Application of Scintillation Results". In: *Radio Science* 19.3 (June 1984), pp. 687–694.

[87] A.W. Wernik, J.A. Secan, and E.J. Fremouw. "Ionospheric Irregularities and Scintillation". In: *Advances in Space Research* 31.4 (2003), pp. 971–981.

[88] Y. Béniguel and S. Buonomo. "A Multiple Phase Screen Ionospheric Propagation Model to Estimate the Fluctuations of Transmitted Signals". In: *Physics and Chemistry of the Earth, Part C: Solar, Terrestrial and Planetary Science* 24.4 (1999), pp. 333–338.

[89] Y. Béniguel. "Global Ionospheric Propagation Model (GIM): A Propagation Model for Scintillations of Transmitted Signals". In: *Radio Science* 37.3 (2002), pp. 4-1 –4-13.

[90] S. M. Radicella. "The NeQuick Model Genesis, Uses and Evolution". In: *Annals of Geophysics* 52.3-4 (2009), pp. 417–422. URL: https://www.annalsofgeophysics.eu/index.php/annals/article/view/4597.

[91] Y. Béniguel. Accessed on Jan. 15, 2021. Global Ionospheric Propagation Model. GISM User Manual. release n. 6.53, Jan. 2011. URL: http://www.ieea.fr/help/gism-user-manual.pdf/.

[92] B. Forte and S. M. Radicella. "Comparison of Ionospheric Scintillation Models with Experimental Data for Satellite Navigation Applications". In: *Annals of Geophysics* 48.3 (June 2005).

[93] T. E. Humphreys et al. "Simulating Ionosphere-Induced Scintillation for Testing GPS Receiver Phase Tracking Loops". In: *IEEE Journal of Selected Topics in Signal Processing* 3.4 (2009), pp. 707–715.

[94] T. E. Humphreys et al. "Data-Driven Testbed for Evaluating GPS Carrier Tracking Loops in Ionospheric Scintillation". In: *IEEE Transactions on Aerospace and Electronic Systems* 46.4 (2010), pp. 1609–1623.

[95] M. Aquino et al. *The Implementation of the Cornell Ionospheric Scintillation Model into the Spirent GNSS Simulator*. Accessed on Jan. 15, 2021. The University of Nottingham - Institute of Engineering Surveying and Space Geodesy (IESSG). 2010. URL: https://radionavlab.ae.utexas.edu/images/stories/files/presentations/tm_iono_scint_2010.pptx.

[96] V. V. Sreeja et al. "Tackling Ionospheric Scintillation Threat to GNSS in Latin America". In: *J. Space Weather Space Clim.* 1.1 (2011), A05.

[97] J. Vila-Valls et al. "Are PLLs Dead? A Tutorial on Kalman Filter-based Techniques for Digital Carrier Synchronization". In: *IEEE Aerospace and Electronic Systems Magazine* 32.7 (July 2017), pp. 28–45.

[98] R. Yang et al. "Generalized GNSS Signal Carrier Tracking: Part I - Modeling and Analysis". In: *IEEE Transactions on Aerospace and Electronic Systems* 53.4 (Aug. 2017), pp. 1781–1797.

[99] J.-H. Won, D. Dötterböck, and B. Eissfeller. "Performance Comparison of Different Forms of Kalman Filter Approaches for a Vector-Based GNSS Signal Tracking Loop". In: *NAVIGATION* 57.3 (Aug. 2014), pp. 185–199.

[100] X. Tang et al. "Theoretical Analysis and Tuning Criteria of the Kalman Filter-based Tracking Loop". In: *GPS Solutions* 19 (July 2015), pp. 489–503.

[101] M. Susi et al. "Design of a Robust Receiver Architecture for Scintillation Monitoring". In: *2014 IEEE/ION Position, Location and Navigation Symposium - PLANS 2014*. Monterey, CA, USA, May 2014, pp. 73–81.

[102] L. Zhang, Y. T.Morton, and M. M. Miller. "A Variable Gain Adaptive Kalman Filter-Based GPS Carrier Tracking Algorithm for Ionosphere Scintillation Signals". In: *23rd International Technical Meeting of the Satellite Division of The Institute of Navigation (ION GNSS 2010)*. Portland, OR, USA, Sept. 2010, pp. 3107–3114.

[103] J. H. Won et al. "Advanced Signal Processing Scheme for GNSS Receivers Under Ionospheric Scintillation". In: *Proceedings of the 2012 IEEE/ION Position, Location and Navigation Symposium*. Myrtle Beach, SC, USA, Apr. 2012, pp. 44–49.

[104] T. E. Humphreys et al. "GPS Carrier Tracking Loop Performance in the Presence of Ionospheric Scintillations". In: *18th International Technical Meeting of the Satellite Division of The Institute of Navigation (ION GNSS 2005)*. Long Beach, CA, USA, Sept. 2005, pp. 156–167.

[105] J. Vilà-Valls, P. Closas, and C. Fernández-Prades. "Advanced KF-based Methods for GNSS Carrier Tracking and Ionospheric Scintillation Mitigation". In: *2015 IEEE Aerospace Conference*. Big Sky, MT, USA, Mar. 2015, pp. 1–10.

[106] V. Barreau et al. “Kalman Filter based robust GNSS signal tracking algorithm in presence of ionospheric scintillations”. In: *2012 6th ESA Workshop on Satellite Navigation Technologies (Navitec 2012) and European Workshop on GNSS Signals and Signal Processing*. Noordwijk, Netherlands, Dec. 2012, pp. 1–8.

[107] A. Ferrario et al. “Improvement of a High-Grade GNSS Receiver Robustness Against Ionospheric Scintillations Using a Kalman Filter Tracking Scheme”. In: *28th International Technical Meeting of the Satellite Division of The Institute of Navigation (ION GNSS+ 2015)*. Tampa, Florida, USA, Sept. 2015, pp. 3116–3126.

[108] J. A. Secan et al. “High-latitude Upgrade to the Wideband Ionospheric Scintillation Model”. In: *Radio Science* 32.4 (July 1997), pp. 1567–1574.

[109] R. Tiwari et al. “WBMod Assisted PLL GPS Software Receiver for Mitigating Scintillation Affect in High Latitude Region”. In: *2011 XXXth URSI General Assembly and Scientific Symposium*. Istanbul, Turkey, Aug. 2011, pp. 1–4.

[110] J. O. Olwendo et al. “Elimination of Superimposed Multipath Effects on Scintillations Index on Solar Quite Ionosphere at Low Latitude Over the Kenyan Airspace from a Lone Positioned SCINDA System”. In: *23rd International Technical Meeting of the Satellite Division of The Institute of Navigation (ION GNSS 2010)*. Portland, OR, USA, Sept. 2010, pp. 386–392.

[111] W. Pelgrum et al. “Measurement and Analysis of Artificially-Generated and Natural Ionosphere Scintillations Effects on GNSS Signals”. In: *2011 International Technical Meeting of The Institute of Navigation*. San Diego, CA, USA, Jan. 2011, pp. 950–958.

[112] V. Praveen. “Event Driven GPS Data Collection System for Studying Ionospheric Scintillation”. MA thesis. Oxford, OH, USA: Department of Electrical and Computer Engineering, Miami University, 2011. URL: http://rave.ohiolink.edu/etdc/view?acc_num=miami1323894410.

[113] W. Fu et al. “Real-Time Ionospheric Scintillation Monitoring”. In: *12th International Technical Meeting of the Satellite Division of The Institute of Navigation (ION GPS 1999)*. Nashville, TN, USA, Sept. 1999, pp. 1461–1472.

[114] M. Materassi and C. N. Mitchell. “Wavelet Analysis of GPS Amplitude Scintillation: A Case Study”. In: *Radio Science* 42.1 (2007).

[115] N. Linty and F. Dovis. “An Open-Loop Receiver Architecture for Monitoring of Ionospheric Scintillations by Means of GNSS Signals”. In: *Applied Sciences* 9.12 (June 2019).

[116] R. Romero et al. "A Novel Approach to Ionospheric Scintillation Detection Based on An Open Loop Architecture". In: *2016 8th ESA Workshop on Satellite Navigation Technologies and European Workshop on GNSS Signals and Signal Processing (NAVITEC)*. 2016, pp. 1–9.

[117] M. Irsigler. "Multipath Propagation, Mitigation and Monitoring in the Light of Galileo and the Modernized GPS". PhD thesis. Munich: Universitat der Bundeswehr, Jan. 2008.

[118] Q.-H. Phan et al. "A Unified Framework for GPS Code and Carrier-Phase Multipath Mitigation Using Support Vector Regression". In: *Advances in Artificial Neural Systems* 2013 (Mar. 2013).

[119] J. Van Sickle. *GPS for Land Surveyors*. 3rd Ed. Boca Raton, FL, USA: CRC Press, 2008.

[120] P. D. Groves et al. "A Portfolio Approach to NLOS and Multipath Mitigation in Dense Urban Areas". In: *26th International Technical Meeting of the Satellite Division of The Institute of Navigation (ION GNSS+ 2013)*. Nashville, TN, USA, Sept. 2013, pp. 3231–3247.

[121] GPS Yuma Almanacs. Accessed Oct. 1, 2020. CelesTrak. URL: https://celestrak.com/GPS/almanac/Yuma/.

[122] F. G. Nievinski and K. M. Larson. "An Open Source GPS Multipath Simulator in Matlab/Octave". In: *GPS Solutions* 18.3 (July 2014), pp. 473–481.

[123] N. I. Ziedan. "Improved Multipath and NLOS Signals Identification in Urban Environments". In: *NAVIGATION* 65.3 (Sept. 2018), pp. 449–462.

[124] R. D. J. Van Nee. "The Multipath Estimating Delay Lock Loop". In: *IEEE Second International Symposium on Spread Spectrum Techniques and Applications*. Yokohama, Japan, Nov.–Dec. 1992, pp. 39–42.

[125] L. R. Weill. "Multipath Mitigation using Modernized GPS Signals: How Good Can it Get?" In: *15th International Technical Meeting of the Satellite Division of The Institute of Navigation (ION GPS 2002)*. Portland, OR, USA, Sept. 2002, pp. 493–505.

[126] P. C. Fenton and J. Jones. "The Theory and Performance of NovAtel Inc.'s Vision Correlator". In: *18th International Technical Meeting of the Satellite Division of The Institute of Navigation (ION GNSS 2005)*. Long Beach, CA, USA, Sept. 2005, pp. 2178–2186.

[127] X. Chen et al. "Comparative Studies of GPS Multipath Mitigation Methods Performance". In: *IEEE Transactions on Aerospace and Electronic Systems* 49.3 (2013), pp. 1555–1568.

[128] R. G. Brown and G. Y. Chin. "GPS RAIM: Calculation of Threshold and Protection Radius Using Chi-square Methods—A Geometric Approach". In: *Global Positioning System: Institute of Navigation GPS Red Books*. Vol. 5. Manassas, VA, USA: NAVIGATION, 1998, pp. 155–179.

[129] R. G. Brown. "Receiver Autonomous Integrity Monitoring". In: *Global Positioning System: Theory and Applications, Volume II*. Ed. by B. W. Parkinson and J. J. Spilker Jr. 370 L'Enfant Promenade, SW, Washington, DC: American Institute of Aeronautics and Astronautics, Inc., 1996. Chap. 5, pp. 143–165.

[130] T. Iwase, N. Suzuki, and Y. Watanabe. "Estimation and Exclusion of Multipath Range Error for Robust Positioning". In: *GPS Solutions* 17.1 (Jan. 2013), pp. 53–62.

[131] Z. Jiang et al. "Multi-Constellation GNSS Multipath Mitigation Using Consistency Checking". In: *24th International Technical Meeting of the Satellite Division of The Institute of Navigation (ION GNSS 2011)*. Portland, OR, USA, Sept. 2011, pp. 3889–3902.

[132] T. Lin, G. Lachapelle, and L. P. S. Fortes. *Ionospheric Scintillation*. Inside GNSS. Jan.–Feb. 2014. URL: https://insidegnss.com/ionospheric-scintillation/.

[133] D. Borio, C. Mongredien, and G. Lachapelle. "New L5/E5a Acquisition Algorithms: Analysis and Comparison". In: *2008 IEEE 10th International Symposium on Spread Spectrum Techniques and Applications*. Bologna, Italy, Aug. 2008, pp. 53–57.

[134] C. Hegarty, M. Tran, and A. J. Van Dierendonck. "Acquisition Algorithms for the GPS L5 Signal". In: *16th International Technical Meeting of the Satellite Division of The Institute of Navigation (ION GPS/GNSS 2003)*. Portland, OR, USA, Sept. 2003, pp. 165–177.

[135] F. Bastide et al. "Analysis of L5/E5 Acquisition, Tracking and Data Demodulation Thresholds". In: *15th International Technical Meeting of the Satellite Division of The Institute of Navigation (ION GPS 2002)*. Portland, OR, USA, Sept. 2002, pp. 2196–2207.

[136] C. Yang, C. Hegarty, and M. Tran. "Acquisition of the GPS L5 Signal Using Coherent Combining of I5 and Q5". In: *17th International Technical Meeting of the Satellite Division of The Institute of Navigation (ION GNSS 2004)*. Long Beach, CA, USA, Sept. 2004, pp. 2184–2195.

[137] C. Yang. "FFT Acquisition of Periodic, Aperiodic, Puncture, and Overlaid Code Sequences in GPS". In: *14th International Technical Meeting of the Satellite Division of The Institute of Navigation (ION GPS 2001)*. Salt Lake City, UT, USA, Sept. 2001, pp. 137–147.

[138] M. Pini, E. Viviani, and L. L. Presti. "GPS L5 Signal Acquisition Exploiting Neumann-Hoffman Code Transitions". In: *2010 International Technical Meeting of The Institute of Navigation*. San Diego, CA, USA, Jan. 2010, pp. 765–772.

[139] G. E. Corazza et al. "Galileo Primary Code Acquisition Based on Multihypothesis Secondary Code Ambiguity Elimination". In: *20th International Technical Meeting of the Satellite Division of The Institute of Navigation (ION GNSS 2007)*. Fort Worth, TX, USA, Sept. 2007, pp. 2459–2465.

[140] D. Borio. "M-Sequence and Secondary Code Constraints for GNSS Signal Acquisition". In: *IEEE Transactions on Aerospace and Electronic Systems* 47.2 (Apr. 2011), pp. 928–945.

[141] N. C. Shivaramaiah, A. G. Dempster, and C. Rizos. "Exploiting the Secondary Codes to Improve Signal Acquisition Performance in Galileo Receivers". In: *21st International Technical Meeting of the Satellite Division of The Institute of Navigation (ION GNSS 2008)*. Savannah, GA, USA, Sept. 2008, pp. 1497–1506.

[142] J. Leclère, C. Botteron, and P. Farine. "High Sensitivity Acquisition of GNSS Signals with Secondary Code on FPGAs". In: *IEEE Aerospace and Electronic Systems Magazine* 32.8 (Aug. 2017), pp. 46–63.

[143] J. Leclère and R. J. Landry. "Combining Secondary Code Correlations for Fast GNSS Signal Acquisition". In: *2018 IEEE/ION Position, Location and Navigation Symposium (PLANS)*. Monterey, CA, USA, Apr. 2018, pp. 46–55.

[144] J. B.-Y. Tsui. *Fundamentals of Global Positioning System Receivers: A Software Approach*. 1st Ed. New York, NY, USA: John Wiley & Sons, Inc., May 2000.

[145] D. Borio, C. O'Driscoll, and G. Lachapelle. "Coherent, Noncoherent, and Differentially Coherent Combining Techniques for Acquisition of New Composite GNSS Signals". In: *IEEE Transactions on Aerospace and Electronic Systems* 45.3 (July 2009), pp. 1227–1240.

[146] D. Borio. "A Statistical Theory for GNSS Signal Acquisition". PhD thesis. Turin, Italy: Department of Electronics and Telecommunications, Politecnico di Torino, Mar. 2008.

[147] P. W. Ward, J. W. Betz, and C. J. Hegarty. "Satellite Signal Acquisition, Tracking, and Data Demodulation". In: *Understanding GPS Principles and Applications*. Ed. by E. D. Kaplan and C. J. Hegarty. 2nd Ed. Norwood, MA, USA: Artech House, Inc., 2006. Chap. 5, pp. 153–241.

[148] P. M. Kintner, B. M. Ledvina, and E. R. de Paula. "GPS and Ionospheric Scintillations". In: *Space Weather* 5.9 (Sept. 2007).

[149] A. J. Van Dierendonck. "GPS Receivers". In: *Global Positioning System: Theory and Applications, Volume I*. Ed. by J. J. Spilker Jr. et al. 370 L'Enfant Promenade, SW, Washington, DC: American Institute of Aeronautics and Astronautics, Inc., 1996. Chap. 8, pp. 329–407.

[150] S. Stevanovic and B. Pervan. "A GPS Phase-Locked Loop Performance Metric Based on the Phase Discriminator Output". In: *Sensors* 18.1 (Jan. 2018), p. 296.

[151] R. Kline. "Cybernetics, Automata Studies, and the Dartmouth Conference on Artificial Intelligence". In: *IEEE Annals of the History of Computing* 33.4 (2011), pp. 5–16.

[152] M. Z. Alom et al. "A State-of-the-Art Survey on Deep Learning Theory and Architectures". In: *Electronics* 8.3 (2019).

[153] W. Thompson, H. Lui, and A. Bolen. *Artificial Intelligence, Machine Learning, Deep Learning and Beyond*. Accessed on Jan. 20, 2021. SAS, NC, USA. URL: https://www.sas.com/en_us/insights/articles/big-data/artificial-intelligence-machine-learning-deep-learning-and-beyond.html#/.

[154] Kevin P. Murphy. *Machine Learning - A Probabilistic Perspective*. Adaptive Computation and Machine Learning Series. Cambridge, Massachusetts, USA: The MIT Press, 2012.

[155] T. Hastie, R. Tibshirani, and J. H. Friedman. *The Elements of Statistical Learning: Data Mining, Inference, and Prediction*. 2nd Ed. Springer Series in Statistics. Springer, 2009.

[156] I. Goodfellow, Y. Bengio, and A. Courville. *Deep Learning*. Adaptive Computation and Machine Learning. MIT Press, Cambridge, MA, 2016.

[157] Charu C. Aggarwal. *Neural Networks and Deep Learning. A Textbook*. Cham, Switzerland: Springer, 2018.

[158] A. Sengupta et al. "Going Deeper in Spiking Neural Networks: VGG and Residual Architectures". In: *Frontiers in Neuroscience* 13 (2019), p. 95. URL: https://www.frontiersin.org/article/10.3389/fnins.2019.00095.

[159] A. Burkov. *The Hundred-Page Machine Learning Book*. Andriy Burkov, 2019.

[160] S. Dargan et al. "A Survey of Deep Learning and Its Applications: A New Paradigm to Machine Learning". In: *Archives of Computational Methods in Engineering* 27.4 (Sept. 2020), pp. 1071–1092.

[161] I. V. Malygin et al. "Radio Signal Detection Using Machine-Learning Approach". In: *Information Technologies, Telecommunications and Control Systems (ITTCS)*. 2017, pp. 57–61.

[162] I. Sutskever, O. Vinyals, and Q. V. Le. "Sequence to Sequence Learning with Neural Networks". In: *CoRR* abs/1409.3215 (2014). arXiv: 1409.3215. URL: http://arxiv.org/abs/1409.3215.

[163] X. Li et al. "A Survey on Deep Learning Techniques in Wireless Signal Recognition". In: *Wireless Communications and Mobile Computing* 2019 (Deep Learning Driven Wireless Communications and Mobile Computing Feb. 2019), pp. 1–12.

[164] B. Kim et al. "Deep Neural Network-based Automatic Modulation Classification Technique". In: *2016 International Conference on Information and Communication Technology Convergence (ICTC)*. Oct. 2016, pp. 579–582.

[165] W. Yin et al. "Comparative Study of CNN and RNN for Natural Language Processing". In: *CoRR* abs/1702.01923 (2017). arXiv: 1702.01923. URL: http://arxiv.org/abs/1702.01923.

[166] C. Fan, X. Yuan, and Y. A. Zhang. "Deep-Learning-Based Signal Detection for Banded Linear Systems". In: *2018 IEEE Global Communications Conference (GLOBECOM)*. Dec. 2018, pp. 1–6.

[167] P. Borhani-Darian and P. Closas. "Deep Neural Network Approach to GNSS Signal Acquisition". In: *2020 IEEE/ION Position, Location and Navigation Symposium (PLANS)*. 2020, pp. 1214–1223.

[168] R. Morales-Ferre et al. "A Survey on Coping With Intentional Interference in Satellite Navigation for Manned and Unmanned Aircraft". In: *IEEE Communications Surveys Tutorials* 22.1 (2020), pp. 249–291.

[169] P. Gao et al. "GNSS Spoofing Jamming Recognition Based on Machine Learning". In: *Signal and Information Processing, Networking and Computers*. Ed. by S. Sun, N. Chen, and T. Tian. Singapore: Springer, 2018, pp. 221–228.

[170] S. Semanjski et al. "Use and Validation of Supervised Machine Learning Approach for Detection of GNSS Signal Spoofing". In: *2019 International Conference on Localization and GNSS (ICL-GNSS)*. June 2019, pp. 1–6.

[171] W. Li et al. "A Real-Time Interference Monitoring Technique for GNSS Based on a Twin Support Vector Machine Method". In: *Sensors* 16.3 (2016).

[172] J. Pihlajasalo et al. "Improvement of GPS and BeiDou extended orbit predictions with CNNs". In: *2018 European Navigation Conference (ENC)*. May 2018, pp. 54–59.

[173] H. Peng and X. Bai. "Improving Orbit prediction accuracy through supervised machine learning". In: *Advances in Space Research* 61.10 (May 2018), pp. 2628–2646. URL: http://dx.doi.org/10.1016/j.asr.2018.03.001.

[174] J. Pihlajasalo et al. “Methods for Long-Term GNSS Clock Offset Prediction”. In: *2019 International Conference on Localization and GNSS (ICL-GNSS)*. June 2019, pp. 1–6.

[175] E. Tulunay et al. “Forecasting Total Electron Content Maps by Neural Network Technique”. In: *Radio Science* 41.04 (2006), pp. 1–12.

[176] C. Cesaroni et al. “Neural Network Based Model for Global Total Electron Content Forecasting”. In: *J. Space Weather Space Clim.* 10 (Mar. 2020), p. 11.

[177] A. Boulch, N. Cherrier, and T. Castaings. *Ionospheric Activity prediction using convolutional recurrent neural networks*. 2018. arXiv: 1810.13273 [cs.CV]. URL: https://arxiv.org/abs/1810.13273v2.

[178] O. Ureten and N. Serinken. “Wireless Security Through RF Fingerprinting”. In: *Canadian Journal of Electrical and Computer Engineering* 32.1 (2007), pp. 27–33.

[179] D. Borio et al. *Feature Selection for GNSS Receiver Fingerprinting*. Inside GNSS. July–Aug. 2017. URL: https://insidegnss.com/feature-selection-for-gnss-receiver-fingerprinting/.

[180] Q. Xu et al. “Device Fingerprinting in Wireless Networks: Challenges and Opportunities”. In: *IEEE Communications Surveys and Tutorials* 18.1 (Jan. 2016), pp. 94–104.

[181] A. Khalajmehrabadi, N. Gatsis, and D. Akopian. “Modern WLAN Fingerprinting Indoor Positioning Methods and Deployment Challenges”. In: *IEEE Communications Surveys Tutorials* 19.3 (2017), pp. 1974–2002.

[182] C. Bertoncini et al. “Wavelet Fingerprinting of Radio-Frequency Identification (RFID) Tags”. In: *IEEE Transactions on Industrial Electronics* 59.12 (2012), pp. 4843–4850.

[183] D. Borio et al. “GNSS Receiver Identification Using Clock-Derived Metrics”. In: *Sensors* 17.9 (2017).

[184] L. Wang, P. D. Groves, and M. K. Ziebart. “Urban Positioning on a Smartphone: Real-time Shadow Matching Using GNSS and 3D City Models”. In: *26th International Technical Meeting of the Satellite Division of The Institute of Navigation (ION GNSS+ 2013)*. Nashville, TN, USA, Sept. 2013, pp. 1606–1619.

[185] M. Sun et al. “RF Fingerprint Extraction for GNSS Anti-Spoofing Using Axial Integrated Wigner Bispectrum”. In: *Journal of Information Security and Applications* 35 (2017), pp. 51–54.

[186] S. Gahlawat. "Investigation of RF Fingerprinting Approaches in GNSS". MA thesis. Kalevantie, Tampere, Finland: Faculty of Information Technology and Communication Sciences, Tampere University, May 2020. URL: https://trepo.tuni.fi/handle/10024/122150.

[187] C. Cortes and V. Vapnik. "Support-vector networks". In: *Machine Learning* 20 (Sept. 1995), pp. 273–297.

[188] Y. Jiao, J. J. Hall, and Y. T. Morton. "Automatic Equatorial GPS Amplitude Scintillation Detection Using a Machine Learning Algorithm". In: *IEEE Transactions on Aerospace and Electronic Systems* 53.1 (Feb. 2017), pp. 405–418.

[189] Y. Jiao, J. J. Hall, and Y. T. Morton. "Performance Evaluation of an Automatic GPS Ionospheric Phase Scintillation Detector Using a Machine-Learning Algorithm". In: *NAVIGATION* 64.3 (Oct. 2017), pp. 391–402.

[190] O. Bousquet and D. Herrmann. "On the Complexity of Learning the Kernel Matrix". In: *Advances in Neural Information Processing Systems 15 [Neural Information Processing Systems, NIPS 2002, December 9-14, 2002, Vancouver, British Columbia, Canada]*. Ed. by Suzanna Becker, Sebastian Thrun, and Klaus Obermayer. Cambridge, MA, USA: MIT Press, Oct. 2003, pp. 399–406.

[191] Z. Liu et al. "An Analytical Approach to Fast Parameter Selection of Gaussian RBF Kernel for Support Vector Machine". In: *J. Inf. Sci. Eng.* 31.2 (Mar. 2015), pp. 691–710.

[192] N. Cristianini and J. Shawe-Taylor. *An Introduction to Support Vector Machines and Other Kernel-based Learning Methods*. 16th Ed. Cambridge, UK: Cambridge University Press, 2014.

[193] A. Ben-Hur and J. Weston. "A User's Guide to Support Vector Machines". In: *Data Mining Techniques for the Life Sciences. Methods in Molecular Biology (Methods and Protocols)*. Ed. by Carugo O. and Eisenhaber F. Vol. 609. Humana Press, 2010, pp. 223–239.

[194] C.-W. Hsu, C.-C. Chang, and C.-J. Lin. *A Practical Guide to Support Vector Classification*. Tech. rep. Taipei, Taiwan: Department of Computer Science, National Taiwan University, July 2003. URL: https://www.csie.ntu.edu.tw/~cjlin/papers/guide/guide.pdf.

[195] D. D. Gutierrez. *Machine Learning and Data Science: An Introduction to Statistical Learning Methods with R*. Basking Ridge, NJ, USA: Technics Publications, 2015.

[196] Christopher M. Bishop. *Pattern Recognition and Machine Learning (Information Science and Statistics)*. Berlin, Heidelberg: Springer-Verlag, 2006.

[197] J. Shawe-Taylor and N. Cristianini. *Kernel Methods for Pattern Analysis*. New York, NY, USA: Cambridge University Press, 2004.

[198] N. Aronszajn. "Theory of Reproducing Kernels". In: *Transactions of the American Mathematical Society* 68.3 (1950), pp. 337–404.

[199] B.-H. Asa et al. "Support Vector Machines and Kernels for Computational Biology". In: *PLoS Computational Biology* 4.10 (Oct. 2008).

[200] A. O. Moraes et al. "Extended Ionospheric Amplitude Scintillation Model for GPS Receivers". In: *Radio Science* 49.5 (2014), pp. 315–329.

[201] J. Kinrade et al. "Ionospheric Scintillation Over Antarctica During the Storm of 5–6 April 2010". In: *Journal of Geophysical Research: Space Physics* 117.A5 (2012).

[202] F. Provost and T. Fawcett. *Data Science for Business: What You Need to Know about Data Mining and Data-Analytic Thinking*. Sebastopol, CA, USA: O'Reilly Media, Inc., Aug. 2013.

[203] T. Fawcett. "An Introduction to ROC Analysis". In: *Pattern Recognition Letters* 27.8 (June 2006), pp. 861–874.

[204] N. Japkowicz and M. Shah. *Evaluating Learning Algorithms: A Classification Perspective*. New York, NY, USA: Cambridge University Press, Aug. 2011.

[205] *MATLAB and Statistics and Machine Learning Toolbox*. The Mathworks, Inc., Natick, MA, USA. <R2019b>.

[206] T. Wang. "Development of the Machine Learning-Based Approach to Access Occupancy Information through Indoor CO_2 Data". MA thesis. Delft, The Netherlands: Delft University of Technology, 2017.

[207] A. Abdiansah and R. Wardoyo. "Time Complexity Analysis of Support Vector Machines (SVM) in LibSVM". In: *International Journal of Computer Applications* 128.3 (Oct. 2015), pp. 28–34.

[208] M. Claesen et al. *Fast Prediction with SVM Models Containing RBF Kernels*. 2014. arXiv: 1403.0736 [stat.ML].

[209] A. P. Bradley. "The Use of The Area Under the ROC Curve in The Evaluation of Machine Learning Algorithms". In: *Pattern Recognition* 30.7 (July 1997), pp. 1145–1159.

[210] K. M. Ting. "Confusion Matrix". In: *Encyclopedia of Machine Learning*. Ed. by C. Sammut and G. I. Webb. Boston, MA, USA: Springer, 2011, pp. 209–209.

[211] X. Wu et al. "Top 10 Algorithms in Data Mining". In: *Knowledge and Information Systems* 14 (Jan. 2008), pp. 1–37.

[212] I. W. Tsang, J. T. Kwok, and P.-M. Cheung. "Core Vector Machines: Fast SVM Training on Very Large Data Sets". In: *Journal of Machine Learning Research* 6.13 (2005), pp. 363–392.

[213] J. Nalepa and M. Kawulok. "Selecting Training Sets for Support Vector Machines: A Review". In: *Artificial Intelligence Review* 52 (Aug. 2019), pp. 857–900.

[214] L. Hsu. "GNSS Multipath Detection Using a Machine Learning Approach". In: *2017 IEEE 20th International Conference on Intelligent Transportation Systems (ITSC)*. Yokohama, Japan, Oct. 2017, pp. 1–6.

[215] Y. Quan. "A New Machine Learning Based Method for Multi-GNSS Data Quality Assurance and Multipath Detection". PhD thesis. Nottingham: University of Nottingham, Sept. 2017.

[216] Q.-H. Phan, S.-L. Tan, and I. McLoughlin. "GPS Multipath Mitigation: A Nonlinear Regression Approach". In: *GPS Solutions* 17.3 (July 2013), pp. 371–380.

[217] Y. Quan et al. "Convolutional Neural Network Based Multipath Detection Method for Static and Kinematic GPS High Precision Positioning". In: *Remote Sensing* 10.12 (Dec. 2018).

[218] E. Munin, A. Blais, and N. Couellan. *Convolutional Neural Network for Multipath Detection in GNSS Receivers*. 2019. arXiv: 1911.02347 [eess.SP].

[219] S. J. Cho et al. "Enhancing GNSS Performance and Detection of Road Crossing in Urban Area Using Deep Learning". In: *2019 IEEE Intelligent Transportation Systems Conference (ITSC)*. 2019, pp. 2115–2120.

[220] J. Vesanto and E. Alhoniemi. "Clustering of the Self-Organizing Map". In: *IEEE Transactions on Neural Networks* 11.3 (2000), pp. 586–600.

[221] Y. Xiao and Y. Jian. "Partitive Clustering (K-means Family)". In: *WIREs Data Mining and Knowledge Discovery* 2.3 (2012), pp. 209–225.

[222] T. Kohonen. *Self-Organizing Maps*. 3rd Ed. Berlin Heidelberg: Springer-Verlag, 2001.

[223] S. Delgado et al. "A SOM Prototype-Based Cluster Analysis Methodology". In: *Expert Syst. Appl.* 88.C (Dec. 2017), pp. 14–28.

[224] J. Vesanto et al. *Som Toolbox for MATLAB 5*. Tech. rep. Espoo, Finland: SOM Toolbox Team, Helsinki University of Technology, 2000. URL: http://www.cis.hut.fi/projects/somtoolbox/package/papers/techrep.pdf.

[225] S. Haykin. *Adaptive Filter Theory*. 5th Ed. Edinburgh, England: Pearson Education Limited, 2014.

[226] B. Fornberg. "Generation of Finite Difference Formulas on Arbitrarily Spaced Grids". In: *Mathematics of Computation* 51.184 (Oct. 1988), pp. 699–706.

[227] P. Stefanovic and O. Kurasova. "Influence of Learning Rates and Neighboring Functions on Self-Organizing Maps". In: *Advances in Self-Organizing Maps - 8th International Workshop, WSOM 2011, Espoo, Finland, June 13-15, 2011. Proceedings*. Ed. by J. Laaksonen and T. Honkela. Vol. 6731. Lecture Notes in Computer Science. Springer, 2011, pp. 141–150.

[228] A. M. M. Kamel. "Context Aware High Dynamics GNSS-INS for Interference Mitigation". PhD thesis. Calgary, Canada: Department of Geomatics Engineering, University of Calgary, Aug. 2011.

[229] R. G. Brown and P. Y. C. Hwang. *Introduction to Random Signals and Applied Kalman Filtering. with MATLAB exercises*. 4th Ed. Hoboken, NJ, USA: Wiley, 2012.

[230] M. Susi et al. "Tuning a Kalman Filter Carrier Tracking Algorithm in the Presence of Ionospheric Scintillation". In: *GPS Solutions* 21 (July 2017).

[231] P. Laface and S. Cumani. *Support Vector Machines*. Lecture Notes in Machine Learning for Pattern Recognition (01SCSIU). Turin, Italy: Computer and Control Engineering, Politecnico di Torino, Mar. 2018.

[232] Fugro Satellite Positioning. *The effect of space weather phenomena on precise GNSS applications*. Tech. rep. Leidschendam, The Netherlands: Fugro N.V., Dec. 2014. URL: https://fsp.support/pl/12321850.php.

[233] J. T. Curran, M. Bavaro, and G. J. Fortuny. "An Open-Loop Vector Receiver Architecture for GNSS-Based Scintillation Monitoring". In: *European Navigation Conference (ENC) - GNSS 2014*. Rotterdam, The Netherlands: Netherlands Institute of Navigation (NIN), Apr. 2014, pp. 1–12.

[234] F. Dovis and T. H. Ta. "High Sensitivity Techniques for GNSS Signal Acquisition". In: *Global Navigation Satellite Systems: Signal, Theory and Applications*. Ed. by Shuanggen Jin. 51000 Rijeka, Croatia: IntechOpen, Feb. 2012. Chap. 1, pp. 3–32.

[235] B. Zheng and G. Lachapelle. "Acquisition Schemes for a GPS L5 Software Receiver". In: *17th International Technical Meeting of the Satellite Division of The Institute of Navigation (ION GNSS 2004)*. Long Beach, CA, USA, Sept. 2004, pp. 1035–1040.

This Ph.D. thesis has been typeset by means of the TEX-system facilities. The typesetting engine was pdfLATEX. The document class was `toptesi`, by Claudio Beccari, with option `tipotesi=scudo`. This class is available in every up-to-date and complete TEX-system installation.